

# Host Galaxies of Ultra Strong Mg II absorbers at $z \sim 0.5$

Labanya Kumar Guha<sup>1\*</sup>, Raghunathan Srianand<sup>1</sup>, Rajeshwari Dutta<sup>2,6</sup>, Ravi Joshi<sup>3</sup>,  
Pasquier Noterdaeme<sup>4,5</sup> & Patrick Petitjean<sup>4</sup>

<sup>1</sup> IUCAA, Postbag 4, Ganeshkhind, Pune 411007, India

<sup>2</sup> Dipartimento di Fisica G. Occhialini, Università degli Studi di Milano-Bicocca, Piazza della Scienza 3, 20126 Milano, Italy

<sup>3</sup> Indian Institute of Astrophysics, Koramangala II Block, Bangalore 560 034, India.

<sup>4</sup> Institut d'Astrophysique de Paris, Sorbonne Universités and CNRS, 98bis boulevard Arago, 75014 Paris, France

<sup>5</sup> Franco-Chilean Laboratory for Astronomy, IRL3386, Camino el Observatorio 1515, Las Condes, Santiago, Chile

<sup>6</sup> INAF - Osservatorio Astronomico di Brera, via Bianchi 46, 23087 Merate (LC), Italy

Accepted XXX. Received YYY; in original form ZZZ

## ABSTRACT

From a sample of 109 candidate Ultra-Strong Mg II (USMgII; having rest equivalent width of Mg II,  $W_{2796} > 3.0\text{\AA}$ ) systems at  $z=0.4-0.6$ , we confirm 27 and identify host galaxies of 20 systems based on associated nebular line emission from our SALT observations or from SDSS fiber spectra. The measured impact parameter, [O II] luminosity, star formation rate, B-band luminosity and stellar mass are in the ranges  $7.3 \leq D[\text{kpc}] \leq 79$ ,  $0.2 \leq L_{[\text{O II}]}[10^{41} \text{ ergs}^{-1}] \leq 4.5$ ,  $2.59 \leq \text{SFR}[M_{\odot}\text{yr}^{-1}] \leq 33.51$ ,  $0.15L_{\text{B}}^* \leq L_{\text{B}} \leq 1.63L_{\text{B}}^*$  and  $10.21 \leq \log[M_{*}/M_{\odot}] \leq 11.62$  respectively. The impact parameters found are larger than that predicted by the  $W_{2796}$  vs  $D$  relationship of the general population of Mg II absorbers. At a given  $D$ , USMgII host galaxies are more luminous and massive compared to typical Mg II absorbers. However, the measured SFRs are slightly lower than that of main-sequence galaxies with same  $M_{*}$  at  $z \sim 0.5$ . We report a correlation between  $L_{[\text{O II}]}$  and  $W_{2796}$  for the full population of Mg II absorbers, driven mainly by the host galaxies of weak Mg II absorbers that tend to have low  $L_{[\text{O II}]}$  and large impact parameters. We find at least  $\sim 33\%$  of the USMgII host galaxies (with a limiting magnitude of  $m_r < 23.6$ ) are isolated and the large  $W_{2796}$  in these cases may originate from gas flows (infall/outflow) in single halos of massive but not starburst galaxies. We also find galaxy interactions could be responsible for large velocity widths in at least  $\sim 17\%$  cases.

**Key words:** galaxies: evolution; galaxies: groups: general; galaxies: high-redshift; galaxies: haloes; quasars: absorption lines

## 1 INTRODUCTION

Our current understanding of galaxy formation and evolution is based on the model known as the ‘cosmic baryon cycle’, according to which, galaxies evolve by means of a slowly varying equilibrium between inflows from the intergalactic medium (IGM), high velocity outflows from the galaxy and the in-situ star-formation taking place within the galaxy (Anglés-Alcázar et al. 2017; Péroux & Howk 2020). Biconical galactic scale outflows (with velocities of 100–1000  $\text{km s}^{-1}$ ), probed by neutral or singly ionized species like Na I, Mg II and Fe II in absorption, are ubiquitous in high redshift (i.e.  $0.5 \leq z \leq 1.5$ ) galaxies (e.g. Tremonti et al. 2007; Chen et al. 2010a; Martin et al. 2012; Rubin et al. 2014; Bordoloi et al. 2014). The probability to detect a wind is found to depend weakly on the intrinsic properties of the galaxies but strongly on the galaxy orientation. Notwithstanding this, the importance of star formation

rate (SFR) and stellar mass ( $M_{*}$ ) of the host galaxy is reflected by the correlations observed between the maximum wind velocity ( $v_{\text{max}}$ ) and  $M_{*}$ , and between the equivalent width of the flow and SFR. *While the presence of a wind is well established in these galaxies, its location (important for deriving wind parameters) with respect to the stellar disk can not be constrained accurately.*

On the other hand, quasar absorption lines in principle allow us to probe the spatial distribution and kinematics of the gas in foreground galaxies at very small impact parameters ( $D$ ), thereby allowing us to probe the nature of gas flows in these galaxies. Presence of cool circumgalactic medium (CGM) around galaxies out to projected distances of  $\sim 200$  kpc (for example, Bergeron & Boissé 1991; Steidel 1995; Chen et al. 2010a; Nielsen et al. 2013a; Rubin et al. 2018) is well established and an anti-correlation between the rest equivalent width of Mg II  $\lambda 2796$  absorption (i.e.  $W_{2796}$ ) and the impact parameter has been derived using spectra of distant quasars. While early models reproduced this correlation using photoionized halos around galaxies (see for example, Petitjean et al. 1992; Srianand

\* E-mail: labanya@iucaa.in (LKG)

& Khare 1994), it was apparent that continuous gas flow is needed to sustain the observed covering fraction of gas over a long period.

This observed anti-correlation between  $W_{2796}$  and  $D$  allows us to select quasar and foreground galaxy pairs with small impact parameters using absorption systems with large  $W_{2796}$  (see, Bouché et al. 2007, 2012). The Mg II absorption systems with  $W_{2796} > 3\text{Å}$  are known as Ultra-Strong Mg II absorbers (referred hereafter as USMgII ; Nestor et al. 2011a). They constitute only 0.8% of the Mg II absorber population having  $W_{2796} > 0.02\text{Å}$ . Observationally such large equivalent widths are seen in a very high fraction (i.e. 30-50%) of (i) outflows detected in  $z \sim 0.5$  galaxies (Rubin et al. 2014); (ii) Milky Way sightlines that probe disk+halo gas (after applying a factor 2 correction to match with QSO absorbers, Savage et al. 2000); (iii) Galaxy On Top Of Quasars (GOTOQs; Noterdaeme et al. 2010b; Straka et al. 2015; Joshi et al. 2017, 2018) and (iv) high- $z$  C I absorbers (Ledoux et al. 2015; Zou et al. 2018). From figure 2 of Rao et al. (2017) it is also evident that more than 50% of USMgII absorbers are damped Lyman- $\alpha$  systems (DLAs; neutral hydrogen column density,  $N(\text{H I}) \geq 2 \times 10^{20}\text{ cm}^{-2}$ ).

It is well known that the measured  $W_{2796}$  using low dispersion spectra are related to the number of absorbing clouds and velocity dispersion between them, and not directly related to the column density (Petitjean & Bergeron 1990). For a fully saturated Mg II line,  $W_{2796} \geq 3\text{Å}$  would correspond to a minimum velocity width of  $320\text{ km s}^{-1}$ . Gas having such velocity spread usually have large metallicities (Ledoux et al. 2006). Large velocity spread could originate from, (i) galactic-scale outflows (Bouché et al. 2006; Weiner et al. 2009; Rubin et al. 2012), (ii) filamentary accretion onto galaxies (Steidel et al. 2002; Chen et al. 2010a), (iii) dynamical mergers (Richter 2012) and intra-group gas (Rubin et al. 2010; Gauthier 2013). In such cases, measured metallicities and galaxy orientations with respect to the quasar sightlines are used to distinguish between the different possibilities (Péroux et al. 2013; Kacprzak et al. 2014; Zabl et al. 2019; Bordoloi et al. 2011; Péroux et al. 2020; Zabl et al. 2021).

It is possible that absorption line-based selection of galaxies (unbiased by the galaxy luminosity) may pick a population that is different from that observed through galaxy surveys that rely on optical colours and emission line strengths. Large  $W_{2796}$  systems, in particular the USMgII systems have been associated with host-galaxies that are going through a rapid star-formation episode or have been through a phase of rapid star-formation in the recent past, i.e. they are either star-burst or post star-burst galaxies (Nestor et al. 2011a). By studying the average photometric properties of more than 2800 Mg II systems, Zibetti et al. (2007) suggested that the stronger Mg II systems (with  $W_{2796} \geq 1\text{Å}$ ) are associated with actively star-forming galaxies. Based on the [O II] emission associated to Mg II-selected systems, Noterdaeme et al. (2010a) found a strong correlation between  $W_{2796}$  and [O II] luminosity. In a similar work, Ménard et al. (2011) interpreted this as a correlation between  $W_{2796}$  and SFR, but this interpretation was later shown to be vulnerable to fiber losses effects (López & Chen 2012; Joshi et al. 2017).

Discussions presented above suggests that USMgII absorbers are ideal targets for studying the gas flows at low impact parameters to star forming galaxies and/or interacting groups of galaxies. Studying such systems can provide important insights into the baryonic cycle that governs the galaxy evolution. Motivated by this, we embarked on a detailed study of USMgII systems at  $z \sim 0.5$  with the aim to (i) identify their host galaxies and characterize the galaxy environment around these absorbers, (ii) investigate whether we preferentially select a particular galaxy population using the USMgII selection, (iii) study the connection between the galaxy properties and that

of the absorption features, and (iv) identify potential quasar-galaxy pairs where galactic outflow can be studied through down-the-barrel absorption towards the galaxy, and absorption along the quasar line-of-sight simultaneously. This paper is organized as follows. In section 2, we discuss the sample. The observational setup, data reduction and calibrations are described in section 3. The identification of the USMgII host galaxies and the method of inferring their physical properties based on the available spectro-photometric data are discussed in section 4. In section 5, we present the results of our analysis and the nature of the USMgII host galaxies based on the inferred galaxy properties. As we go along, to investigate whether the USMgII host galaxies are drawn from a specific galaxy population or not, we compare their properties against various low- $z$  Mg II and DLA absorber samples available in the literature. Wherever possible, we also compare the properties of our sample with those of high- $z$  C I absorbers. In section 6, we provide an overall discussion on the USMgII systems. Our conclusions are summarized in section 7. Throughout this paper we assume a flat  $\Lambda$ CDM cosmology with  $H_0 = 70\text{ km s}^{-1}\text{ Mpc}^{-1}$  and  $\Omega_{m,0} = 0.3$ .

## 2 OUR SAMPLE OF USMgII SYSTEMS AT $Z \sim 0.5$ :

We compiled a sample of USMgII systems that are accessible to the South African Large Telescope (SALT, Buckley et al. 2005) (i.e., declination,  $\delta \leq +10^\circ$ ), using the Sloan Digital Sky Survey (SDSS, York et al. 2000) Mg II/Fe II absorber catalog of Zhu & Ménard (2013) in the redshift range  $0.4 \leq z_{\text{abs}} \leq 0.6$ . The lower limit in  $z_{\text{abs}}$  was chosen so that the SDSS spectra could cover the Fe II  $\lambda 2600$  absorption line, while the upper limit on  $z_{\text{abs}}$  is set to be able to cover the [O II]  $\lambda\lambda 3727, 3729$  doublet, H $\beta$  and [O III]  $\lambda\lambda 4960, 5008$  nebular emission lines associated with the USMgII absorption, in the wavelength range over which the Robert-Stobie Spectrograph (RSS) attached to SALT has good sensitivity. Application of these criteria has resulted in a total of 109 USMgII systems along the line-of-sight towards 106 different background quasars. A careful visual inspection of the SDSS spectrum of each of these quasars has led to the removal of 34 systems from our sample owing to the false identification of Mg II doublets. In 48 cases C IV or Si IV Broad Absorption Lines (BAL) are misidentified as Mg II. After removing these we are left with a sample of 27 USMgII systems.

Details of all the 109 USMgII systems retrieved from the SDSS Mg II / Fe II absorber catalog of Zhu & Ménard (2013) are provided in Table B1 of Appendix B, where we have explicitly mentioned the reason for rejecting or accepting a USMgII system in our sample along with information such as the quasar and absorption redshifts. Among these 27 systems, the galaxy association for 3 USMgII systems have already been studied in the literature in some detail. One is the multiband photometric study of the environment of the USMgII system J0240-0812 (Nestor et al. 2007), and another is the spectro-photometric study of the USMgII system J2207-0901 (Gauthier 2013). In addition, using the X-shooter spectrograph at the Very Large Telescope, Rahmani et al. (2016) have studied the galaxy associated with the  $z_{\text{abs}} = 0.5896$  USMgII absorber, which is a known DLA. The [O II] nebular emission from another three of our USMgII systems (i.e.  $z_{\text{abs}} = 0.5928$  towards J0930+0018,  $z_{\text{abs}} = 0.5561$  towards J1025-0046 and  $z_{\text{abs}} = 0.5519$  towards J1216+0350) were detected in the SDSS spectrum and these systems are part of the GOTOQ sample of Joshi et al. (2017).

In order to reconfirm that all the selected Mg II systems are bona fide USMgII systems, we measured the rest equivalent widths of Mg II  $\lambda\lambda 2796, 2803$  absorption lines by Gaussian fitting after approx-

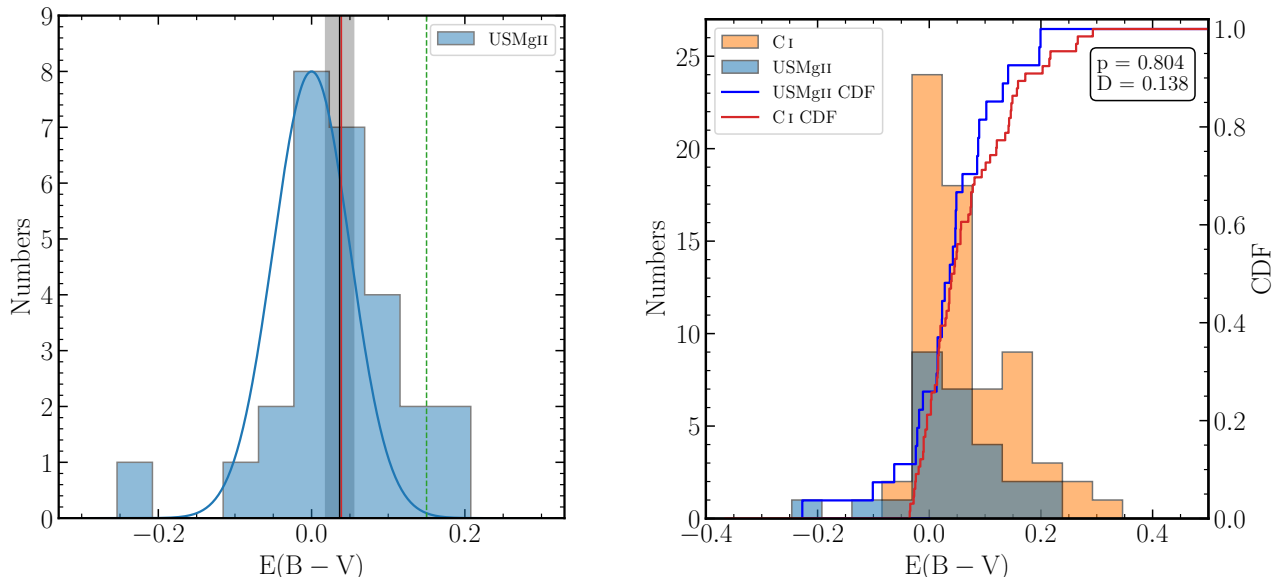


**Figure 1.** *Left panel:* The histogram of the V band colour excess,  $E(B-V)$ , for the USMgII systems in our sample. The deep blue Gaussian ( $\mu = 0$ ,  $\sigma = 0.050$ ) corresponds to the distribution of  $E(B-V)$  that is expected to arise out of the template matching procedure. We inferred this from the distribution of negative  $E(B-V)$  values in our sample (see text for more details). The vertical dashed green line corresponds to the  $3\sigma$  above the mean of the distribution. The solid vertical black line corresponds to the expected colour excess for the  $W_{2796} = 3\text{\AA}$  based on the relation obtained by Budzynski & Hewett (2011) with the gray region showing the  $1\sigma$  uncertainty range. The vertical red line corresponds to the median color excess for our USMgII sample. *Right panel:* Comparison of the distribution of colour excess,  $E(B-V)$ , between the USMgII absorbers (blue histogram) and C I absorbers (orange histogram) taken from Ledoux et al. (2015). The solid blue and red lines correspond to the cumulative distribution of  $E(B-V)$  for the USMgII and C I absorbers, respectively.

imaging the observed continuum spectrum around these absorption lines with smooth polynomials. Our Gaussian fits to absorption lines are shown in Figure A1 and A2. During the fit, we kept the redshift and the velocity width same for both the lines of the Mg II doublet. For the USMgII systems in the spectrum of J0334-0711, J0856+0740, J2045-0704 and, J1114-0023, even at SDSS resolution, the Mg II  $\lambda 2796$  absorption line itself splits into two Gaussian profiles. For these systems, we fit the Mg II  $\lambda\lambda 2796, 2803$  absorption profile with a pair of Gaussian doublets. For each pair, like before, we imposed the redshift and the velocity width for the individual Gaussian to be same. While the total equivalent width is greater than  $3\text{\AA}$ , except for J1114-0023, individual components in these systems are not USMgII absorbers. For these systems, we quote the mean redshift of the pair of Gaussian doublets as the absorption redshift. Our analysis confirmed that all the 27 systems selected are indeed USMgII absorbers. Similarly, we also measured the rest equivalent width of the other associated absorption lines like Fe II  $\lambda 2600$  and Mg I  $\lambda 2853$  by fitting a single Gaussian (also shown in Figure A1). The complete sample along with their absorption properties are presented in Table 1. In this table, the quasar name,  $z_{\text{qso}}$  and  $z_{\text{abs}}$  are summarised in columns 2, 3 and 4 respectively. The next four columns provide rest equivalent widths of Mg II  $\lambda 2796$ , Mg II  $\lambda 2803$ , Fe II  $\lambda 2600$  and Mg I  $\lambda 2853$  respectively. For the cases with detection significance level less than  $3\sigma$ , we provide the  $3\sigma$  upper limits. For these cases, the  $1\sigma$  limit is computed from the total uncertainty across the FWHM of the Mg II absorption line profile around the expected location of the absorption line of our interest.

Next, we identified additional non-USMgII absorber in the SDSS spectra of quasars in our sample. We find 11 Mg II systems but none at  $0.4 \leq z_{\text{abs}} \leq 0.6$ . We then tried to identify if any of the targeted potential host galaxies corresponds to the non-USMgII absorbers identified in the spectra of our sample. We found only one system

at  $z_{\text{abs}} = 0.7981$  ( $W_{2796} = 2.14 \pm 0.18\text{\AA}$ ) towards J1140-0023. We provide the details of this absorber in the last row of Table 1.

## 2.1 Line of sight reddening towards quasars

We calculate the reddening of the background quasar by the absorbing gas assuming the extinction curve of the gas to be similar to the extinction curves of the Small Magellanic Cloud (SMC), Large Magellanic Cloud (LMC), Large Magellanic Cloud Supershell (LMC2) and, our Milky Way (MW) galaxy (Gordon et al. 2003). For the rest wavelength range considered here, the choice of different extinction curves are found to make no significant difference. We fitted all the quasar spectra in our sample with a standard quasar spectrum template (Selsing et al. 2016) redshifted exactly to the quasar redshift and applied the SMC extinction at the redshift of the USMgII absorption, keeping the V band extinction coefficient,  $A_V$ , as the only free parameter, apart from a multiplicative scaling (as described in Srianand et al. 2008). The best fit V-band colour excess,  $E(B-V)$ , for each system is listed in the last column of Table 1.

In Figure 1, the distribution of  $E(B-V)$  is shown in the left panel. For 6 USMgII systems, we find that the color excess,  $E(B-V)$  is negative. The system J1146-0237 has an extremely negative  $E(B-V)$  of  $-0.227$ , which is related to the fact that the quasar has weak emission lines and its spectrum does not exactly follow the standard quasar template. We used the remaining cases with negative values of  $E(B-V)$  to compute the expected scatter from the spectral energy distribution (SED) fitting procedure. The deep blue Gaussian shown in Figure 1 corresponds to the distribution of  $E(B-V)$  (with a  $\sigma = 0.050$ ) that is expected to arise from our template matching procedure. The vertical dashed green line corresponds to the  $3\sigma$  limit of our  $E(B-V)$  measurements. We find only two USMgII systems present in our sample to have  $E(B-V)$  larger than this value. The

highest  $E(B-V)$  of  $\sim 0.2$  is measured for J0156+0343. As this is a C iv BAL quasar, it is not clear how much of the reddening is due to the USMgII absorber.

Using a sample of about 8300 strong Mg II absorption systems identified in the SDSS spectroscopic survey (DR6), [Budzynski & Hewett \(2011\)](#) have shown that  $W_{2796}$  strongly correlates with reddening of the background quasar spectra (see also, [York et al. 2006](#); [Ménard et al. 2008](#)) with  $E(B-V) = [(8.0 \pm 3.0) \times 10^{-4}] \times (W_{2796})^{(3.48 \pm 0.3)}$ . The solid vertical black line in the left panel of the Figure 1 corresponds to the expected  $E(B-V)$  for the  $W_{2796} = 3$  based on this relationship. The solid vertical red line corresponds to the median color excess of our USMgII sample. Higher  $E(B-V)$  seen in our sample is consistent with their results.

In the right panel of Figure 1, the blue and orange histograms correspond to the  $E(B-V)$  measurements for USMgII and high- $z$  C I- selected absorbers from [Ledoux et al. \(2015\)](#) respectively. The solid blue and red lines correspond to the cumulative distribution function for the USMgII and C I absorbers respectively. The median  $E(B-V)$  values for the USMgII and C I absorbers are 0.037 and 0.042 respectively. A two sample Kolmogorov-Smirnov (KS) test between these two samples indicates that the probability of these two samples to arise from the same parent population is  $\sim 80\%$ . This is not surprising given the fact that a good fraction (i.e.  $\sim 47\%$ ) of C I absorbers have  $W_{2796} > 3.0$  (see table 2 of [Zou et al. 2018](#)).

## 2.2 Detection of other metal lines

Out of the 27 USMgII systems, six (along the line-of-sight of J0240–0812, J1016+0752, J1025–0046, J1030–0132, J1216+0350 and J2301–0212) exhibit associated Mn II absorption having more than  $3\sigma$  significance (see Figure A1) with the rest equivalent width in the range,  $0.25 \leq W_{2576}^{\text{MnII}}(\text{\AA}) \leq 1.32$ , while 10 systems (along the line-of-sight of J0218–0832, J0334–0711, J1025–0046, J1214+0804, J1114–0023, J1216+0350, J2121+0039, J2127+0827, J2203–0022 and J2301–0212) exhibit associated Ca II absorption (see Figure A2) with the rest equivalent width in the range ( $0.18 \leq W_{3935}^{\text{CaII}}(\text{\AA}) \leq 1.08$ ) in the SDSS spectra of the background quasars. In the case of non-detection, the  $3\sigma$ , upper limits are typically in the range  $0.5\text{--}0.9\text{\AA}$ . We do not find any significant correlation between  $W_{3935}^{\text{CaII}}$  and  $E(B-V)$ . In addition, the distributions of measured  $E(B-V)$  of sightlines with and without Ca II detected are not statistically different (KS test  $p\text{-value} = 0.23$ ).

For the sake of comparison, in Figure D1, we plot  $E(B-V)$  vs Ca II equivalent width in our sample with those found in low- $z$  DLAs ([Wild & Hewett 2005](#)), high- $z$  C I sample ([Zou et al. 2018](#)) and our Galaxy ([Murga et al. 2015](#)). We do not detect associated Na I absorption (at  $> 3\sigma$  level) for any of the USMgII systems in our sample in the SDSS spectrum. The  $3\sigma$  upper limit on the rest equivalent width lies between  $0.5\text{\AA}$  to  $0.9\text{\AA}$ . As our SALT spectra cover limited wavelength range we could not use them for the above discussed absorption line searches.

## 3 SALT OBSERVATIONS AND DATA REDUCTION

We first identified all galaxies seen within an impact parameter of 50 kpc from the quasar line of sight using the SDSS photometry (typically complete for  $m_r \leq 22.5$ ) and having consistent photometric redshifts within  $1\sigma$ . Note that based on the known anti-correlation between  $D$  and  $W_{2796}$ , we expect the isolated host galaxies to lie within  $D \leq 10$  kpc. Even with the scatter in the relation the observed  $D$  values are  $< 50$  kpc in the available literature data (see discussions in

Section 5.4). Thus we mainly focus on observing candidate galaxies within this impact parameter. We have completed observations for 21 absorbers out of 27 discussed in the previous section.

In Table 2, we provide the number of such galaxies (last column) in addition to our observational log. It is clear from this table that in only one case we have more than one host-galaxy candidate within 50 kpc. These are 5 galaxies in the case of  $z_{\text{abs}} = 0.5581$  towards J0156+0343 within 50 kpc. In 6 cases the potential galaxy image is merged with that of the quasar (see Figure 2). Thus we have 26 host galaxy candidates and we obtained spectra of 23 of them (including from the literature as mentioned above). The SALT spectroscopic observations were carried out using the Robert Stobie Spectrograph (RSS, [Burgh et al. 2003](#); [Kobulnicky et al. 2003](#)) either in the long-slit or the Multi Object Spectroscopy (MOS) mode from June, 2015 to April, 2021 (Program IDs: 2015-1-SCI-021, 2015-2-SCI-031, 2017-1-SCI-011, 2017-2-SCI-009 and 2018-1-SCI-019, 2020-2-SCI-019).

For all our observations, we have used the PG0900 grating along with a slit-width of  $1.5''$  and a suitable grating angle depending on the system observed to get the required wavelength coverage of [O II], [O III] and  $H\beta$  emission lines. Such observational settings resulted in a velocity resolution of  $\sim 300 \text{ km s}^{-1}$ . We have used MOS mode only for two cases (J0344-0711 and J2338-0056) and additional galaxies observed in these cases are beyond 50 kpc. In the case of the GOTOQs, there are no potential USMgII host galaxies seen in SDSS images within 50 kpc and the host galaxy lies on top of the quasar image. We therefore considered two slit position angles to separate the [O II] emission from the quasar continuum trace in the 2D spectra using the triangulation method. Our method is similar to what is discussed in [Fynbo et al. \(2010\)](#); [Srianand et al. \(2016\)](#).

The details of observations along with the observational settings are provided in Table 2. The second column provides the quasar identification. The date of observations, exposure time and mode of observation are presented in columns 3, 4 and 5, respectively. Sixth, seventh and eight columns of this table present the slit position angle, grating angle and the wavelength coverage of the setting used respectively. The number of additional galaxies having consistent photometric redshifts within 100 kpc to the quasar sightlines with photometric redshift consistent with the absorption redshift of the USMgII systems is indicated in column 9 of Table 2.

Our sample is, by far, the largest sample of USMgII systems for which the host galaxy properties are probed over the redshift range  $0.4 \leq z \leq 0.6$ . The field of these targets and the slit orientations are shown in Figure 2. Details of these USMgII systems that were observed with SALT are presented in the top part of Table 1, and the remaining 5 are presented in the bottom part of this table. This unobserved target list also includes two GOTOQ absorbers ( $z_{\text{abs}} = 0.5928$  towards J0932020.60+001828.0 and  $z_{\text{abs}} = 0.5561$  towards J1025–0046), for which, based on the [O II] emission detected on top the SDSS quasar spectrum, we have some information on the host galaxy from the SDSS quasar spectrum itself.

The raw CCD frames were initially subjected to the preliminary data processing with the SALT data reduction and analysis pipeline ([Crawford et al. 2010](#)). Next, we use standard IRAF ([Tody 1986](#)) routines to obtain the wavelength calibrated 2D spectra and the flux calibrated 1D spectra of the quasars as well as the host galaxies. In summary, each of the science frames were first flat-field corrected, cosmic ray zapped, and wavelength calibrated against a standard lamp. Next we applied the extinction correction due to the Earth's atmosphere and then the 1D spectra of the quasar and the galaxy were extracted. The long-slit spectra were all individually flux calibrated against standard stars observed with the same settings as of the

**Table 1.** Details of our USMgII sample. Columns 2, 3 and 4 provide the quasar name, its redshift and the USMgII absorption redshift respectively. The next four columns (i.e. 5 to 8) provide the rest equivalent width of Mg II  $\lambda$  2796, Mg II  $\lambda$  2803, Fe II  $\lambda$  2600 and Mg I  $\lambda$  2853 absorption respectively, where ‘-’ signifies the absorption is outside of the wavelength coverage of the observed spectrum. In the case of non-detections we provide  $3\sigma$  upper limits. Last column provides the measured E(B-V) derived using the SMC extinction curve.

No. (1)	Quasar (2)	$z_{\text{qso}}$ (3)	$z_{\text{abs}}$ (4)	$W_{2796}$ (Å) (5)	$W_{2803}$ (Å) (6)	$W_{2600}$ (Å) (7)	$W_{2853}$ (Å) (8)	E(B-V) (SMC) (9)
Targets with SALT spectrum								
1	J000413.73-082625.4	2.247	0.5544	$3.07 \pm 0.16$	$3.05 \pm 0.15$	$2.05 \pm 0.15$	$0.82 \pm 0.15$	$0.015 \pm 0.002$
2	J015635.18+034308.1	1.371	0.5581	$4.20 \pm 0.30$	$3.76 \pm 0.26$	$3.30 \pm 0.40$	$1.56 \pm 0.26$	$0.199 \pm 0.001$
3	J021820.10-083259.4 <sup>a</sup>	1.219	0.5896	$3.07 \pm 0.11$	$2.81 \pm 0.10$	$2.15 \pm 0.14$	$1.43 \pm 0.14$	$0.022 \pm 0.001$
4	J024008.21-081223.4 <sup>b</sup>	2.230	0.5311	$3.88 \pm 0.17$	$3.56 \pm 0.16$	$2.01 \pm 0.15$	$\leq 0.89$	$0.015 \pm 0.005$
5	J033438.28-071149.0	0.634	0.5977	$3.55 \pm 0.23$	$3.13 \pm 0.24$	$1.89 \pm 0.22$	$0.34 \pm 0.01$	$-0.011 \pm 0.001$
6	J085627.09+074031.7	1.890	0.5232	$4.14 \pm 0.47$	$3.19 \pm 0.61$	$1.22 \pm 0.20$	$0.34 \pm 0.05$	$0.197 \pm 0.001$
7	J092222.58+040858.7	0.713	0.4549	$3.63 \pm 0.21$	$3.11 \pm 0.18$	-	$0.72 \pm 0.12$	$0.049 \pm 0.003$
8	J111400.00-002342.6	0.952	0.5610	$5.75 \pm 1.36$	$4.62 \pm 1.33$	$3.33 \pm 0.95$	$2.40 \pm 0.47$	$0.102 \pm 0.004$
9	J121453.29+080457.7	1.430	0.4908	$3.38 \pm 0.21$	$2.97 \pm 0.19$	$2.27 \pm 0.12$	$\leq 0.63$	$0.089 \pm 0.003$
10	J121628.03+035031.8 <sup>d</sup>	0.996	0.5519	$3.51 \pm 0.12$	$3.53 \pm 0.12$	$2.89 \pm 0.18$	$0.81 \pm 0.12$	$-0.063 \pm 0.001$
11	J155003.71+031325.0	1.789	0.5694	$3.11 \pm 0.08$	$2.97 \pm 0.08$	$1.82 \pm 0.15$	$1.04 \pm 0.16$	$0.141 \pm 0.004$
12	J204501.32-070452.6	0.670	0.5649	$3.77 \pm 0.28$	$3.12 \pm 0.32$	$2.37 \pm 0.15$	$1.21 \pm 0.38$	$0.059 \pm 0.003$
13	J210851.53-074726.5	1.486	0.5187	$3.43 \pm 0.17$	$2.69 \pm 0.14$	$2.24 \pm 0.24$	$1.43 \pm 0.25$	$0.088 \pm 0.003$
14	J212143.98+003954.2	1.348	0.5509	$3.44 \pm 0.33$	$3.57 \pm 0.34$	$2.85 \pm 0.48$	$1.60 \pm 0.24$	$0.132 \pm 0.003$
15	J212727.20+082724.6	0.745	0.4392	$4.26 \pm 0.16$	$3.99 \pm 0.15$	$3.75 \pm 0.16$	$1.28 \pm 0.13$	$0.042 \pm 0.001$
16	J220330.04-002211.4	1.782	0.4381	$4.49 \pm 0.31$	$3.99 \pm 0.27$	-	$0.82 \pm 0.13$	$0.022 \pm 0.002$
17	J220702.53-090127.7 <sup>c</sup>	1.296	0.5623	$4.08 \pm 0.18$	$3.66 \pm 0.16$	$2.93 \pm 0.32$	$1.39 \pm 0.14$	$0.047 \pm 0.002$
18	J230101.28-021200.0	0.619	0.5367	$3.16 \pm 0.07$	$3.07 \pm 0.07$	$2.20 \pm 0.12$	$0.65 \pm 0.07$	$0.086 \pm 0.001$
19	J232653.15+002142.9	2.190	0.5624	$4.37 \pm 0.46$	$5.22 \pm 0.55$	$4.29 \pm 0.76$	$2.00 \pm 0.23$	$0.013 \pm 0.007$
20	J233548.62-023734.3	1.234	0.5081	$3.76 \pm 0.10$	$3.57 \pm 0.10$	$2.54 \pm 0.11$	$1.15 \pm 0.13$	$0.047 \pm 0.002$
21	J233818.25-005610.5	0.894	0.4801	$3.05 \pm 0.12$	$2.74 \pm 0.10$	$1.95 \pm 0.31$	$0.51 \pm 0.08$	$-0.018 \pm 0.003$
Targets without SALT spectrum								
22	J093020.60+001828.0 <sup>d</sup>	2.4300	0.5928	$3.48 \pm 0.25$	$3.58 \pm 0.25$	$2.90 \pm 0.22$	$1.75 \pm 0.36$	$-0.101 \pm 0.004$
23	J101610.82+075209.1	2.187	0.5961	$3.09 \pm 0.38$	$3.62 \pm 0.45$	$2.04 \pm 0.20$	$1.31 \pm 0.17$	$0.028 \pm 0.006$
24	J102510.10-004644.9 <sup>d</sup>	2.212	0.5561	$3.22 \pm 0.11$	$2.80 \pm 0.10$	$2.05 \pm 0.08$	$0.97 \pm 0.07$	$0.037 \pm 0.001$
25	J103059.75-013237.7	2.155	0.5783	$3.27 \pm 0.10$	$3.20 \pm 0.10$	$2.39 \pm 0.11$	$0.49 \pm 0.01$	$-0.024 \pm 0.001$
26	J110817.93+062833.0	1.202	0.5721	$3.02 \pm 0.16$	$2.89 \pm 0.15$	$1.72 \pm 0.33$	$0.49 \pm 0.16$	$0.023 \pm 0.004$
27	J114614.24-023716.1	2.207	0.5295	$4.13 \pm 0.22$	$3.22 \pm 0.17$	$\leq 0.59$	$\leq 0.91$	$-0.227 \pm 0.004$
The non-USMgII absorber in our lines of sight								
28	J111400.00-002342.6	0.952	0.7981	$2.15 \pm 0.18$	$1.88 \pm 0.16$	$1.37 \pm 0.16$	$0.42 \pm 0.09$	$0.084 \pm 0.006$

<sup>a</sup> Host galaxy of this USMgII system was studied by [Rahmani et al. \(2016\)](#) using both spectroscopy and multiband photometry

<sup>b</sup> The environment of this system was explored in [Nestor et al. \(2007\)](#) using multiband photometry.

<sup>c</sup> A group of 4 galaxies associated to this USMgII was studied by [Gauthier \(2013\)](#) using both spectroscopy and multiband photometry.

<sup>d</sup> These systems are part of the GOTOQ sample of [Joshi et al. \(2017\)](#).

quasar within a couple of nights of our observations. Once the flux calibration is done, we apply the air to vacuum wavelength transformation and also correct for the heliocentric velocity.

Since we could only observe 21 out of 27 systems, we first establish that the observed sub-sample represents an unbiased population of the original sample. We performed the two-sample Kolmogorov-Smirnov (KS) test between the parent and the observed sub-sample based on the absorption line properties [such as the rest equivalent width of Mg II  $\lambda$  2796 ( $W_{2796}$ ), the doublet ratio of Mg II doublet ( $W_{2796} / W_{2803}$ ),  $W_{2600} / W_{2796}$  (referred to as  $\mathcal{R}$ ), and the absorption redshift ( $z_{\text{abs}}$ )]. Results of the KS test are summarised in Table 3. For each of the absorption properties, we find that the p-value of the KS test, i.e., the probability of both the samples (parent and the observed) being drawn from the same underlying population is very close to 1, which implies that purely based on absorption line properties the observed sub-sample essentially represents an unbiased population of the parent sample.

### 3.1 Survey completeness

We consider deeper images and photometric redshifts available in DECaLS galaxy catalogs ([Dey et al. 2019](#)) to quantify completeness of our sample at the faintest magnitude levels (i.e.  $m_r < 23.6$ ). In Table C1 in the appendix, we summarize details of all the galaxies in DECaLS, within an impact parameter of 100 kpc and photometric redshift consistent with the  $z_{\text{abs}}$  for the USMgII in our sample. First we consider the 36 (26 if  $m_r < 22.5$ ) galaxy candidates within  $D \leq 50$  kpc. For 12 USMgII absorbers there is only a single identified galaxy. Our observational completeness is 92% (one galaxy not observed) and spectroscopic measurement completeness is 83% (i.e. 10/12). For six USMgII absorbers we have two galaxy candidates available within 50 kpc. In 3 cases both the galaxies are observed and in the remaining 3 cases only the brightest galaxy is targeted. But the galaxies unobserved were fainter than 22.5 mag and not visible in the SDSS. Therefore, the observational completeness is 75% (100%) for the limiting magnitude  $m_r = 23.6$  (22.5) mag. We measure the redshifts of 7 of the 9 targeted galaxies. Therefore, the redshift measurement completeness is 58% (78%) for the limiting magnitude

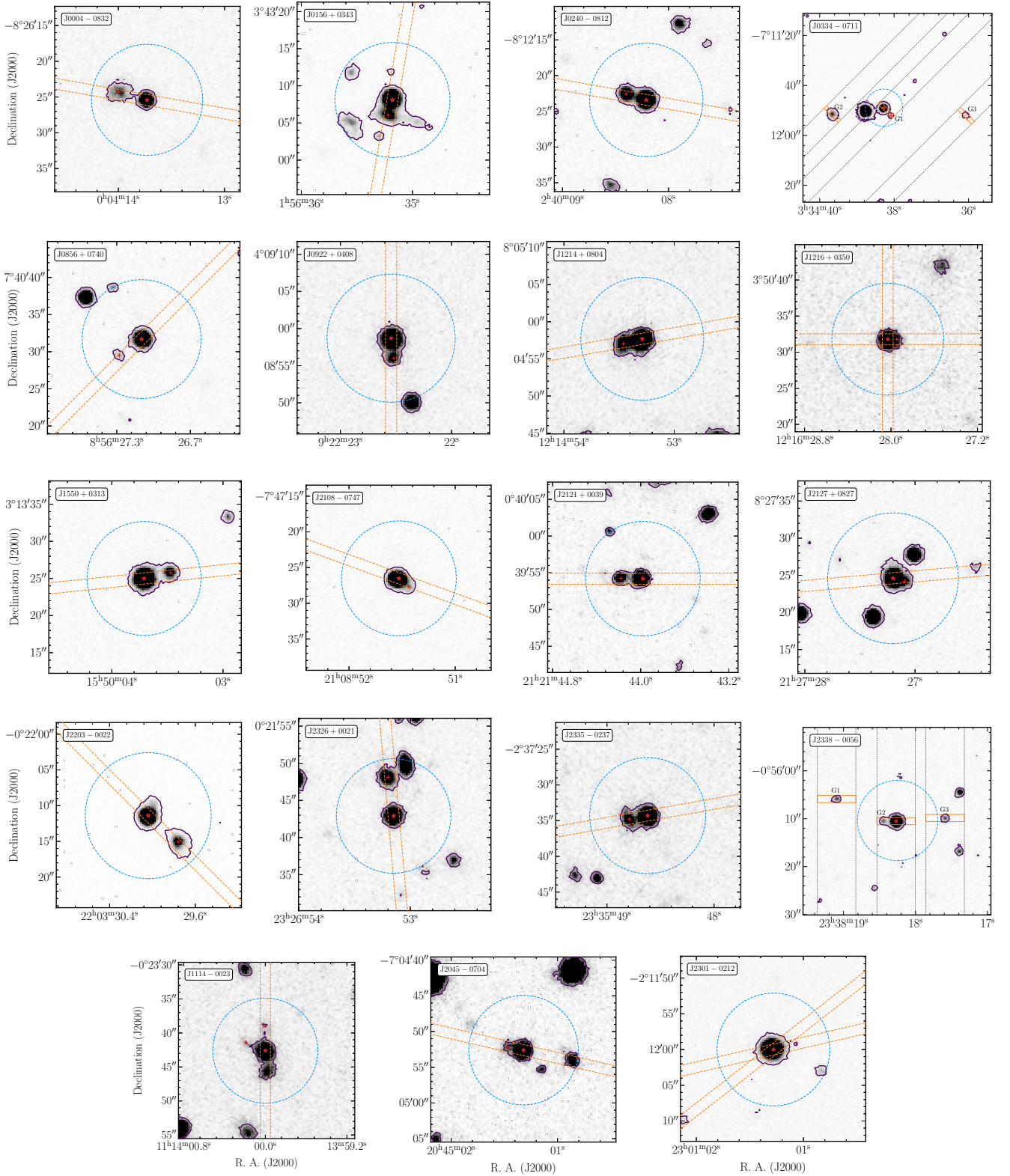


**Figure 2.** The DECaLS r-band images of the observed USMgn fields, except for the systems J2207-0901 and J0218-0832 that have been studied in detail by [Gauthier \(2013\)](#) and [Rahmani et al. \(2016\)](#) respectively. In each of these fields, the quasar sits at the centre and is marked with a red star while in the case of detection, the centre of the associated USMgn host galaxy is marked with a red plus sign. The contours correspond to the  $3\sigma$  noise level on top of the mean background counts. The blue dashed circle corresponds to the circle with a radius 50 kpc around the quasar. Our SALT programme aims to obtain redshifts of potential galaxies within 50 kpc. The parallel red dashed line corresponds to the slit of width  $1.5''$  used during the SALT observations. For two fields J0334-0711 and J2338-0056 multiple potential galaxies are seen and were targeted using MOS. The GOTOQ system, J1216+0350, has been observed with two different slit position angles to constrain the impact parameter by the method of triangulation using the  $[O\text{II}]$  emission line. The 16 systems in the first 4 rows correspond to detections while the 3 systems presented in the last row are non-detections. The potential host galaxies based on the photo redshifts in the cases of non-detections are marked with red '+' sign. For the USMgn system, J1114-0023, we have marked the Mg II absorbing galaxy at  $z_{\text{abs}} \sim 0.7981$  ( $W_{2796} = 2.15\text{\AA}$ ) with red 'x'.

**Table 2.** Log of observations for our USMgII sample. Systems marked with \* represent non-detection of any associated host galaxy, while systems marked with + represent cases where the host galaxy sits on top of the quasar along the line of sight (see text for more details). The last two columns correspond to the number of other candidate galaxies within  $50 \leq D[\text{kpc}] \leq 100$  and  $D \leq 50$  kpc with  $m_r \leq 22.5$  based on SDSS photometry.

No.	Quasar	Date	Exposure (s)	Observation Mode	PA (deg.)	Grating Angle (deg)	Wavelength Range ( $\text{\AA}$ )	Other candidate galaxies ( $50 \leq D[\text{kpc}] \leq 100$ )	Total candidate galaxies ( $D \leq 50$ kpc)
(1)	(2)	(3)	(4)	(5)	(6)	(7)	(8)	(9)	(10)
1	J000413.73-082625.4	2017-07-18	2400	Long-slit	80	17.75	5200 – 8200	0	1
		2017-09-17	2400	Long-slit	80	17.75	5200 – 8200		
2	J015635.18+034308.1	2015-11-07	2500	Long-slit	350	17.00	4900 – 7900	0	5
		2015-11-13	2500	Long-slit	350	17.00	4900 – 7900		
3	J021820.10-083259.4	2016-01-10	2500	Long-slit	80	18.125	5300 – 8300	0	1
4	J024008.21-081223.4	2018-10-05	2500	Long-slit	80	17.75	5200 – 8200	0	1
5	J033438.28-071149.0	2017-11-19	2300	MOS	44.8	17.75	5200 – 8200	0	1
		2017-12-11	2300	MOS	44.8	17.75	5200 – 8200		
6	J085627.09+074031.7	2018-02-09	2200	Long-slit	315	17.00	4900 – 7900	0	1
		2018-02-10	2200	Long-slit	315	17.00	4900 – 7900		
7	J092222.58+040858.7	2016-02-08	2400	Long-slit	0	16.625	4800 – 7800	0	1
		2016-03-01	2400	Long-slit	0	16.625	4800 – 7800		
8	J111400.00-002342.6	2021-04-15	2580	Long-slit	0	18.125	5300 – 8300	1	1
9	J121453.29+080457.7	2016-04-09	2300	Long-slit	100	17.375	5050 – 8050	1	1
		2016-03-01	2160	Long-slit	100	17.375	5050 – 8050		
10	J121628.03+035031.8 +	2016-02-05	2400	Long-slit	0	17.75	5200 – 8200	0	1
		2016-02-06	2400	Long-slit	90	17.75	5200 – 8200		
11	J155003.71+031325.0	2015-06-19	2500	Long-slit	96	16.625	4800 – 7800	0	1
		2015-07-14	2500	Long-slit	96	18.125	5300 – 8300		
12	J204501.32-070452.6 *	2017-08-18	2500	Long-slit	77	18.125	5300 – 8300	0	1
13	J210851.53-074726.5 +	2017-06-03	2400	Long-slit	70	17.75	5200 – 5300	0	1
		2017-06-18	2400	Long-slit	70	17.75	5200 – 5300		
14	J212143.98+003954.2	2015-06-20	2340	Long-slit	90	16.625	4800 – 7800	0	1
		2020-10-18	2200	Long-slit	240	18.125	5300 – 8300		
15	J212727.20+082724.6	2015-06-18	2500	Long-slit	95	16.625	4800 – 7800	0	1
		2016-06-20	1844	Long-slit	95	18.125	5300 – 8300		
16	J220330.04-002211.4	2017-09-13	2500	Long-slit	45	17.00	4900 – 7900	0	1
17	J220702.53-090127.7	2017-09-16	2400	Long-slit	77	18.125	5300 – 8300	1	1
18	J230101.28-021200.0 *	2017-10-11	2500	Long-slit	308	18.125	5300 – 8300	0	0
		2017-10-17	2500	Long-slit	283	17.375	5050 – 8050		
19	J232653.15+002142.9	2017-10-17	2500	Long-slit	5	18.125	5300 – 8300	0	1
20	J233548.62-023734.3	2015-06-19	2271	Long-slit	100	16.625	4800 – 7800	0	1
		2015-06-21	2500	Long-slit	100	18.125	5300 – 8300		
21	J233818.25-005610.5	2018-08-21	2200	MOS	90	17.00	4900 – 7900	1	1
		2018-09-11	2324	MOS	90	17.00	4900 – 7900		

**Table 3.** Results of the KS test between the observed sub-sample and the parent sample

Properties	$W_{2796}$	$W_{2796}/W_{2803}$	$W_{2600}/W_{2796}$	$Z_{\text{abs}}$
Statistics (D)	0.101	0.095	0.057	0.127
p-value	0.998	1.000	1.000	0.975

$m_r = 23.6$  (22.5) mag. So for 18 USMgII absorbers discussed above our observational completeness is 79% (90%) and redshift measurement completeness of 71% (81%) for the limiting magnitude  $m_r = 23.6$  (22.5) mag. Our survey completeness for  $D \leq 50$  kpc are summarised in the Table 4.

Next we consider galaxies in the impact parameter  $50 \leq D[\text{kpc}] \leq 100$ , which is important to identify whether the USMgII absorber is part of a galaxy group. It is evident from Table C1 that for 7 USMgII (i.e. 33% of the sample) systems only one galaxy candidate is present. In the remaining 11 cases there are candidate galaxies with impact parameter in the range 50-100 kpc. But good

**Table 4.** Summary of the observational and the redshift completeness of our USMgII survey for  $D \leq 50$  kpc.

Survey	Limiting magnitude ( $m_r$ )	
Completeness	23.6	22.5
Observations	79%	90%
Redshift measurement	71%	81%

fraction of them have  $m_r < 22.5$  mag. In this impact parameter range our search is very much incomplete as we do not target most of these faint sources that also have large errors in the photometric redshifts.

In the case of J0156+0343, there are 6 galaxy candidates present within  $D=50$  kpc, we have spectra of two of these galaxies which have consistent redshifts. Description of this system is presented in detail in section 4.1. In the case of J2203-0022 there are three potential galaxies. We targeted two of them (with the lowest D) and could measure redshift in only one case. No nebular emission was detected in the other case. Note the source that was not observed has

$m_r = 23.5$  mag. In the case of J1114-0023, there are three galaxies within D of 50 kpc. We have not targeted two of these galaxies which are fainter than  $m_r = 22.5$  mag. The galaxy observed by us did not have correct redshift.

#### 4 IDENTIFICATION & PROPERTIES OF THE USMgII HOST GALAXIES

We searched for emission and absorption line signatures of the host galaxies of USMgII systems in the extracted spectra. Apart for 3 cases (shown in the bottom row in Figure 2) we were able to identify at least one galaxy with redshift consistent within  $300 \text{ km s}^{-1}$  with  $z_{\text{abs}}$  of the USMgII systems. For the  $z_{\text{abs}} = 0.5623$  USMgII system towards J2207-0901, Gauthier (2013) have identified 4 potential associated galaxies, the closest galaxy being at an impact parameter of 38 kpc and the farthest being at an impact parameter of 246 kpc. For the USMgII system at  $z_{\text{abs}} = 0.5896$  towards the quasar J0218-0832, Rahmani et al. (2016) have identified the host galaxy at an impact parameter of 16 kpc. For these two cases, we will use their identified galaxies in our work. In the case of the  $z_{\text{abs}} = 0.5311$  USMgII absorber towards J0240-0812 our spectrum confirms the potential host galaxy identified by Nestor et al. (2007) based on photometric redshifts. For the remaining 15 cases, we detect host galaxy(ies) showing at least one emission line among [O II]  $\lambda\lambda$  3727, 3729, [O III]  $\lambda\lambda$  4960, 5008 and H $\beta$   $\lambda$  4862 having consistent redshift with the USMgII absorption.

We have obtained MOS mode observations for two objects (see Figure 2). In the case of  $z_{\text{abs}} = 0.5977$  USMgII systems towards J0334-0711, we could get good spectra of all the three galaxies close to the quasar sightline (see Figure 3). The closest galaxy G1 has a redshift of  $z = 0.5989$  consistent with being the host galaxy of the USMgII system. The measured redshifts of galaxies G2 and G3 are 0.285 and 0.549, respectively, suggesting that they are not associated with the USMgII absorber. The impact parameter of galaxy G3 with respect to the quasar sightline is 211 kpc and we do not detect any Mg II absorption with a  $3\sigma$  rest equivalent with limit of  $0.28\text{\AA}$ . We also used MOS observations for  $z_{\text{abs}} = 0.480$  USMgII absorber towards J2338-0056 using three slits. The galaxy G1 (see Figure 2) has a redshift of 0.4798 and is at an impact parameter of 79 kpc from the quasar sightline. Although both G2 and G3 have photometric redshifts consistent with that of the USMgII absorption, we did not get spectra of sufficient SNR ( $\text{SNR} < 3$ ) to be able to measure their spectroscopic redshifts. While redshift of G1 is consistent with  $z_{\text{abs}}$ , we do not consider this galaxy in our correlation analysis as G2 could be the real host galaxy at an impact parameter of 18 kpc.

As seen in Figure 2, for 13 cases (i.e., 12 objects listed in Table 6 plus the host galaxy identified for  $z_{\text{abs}} = 0.4801$  absorber towards J233818.25-005610.5), the host galaxies are photometrically separated from the background quasars in the SDSS photometry. In the SALT observations as well, we were able to get the galaxy spectra without any contamination from the quasar emission in these cases. We matched our spectroscopic measurements with the r- and i-band fluxes of the host galaxies to correct for the fact that our slit might not have covered the whole galaxy. For four galaxies (associated with absorbers along the lines of sight towards J0156+0343, J1216+0350, J2108-0747 and J2127+0827), for which we can not directly compare the photometric flux of the USMgII host galaxies with its spectroscopic flux due to the quasar contamination, we compare the quasar spectrum obtained from the SALT and SDSS to estimate the flux-loss of the quasar. For these four systems, we

assumed that the slit-loss suffered by the galaxy light is the same as that of the quasar.

In addition, we have detected the stellar/interstellar Ca II  $\lambda\lambda$  3935, 3970 absorption and strong H I Balmer absorption lines in the spectra of 5 USMgII host galaxies. These galaxies are also identified in Table 5. Recently, it has been found that in about 88% of all the red galaxies that shows [O II] emission lines, the excitations are due to various types of AGN, mostly the low ionization nuclear emission-line regions (LINERS, 63%) (Yan et al. 2006; Kocevski et al. 2011). However, Yan & Blanton (2012) based on the spatial extension of the emitting regions rule out AGN contribution in LINER like emission in passive galaxies. Observing [N II] and H $\alpha$  emission lines is important to quantify any contribution of AGN in cases where we have indications of old stellar populations.

As mentioned above, there are three GOTOQs in our sample. To check whether there is any faint emission from galaxies close to the QSO sightline in other cases as well, we searched for the average [O II] emission from the remaining 24 USMgII systems within the SDSS fibre using a median stacked spectrum. We detect a signal at the expected position of the [O II] emission at the  $2\sigma$  level. Upon careful investigation, we notice that this stacked emission is mainly dominated by four systems ( $z_{\text{abs}} = 0.5509$  towards J2121+0039,  $z_{\text{abs}} = 0.4392$  towards J2127+0827,  $z_{\text{abs}} = 0.5961$  towards J1016+0752 and  $z_{\text{abs}} = 0.5610$  towards J1114-0023). Note none of them are in the GOTOQ sample of Joshi et al. (2017) as the emission lines are seen at a lesser significance level in individual spectrum. In the case of J2121+0039, our observations confirm the presence of the host galaxy close to the QSO sightline. Similarly, also for J2127+0827, we identify the host galaxy close to the QSO sightline. In the case of J1114-0023, available images show the presence of a galaxy ( $m_r = 21.2$  mag) along the slit very close to the quasar (identified with + in Figure 2). Our long-slit spectra did not show any nebular emission from this galaxy. However, we detect an emission line galaxy with  $z_{\text{em}} = 0.7983$  at an impact parameter of 22.4 kpc (marked with a cross in Figure 2) associated with the  $z_{\text{abs}} = 0.7981$  Mg II system. While this is not an USMgII system, we measure all its properties also.

The fourth system,  $z_{\text{abs}} = 0.5961$  towards J1016+0752, has not been observed with SALT. However, upon careful inspection, we identify clear signatures of [O II]  $\lambda\lambda$  3727, 3729, [O III]  $\lambda\lambda$  4960, 5008 nebular emission lines in the SDSS spectrum. Hence, this is essentially a GOTOQ system but in the Pan-STARRS photometry, we did not identify any detectable extension around the background quasar. When we repeated the stacking exercise for the remaining systems, we did not find any detectable [O II] emission with at least  $2\sigma$  significance.

#### 4.1 Galaxy parameters from spectroscopy

In Table 5, we summarize properties of the identified host galaxies derived from our flux calibrated spectra after applying the corrections as explained above. In column 3 of this table, we provide the host galaxy redshift measured using [O II] lines. In this case, we fitted the line with double gaussians having the same redshift and velocity width. The flux ratio of the two lines is kept as a free parameters and allowed to vary between 0.34 and 1.50. Columns 6, 7 and 8 provide the measured fluxes of [O II], H $\beta$  and [O III] emission lines. The  $3\sigma$  upper limits are provided in the case of non-detections, and ‘-’ indicates that the measurements are not possible with our spectra because of poor background subtraction due to the skylines present.

The measured impact parameter (D, the projected separation of the host galaxy with respect to the quasar sightline) for host



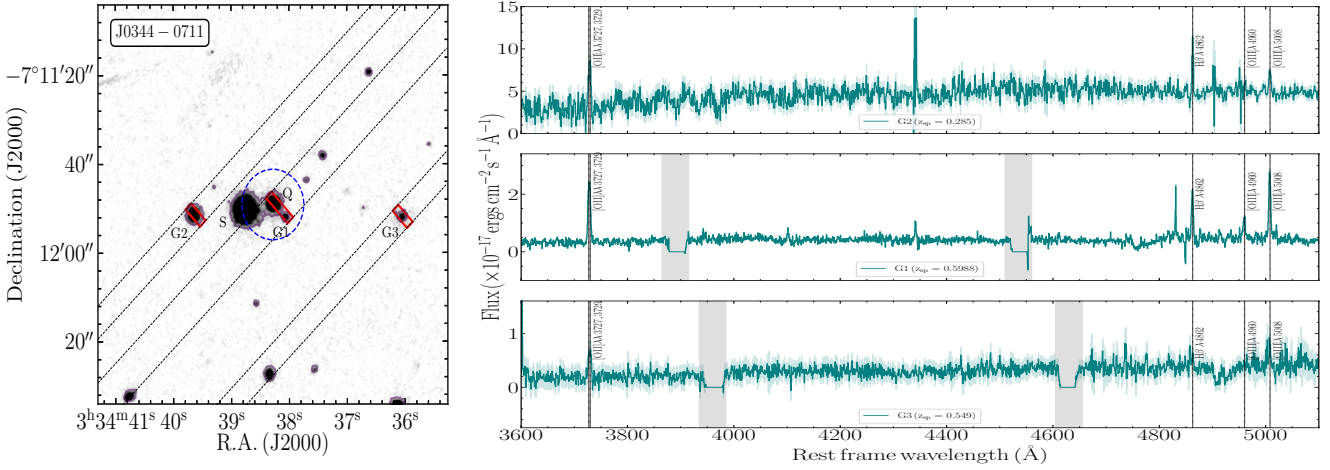


**Figure 3.** Left panel: the observational configuration for Multi Object Spectroscopy (MOS) mode observations of the USMgII system J0334-0826. The blue dashed circle represents a projected distance of 50 kpc across the quasar at the absorption redshift. Three nearby galaxies (named ‘G1’, ‘G2’ and ‘G3’) having photometric redshifts consistent with the redshift of the USMgII systems were targeted. Rest frame galaxy spectra of these galaxies are shown in the right panel. Since the galaxy ‘G2’ was also observed with SDSS, here we display the SDSS spectrum owing to a superior SNR. The black dashed vertical lines mark the locations of nebular emission lines confirming the redshift of these galaxies. The measured redshifts of the galaxies ‘G1’, ‘G2’ and ‘G3’ are 0.5989, 0.285 and 0.549 respectively. Only galaxy ‘G1’ is consistent with the absorption redshift and hence, is assumed to be associated with the USMgII absorption.

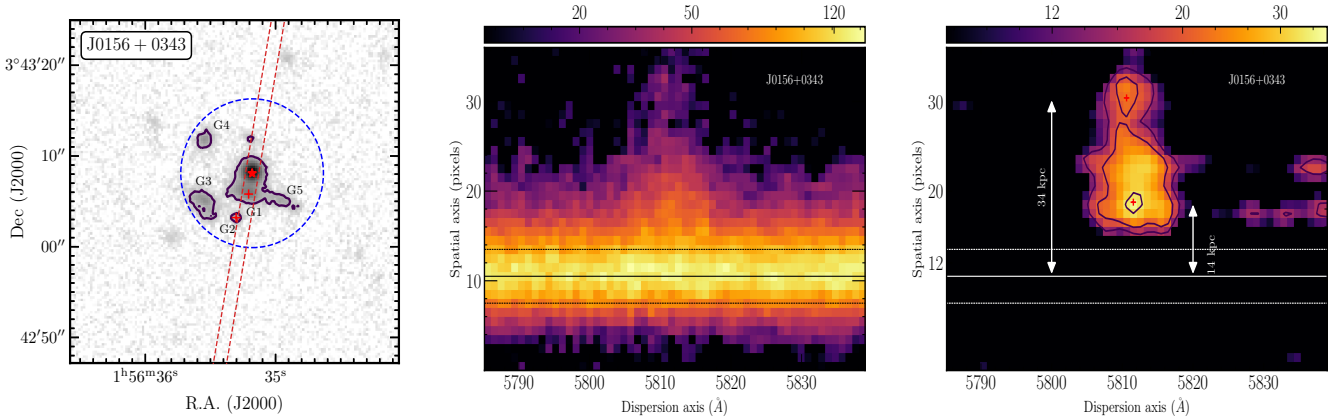


**Figure 4.** Left panel: DECaLS r-band image of J0156+0343 with the slit position shown with red dashed lines. We identify 5 possible galaxies within 50 kpc to the quasar sightline (blue circle). Middle and Right panels show the 2D spectrum before and after the continuum subtraction. We detect [O II] emission associated with G1 ( $D = 14$  kpc) and G2 ( $D = 34$  kpc) indicated by “+” in the figure. G5 could be interacting strongly with G1. We also see strong [O II] emission in between G1 and G2 that could be related to the gas expelled from the interaction between G1 and G5. Photometric redshifts of G3 and G4 are  $0.455 \pm 0.106$  and  $0.524 \pm 0.112$  respectively, that are also consistent with that of the USMgII absorption.

galaxies of USMgII are listed in the fifth column of Table 5. In cases where the host galaxy is well-separated from the quasar sightline, we measure the impact parameter using the coordinates of the centroids of the galaxy and the quasar.

The USMgII system at  $z_{\text{abs}} = 0.5519$  towards J1216+0350 is one of the GOTOQs in our sample with the SDSS spectrum of the quasar showing [O II], [O III] and H $\beta$  emission lines, at the absorption redshift, detected at  $> 3\sigma$  confidence. In the Pan-STARRS images, we do not find any significant extension of the background quasar continuum due to the foreground galaxy. Hence, to constrain the impact parameter, we obtained the SALT spectrum by keeping the slit at two position angles (i.e. PA =  $0^\circ$  and  $90^\circ$ ). In the left most panels of Figure 5, we present the 2D spectrum of this quasar obtained along PA =  $90^\circ$  before (top panel) and after (bottom panel) subtracting the quasar continuum. We removed the quasar flux from the 2D spectra by linearly interpolating the quasar flux measured over 35 on both

sides of the [O II] emission. It is evident that the [O II] emission is well-separated from the QSO along PA =  $90^\circ$ . The bottom panel also displays the  $3\sigma$  contour about the median and the centroid is marked with a ‘+’. Based on this we, constrain the impact parameter to be 8.1 kpc. Due to poor spectral point spread function, we were unable to use the spectra obtained at PA =  $0^\circ$  to further refine the position of the [O II] emission. Interestingly, we find a galaxy at an impact parameter of 302 kpc with redshift  $z = 0.5527$  within 490  $\text{kms}^{-1}$  of this USMgII absorber in the SDSS catalog. However, it is most likely that this galaxy is unrelated to the USMgII absorber as it is at a larger impact parameter and has a much higher velocity separation relative to the USMgII absorption, compared to the galaxy at an impact parameter of 8.1 kpc.

In the remaining two cases,  $z_{\text{abs}} = 0.5187$  towards J2108-0747 and  $z_{\text{abs}} = 0.4392$  towards J2127+0827, while the host galaxies are not distinctly visible, their quasar images show extensions (see

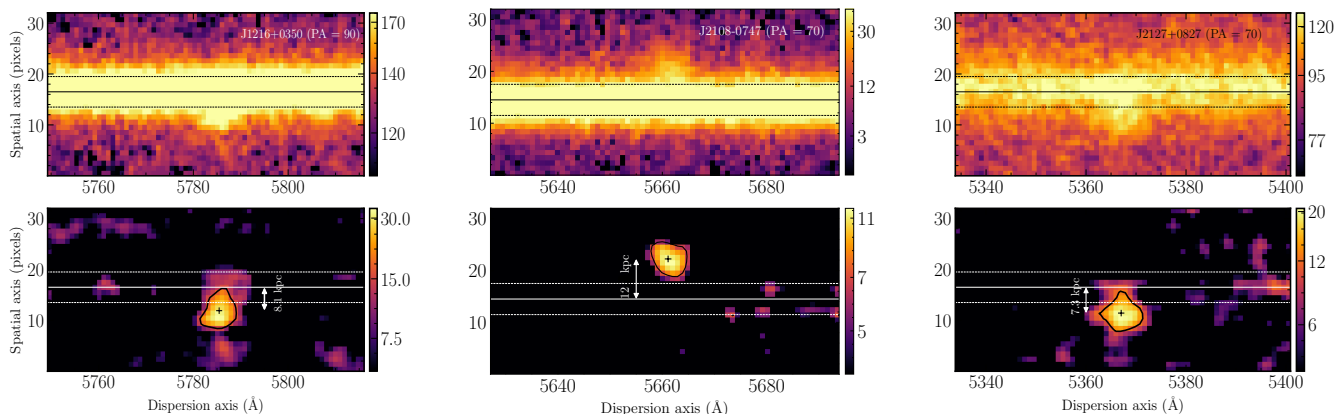


**Figure 5.** An illustration of the procedure for determining the impact parameter for USMgII systems with the host galaxies at low impact parameter to the background quasar. Observed and continuum subtracted 2D spectra are shown in the top and bottom panels respectively. In the left most panel, we show the continuum subtracted 2D spectrum of J1216+0350. [O II] emission is clearly detected with an off-set of 1.27 arc sec from the quasar trace (solid horizontal line). This corresponds to an impact parameter of 8.1 kpc (see section 4.1 for details). The solid black contour corresponds to the  $3\sigma$  noise level on top of the mean background. Similar plots for J2108-0747 and J2127+0827 are shown in the middle and right panels respectively.

Figure 2). We observed these targets keeping the slit aligned to these extended features and detected emission lines well-detached from the quasar trace in both cases. After subtracting the quasar contribution in the 2D image, we estimate the impact parameters to be 12 and 7.3 kpc, respectively, for J2108-0747 and J2127+0827 (see Figure 5).

For the case of USMgII absorption at  $z_{\text{abs}} = 0.5581$  along the line of sight to J0156+0343, we identify a group of 5 galaxies (among which a merger is possibly present) close to the line of sight (see Figure 4). The nearest galaxy G1 could be part of a tidally interacting pair with G5. In our slit spectrum we detect [O II] emission from the galaxy G1 ( $D=14$  kpc) and G2 ( $D=34$  kpc). We also detect [O II] emission between these two galaxies. The galaxies G3, G4 and G5 have photometric redshifts  $0.455 \pm 0.106$ ,  $0.524 \pm 0.112$  and  $0.488 \pm 0.104$  respectively. Thus, this absorber is most likely to originate from gas associated with a group of interacting galaxies.

#### 4.2 Galaxy parameters from SED fitting:

Next we measure the host galaxy properties such as B-band absolute magnitude and luminosity ( $M_B$  and  $L_B$ ), stellar mass ( $M_*$ ), star formation rate (SFR) and specific star formation rate (sSFR) using available spectroscopic and photometric data and template fitting methods. Since the USMgII host galaxies are at low impact parameters to the quasar sightline, we model the quasar image using the appropriate SDSS point spread function (Xin et al. 2018), and then subtract it from the original image before extracting the parameters of the host galaxies. The procedure for modeling and subtracting the PSF for the USMgII system J0004-0826 is shown in Figure 6. We measure the flux of the host galaxy in different photometric passbands and correct for finite telescope gain using standard approaches presented in the SExtractor software (Bertin & Arnouts 1996) and the python fork of the software, Source Extraction and Photometry (Barbary 2016).

We make use of the publicly available python package, Bayesian Analysis of Galaxies for Physical Inference and Parameter Estimation (BAGPIPES; Carnall et al. 2018), to extract the galaxy parameters. We consider the stellar population models by Bruzual & Charlot (2003), constructed assuming the Kroupa & Boily (2002) IMF, and recently updated by Chevallard & Charlot (2016) to include the MILES stellar spectral library (Falc3n-Barroso et al. 2011) and an

updated stellar evolutionary track (Marigo et al. 2013). We used the default implementations of nebular emission, dust and IGM attenuation in BAGPIPES. More details of modeling and fitting the galaxy SED to the spectroscopic/photometric data using BAGPIPES can be found in section 3.1 of Carnall et al. (2018).

To start with, we fix the redshift of the galaxies to their spectroscopic redshifts. We assume that all stars within the galaxy have the same metallicity, and vary it with a uniform prior in the range 0.01 – 2.5 of the solar metallicity. We parameterize the star formation histories (SFHs) using the delayed exponential model. We also chose a flat prior for the logarithm of the total stellar mass formed, in the units of solar mass in the range 0 – 13. It is known that derived parameters depend on our choice of SFH. Using BAGPIPES, Carnall et al. (2019) have obtained the  $M_*$ , SFR, dust attenuation and metallicity posteriors for the galaxies to lie within  $1 - 2\sigma$  of the original values in the mock catalog with four different kinds of SFHs (an exponentially declining SFH, delayed exponentially declining SFH, a log-normal SFH and, a double power law SFH) with a bias of about 0.1 dex in  $M_*$  and a bias of 0.2 dex in SFR. We shall keep this in mind while discussing these parameters. The whole process is demonstrated in Figure 6 for the USMgII system J0004-0826. In the top panel, we show the QSO field in the left and the observed spectrum in the right panels. In the bottom panels, we show the QSO image (left), model PSF (middle) and the galaxy image after subtracting the model QSO PSF (right). In the top left panel, we overlay the best fitted SED on the observed spectrum. This clearly reproduces all the absorption and emission lines and the stellar continuum very well.

The model parameters for the best fitted case are summarized for 12 USMgII host galaxies, where the host galaxies are photometrically separable from the background quasars in Table 6. For each USMgII system, this table provides, coordinates of the background quasars and the USMgII host galaxies (columns 1 and 2), inferred stellar mass, rest frame B-band absolute magnitude, rest frame B-band luminosity and SFR in columns 2, 4, 5 and 6 respectively. The stellar mass of the USMgII host galaxies is in the range,  $10.21 \leq \log(M_*/M_\odot) \leq 11.62$ , with a median value of  $\log(M_*/M_\odot) = 10.64$ . We convert the stellar mass to the dark matter halo mass ( $M_h$ ) using the stellar-to-halo mass relation provided by Girelli et al. (2020). Halo masses and the corresponding virial radius,  $R_h$  (we use

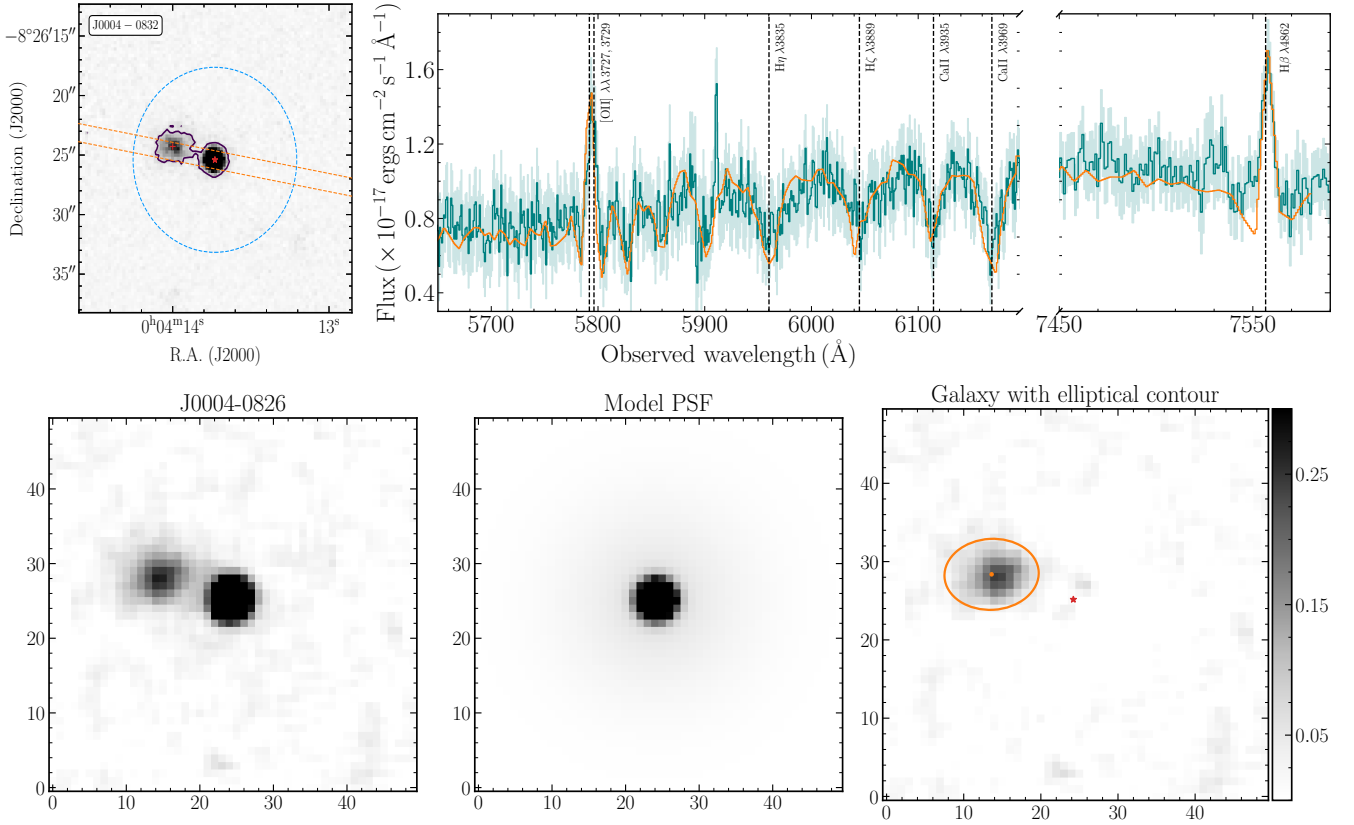


**Figure 6.** *Top left:* The DECaLS r-band image of the observational configuration, with the background quasar and the targeted galaxy marked with symbols, ‘★’ and ‘+’, respectively, for the USMgII system at  $z_{\text{abs}} = 0.5544$  towards J0004-0826. The blue dashed circle corresponds to a projected radius of 50 kpc at the redshift of the host galaxy around the quasar. **Red dashed lines show the slit orientation used in our spectroscopic observations.** *Top right:* observed spectrum of the galaxy in cyan-green colour with different emission and absorption lines marked using vertical dashed lines. The synthetic spectrum obtained from the SED fitting exercise, resampled at the observed wavelengths, is overplotted on top of the observed galaxy spectrum (orange). The bottom panels demonstrate the process of modeling and subtracting the quasar PSF from the SDSS photometry to obtain the galaxy fluxes. *Bottom left:* The actual  $50'' \times 50''$  SDSS i-band image of the quasar J0004-0826. *Bottom middle:* the model QSO image obtained by the fitting the quasar image with the SDSS PSF. *Bottom right:* Residual image after the pixel-by-pixel subtraction of the middle panel from the left panel. The orange ellipse presents the inclination and the orientation of the galaxy obtained from fitting the galaxy image. The red ‘•’ and ‘★’ mark the center of the galaxy and the quasar respectively.

$R_{200}$  for this purpose), associated with the USMgII host galaxies are given in column 8 and 9 respectively.

Next we estimate the B-band luminosities using the synthetic spectrum obtained from the SED fitting of the USMgII host galaxies. First, we de-redshift the synthetic spectrum to its rest frame by conserving the total energy and then we calculated the rest frame B-band flux by appropriately weighting the B-band filter transmission curve. Following the prescription of Fukugita et al. (1995), we convert this flux to the absolute magnitude of the galaxy (given in column 4 of Table 6). Then we determined the B-band luminosity of these galaxies by comparing their magnitude with the solar magnitude and luminosity. These values are summarized in column 5 of Table 6. The USMgII host galaxies have absolute B-band magnitude between -19.05 and -21.68, with a median value of -20.49. Only two of the galaxies are brighter than the characteristic B-band luminosity of the field galaxies at redshift  $z = 0.5$  ( $M_B^* = -21.15$ ; Faber et al. 2007).

Further, for a set of isolated host galaxies of Mg II systems, (defined as host galaxies without any nearest neighbor within 100 kpc and velocity separation within  $500 \text{ km s}^{-1}$ ) from the MAGIICAT survey (Nielsen et al. 2013a), we calculated the rest-frame B-band absolute magnitudes from the synthetic spectrum obtained from the SED fitting, and compared them against the values provided in

the MAGIICAT survey and found them to be consistent. We also calculated the galaxy parameters for the host galaxies identified in the MAGIICAT survey. Although in the MAGIICAT survey, the impact factor goes up to 200 kpc, we are particularly interested in the galaxies with a smaller impact parameter, as isolated USMgII host galaxies identified in the combined sample of our work and from the literature have a maximum impact parameter of 53.8 kpc. Therefore, we consider the isolated Mg II absorption systems from the MAGIICAT survey up to 60 kpc. For these galaxies, we find  $8.65 \leq \log(M_*/M_\odot) \leq 12.12$ , with a median value of  $\log(M_*/M_\odot) = 10.51$ . In the MAGIICAT survey, there are a total of 98 isolated Mg II host galaxies within the impact parameter of 60 kpc, out of which 76 are observed and identified as photometric sources in the SDSS photometric survey. In the following sections, we will be comparing the host galaxy parameters of our USMgII absorbers with those obtained for these galaxies.

## 5 RESULTS

In this section, we discuss the properties of identified USMgII host galaxies and compare them with that of GOTOQs (Joshi et al. 2017), Mg II host galaxies identified in surveys like MAGIICAT (Nielsen

et al. 2013a), MAGG (Dutta et al. 2020), MEGAFLOW (Schroetter et al. 2019) and SIMPLE (Bouché et al. 2007). We also explore possible correlations between the observed properties of galaxies and absorption lines. However, one has to keep in mind that our survey of USMgII host galaxies, GOTOQs, MEGAFLOW and SIMPLE are ‘absorber-centric’ surveys, i.e., aimed at studying the host galaxies of known absorption systems. MAGG survey, on the other hand, is a ‘galaxy-centric’ survey, i.e., aimed at understanding the gas distribution around a population of galaxies while MAGIICAT is a combination of both types from the literature.

### 5.1 USMgII systems and star forming galaxies:

We have identified host galaxies in the case of 18 out of 21 (i.e.  $\sim 86\%$ ) USMgII absorbers listed in Table 2. Only for one (i.e.  $z_{\text{abs}} = 0.5896$  towards J0218-0832) of these 18 USMgII absorbers (listed in Table 5) the host galaxy does not show [O II] emission. The galaxy redshift in this case was measured based on absorption lines and a weak H $\alpha$  emission (Rahmani et al. 2016) corresponding to a SFR of  $0.42 M_{\odot} \text{ yr}^{-1}$ . Moreover, at least for 16 (i.e., excluding  $z = 0.4801$  absorber towards J2338-0056) out of 21 USMgII absorbers (i.e., all the USMgII systems for which we have host galaxy observations listed in Table 2) the identified host galaxies clearly show detectable nebular emission lines indicating an on-going star formation. The [O II] based SFR are higher than  $1 M_{\odot} \text{ yr}^{-1}$  in 14 galaxies. From the 21 systems discussed above and the two GOTOQs J1025-0046 and J0930+0018 that were not observed with SALT, we can conclude at least  $\sim 70\%$  of the USMgII absorbers (i.e. 16/23) are associated with star forming galaxies (i.e.,  $\text{SFR} > 1 M_{\odot} \text{ yr}^{-1}$ ) and between 4.8–30% of the absorbers are hosted by passive galaxies.

Among the three non-detected cases (USMgII absorption towards J2045-0704 at  $z_{\text{abs}} = 0.5649$ , J2301-0212 at  $z_{\text{abs}} = 0.5367$ , and J1114-0023 at  $z_{\text{abs}} = 0.5610$ ), for the first two cases we obtained the upper limits on  $L_{[\text{O II}]}$  (or SFR) assuming the targeted potential USMgII host galaxies are indeed the USMgII host galaxies (see last row of Figure 2). To calculate the upper limit on the SFR, we first remove the quasar trace from the 2D spectrum around the region of the expected [O II] emission as discussed in 4.1. Then we selected a 2D rectangular patch centered on the expected [O II] emission having width equal to the typical width of the [O II] emission line (FWHM =  $350 \text{ km s}^{-1}$ ) in our sample and height equal to the FWHM of spectral PSF obtained by fitting the quasar trace. Next, we calculated the total counts within this rectangular patch by summing over all the pixel counts that happens to fall within this patch. We convert this to [O II] flux using our flux calibration solutions. The  $3\sigma$  upper limits on  $L_{[\text{O II}]}$  for the host galaxies of the USMgII absorbers along the line of sight to J2045-0704 and J2301-0212 are 0.76 and  $1.12 \times 10^{41} \text{ erg s}^{-1}$  respectively. For the USMgII system J1114-0023, the targeted galaxy turns out to be a high redshift galaxy and from the DECaLS photometry, we find that the galaxy with the consistent photometric redshift of the USMgII absorption sits outside our slit.

In their SINFONI Mg II Program for Line Emitters (SIMPLE), Bouché et al. (2007) have identified host galaxies of 6 USMgII systems at  $0.8 < z < 1.0$  out of 8 systems searched for H $\alpha$  emission. Nestor et al. (2011b) also have identified the host galaxies associated with two USMgII absorption systems at  $z_{\text{abs}} \sim 0.7$  (i.e.  $z_{\text{abs}} = 0.7646$  system towards 0747+305 and  $z_{\text{abs}} = 0.669$  towards Q1417+011). Both the USMgII absorption were associated with a pair of starburst galaxies in the impact parameter range of 29–61 kpc. In the MAGIICAT full sample there is only one USMgII system (i.e.  $z_{\text{abs}} = 0.836627$  towards J000448.11–415728.8 from Guillemin &

Bergeron 1997). The measured impact parameter in this case is 53.8 kpc, and the galaxy does not show detectable [O II] emission.

Dutta et al. (2020) have identified a total of 53 galaxies either in an isolated or in a group environment, associated with 21 Mg II absorbers out of a total sample of 27 Mg II absorbers spanning a range in  $W_{2796}$  of  $0.02 - 3.2 \text{ \AA}$  at  $0.8 \leq z \leq 1.5$ . This gives a host galaxy detection rate of 78 % that is 90% complete down to a [O II] flux limit of  $3 \times 10^{-18} \text{ erg s}^{-1} \text{ cm}^{-2}$ . Only one USMgII system is present in this sample associated with an isolated galaxy with an impact parameter of 18 kpc. Schroetter et al. (2019) have identified at least one host galaxy using the [O II] emission line associated with 59 strong Mg II absorbers ( $W_{2796} \geq 0.3$ ), with a detection rate of about 75% out of the 79 strong Mg II absorption systems present along the line of sight of 22 quasars they studied as a part of their MEGAFLOW survey using the MUSE IFU. Their  $5\sigma$  detection limit is  $\sim 4 \times 10^{-18} \text{ erg s}^{-1} \text{ cm}^{-2}$ . There are three USMgII absorbers in this sample, with all of them associated with isolated [O II] emitting galaxies with impact parameters in the range 9.1–24.5 kpc.

We summarize the details of USMgII systems from the literature in Table F of the appendix. Out of these 14 USMgII literature systems, host galaxies of 13 (i.e.  $\sim 93\%$ ) show nebular emission lines with SFR in excess of  $2 M_{\odot} \text{ yr}^{-1}$  (see last column in Table F).

In the same redshift range as our USMgII sample, Rahmani et al. (2016) have detected host galaxies of DLAs and sub-DLAs with a success rate of 78% at an impact parameter of 10–30 kpc, with 71% of the host galaxies showing multiple nebular emission lines [typical limiting flux is in the range  $(1.5 - 6.0) \times 10^{-17} \text{ erg s}^{-1} \text{ cm}^{-2}$ ]. Note that different literature studies have different selection criteria (pre-selection/blind), observing strategy (long-slit/MOS/IFU), sensitivity limit of observations, definition of absorber-galaxy association (i.e. velocity and impact parameter range considered). Despite this, the discussions presented above confirm that the [O II] emission is frequently detected irrespective of  $W_{2796}$ . Motivated by this, we check whether there is any correlation between  $W_{2796}$  and [O II] luminosity in section 5.5.

### 5.2 Velocity difference between the host galaxy and the USMgII absorber

In Figure 7, we plot the histogram of the rest frame velocity offset between the host galaxy and the Mg II absorption. The velocity difference is measured using  $z_{\text{abs}}$  of Mg II absorption seen in the quasar spectrum with respect to the galaxy redshift measured using the [O II] line. The distribution is well fitted with a Gaussian having a mean velocity offset of,  $\mu = 3.48 \pm 5.92 \text{ km s}^{-1}$  with a dispersion of  $\sigma = 71.02 \pm 4.83 \text{ km s}^{-1}$ . All the identified host-galaxies have velocity offset well within  $250 \text{ km s}^{-1}$  to the absorption redshift. Note that the uncertainty in measured galaxy redshift from the [O II] is typically  $60 \text{ km s}^{-1}$ . This figure also shows the distribution of velocity difference found for GOTOQs from Joshi et al. (2017) in the same redshift range. In this case we find  $\mu = -44.05 \pm 6.69 \text{ km s}^{-1}$  with a dispersion of  $\sigma = 73.21 \pm 5.50 \text{ km s}^{-1}$ . Significant albeit small non-zero  $\mu$  value found here is interesting. We will investigate this in more detail using long-slit spectroscopy of bright GOTOQs in our upcoming paper.

Huang et al. (2021) have found  $\mu \sim 0 \text{ km s}^{-1}$  with a dispersion of  $\sigma = 84 \text{ km s}^{-1}$  for their full sample of galaxies associated with Mg II absorbers at  $z = 0.10 - 0.48$ . They also found the dispersion to be larger (i.e.  $\sigma \sim 235 \text{ km s}^{-1}$ ) for the non-isolated galaxies. In the case of the MAGG sample with absorbers at  $0.8 < z < 1.5$ , the measured median velocity difference is  $\mu = -8.0 \text{ km s}^{-1}$  and  $\sigma \approx 62 \text{ km s}^{-1}$  for the single galaxies and  $\approx 208 \text{ km s}^{-1}$  for the group galaxies (Dutta

**Table 5.** Galaxy properties inferred from the observed spectra. Emission line fluxes are given in the units of ( $\times 10^{-17}$  ergs  $\text{cm}^{-2}$   $\text{s}^{-1}$ ).

No.	Quasar	$z_{\text{abs}}$	$z_{\text{gal}}$	D (kpc)	$f_{[\text{O II}] 3728}$	$f_{\text{H}\beta}$	$f_{[\text{O III}] 5008}$	Z	$\log q$	
(1)	(2)	(3)	(4)	(5)	(6)	(7)	(8)	(9)	(10)	
1	J000413.73-082625.4 <sup>a</sup>	0.5544	0.5539	26	4.96±0.71	3.76±0.47	1.80±0.20	8.83 ± 0.04	7.61 ± 0.20	
2	J015635.18+034308.1 <sup>a</sup>	0.5581	0.5590	14	8.73±1.22	≤ 0.60	≤ 0.62	–	–	
3	J021820.10-083259.4 <sup>c</sup>	0.5896	0.5895	16	≤ 2.1	≤ 1.30	≤ 1.70	–	–	
4	J024008.21-081223.4 <sup>a</sup>	0.5311	0.5311	18	6.93±0.96	3.65±0.48	1.98±0.60	8.71 ± 0.08	7.54 ± 0.19	
5	J033438.28-071149.0	0.5977	0.5988	28	23.72±0.56	13.22 ± 0.43	12.08±0.40	8.69 ± 0.07	7.66 ± 0.16	
6	J085627.09+074031.7	0.5232	0.5235	24	1.72±0.24	0.48±0.05	≤ 0.62	–	–	
7	J092222.58+040858.7	0.4549	0.4548	15	19.24±2.80	6.92±0.85	14.51±1.78	8.45 ± 0.09	7.75 ± 0.13	
8	J121453.29+080457.7 <sup>a</sup>	0.4908	0.4911	16	17.35±2.47	6.45±1.29	4.63±0.52	8.60 ± 0.11	7.41 ± 0.14	
9	J121628.03+035031.8 <sup>b</sup>	0.5519	0.5514	8.1	9.39±1.37	2.09±0.23	3.71±0.45	8.47 ± 0.07	7.60 ± 0.10	
10	J155003.71+031325.0 <sup>a</sup>	0.5694	0.5695	23	5.34±0.73	≤ 0.30	–	–	–	
11	J210851.53-074726.5 <sup>b</sup>	0.5187	0.5184	12	2.67±0.36	0.47 ± 0.07	–	–	–	
12	J212143.98+003954.2	0.5509	0.5509	19	9.80±1.10	3.60 ± 0.74	5.30 ± 1.75	8.50 ± 0.13	7.51 ± 0.21	
13	J212727.20+082724.6 <sup>b</sup>	0.4392	0.4397	7.3	10.30±0.72	3.19 ± 0.40	2.17 ± 0.34	8.53 ± 0.07	7.22 ± 0.10	
14	J220330.04-002211.4	0.4381	0.4375	31	47.69±3.21	16.51±0.77	23.60 ± 1.74	8.48 ± 0.10	7.58 ± 0.11	
15	J220702.53-090127.7 <sup>d</sup>	0.5623	0.5621	38	2.82±0.31	–	–	–	–	
			0.5623	55	14.14±0.78	–	–	–	–	
			0.5623	209	14.13±1.57	–	–	–	–	
			0.5604	246	≤ 7.12	–	–	–	–	
16	J232653.15+002142.9	0.5624	0.5621	33	4.61 ± 0.49	≤ 0.88	≤ 1.69	–	–	
17	J233548.62-023734.3	0.5081	0.5080	16	4.47±0.66	≤ 0.53	≤ 0.33	–	–	
18	J233818.25-005610.5 <sup>c</sup>	0.4801	0.4798	79	–	–	–	–	–	
			GOTOQ without SALT observations							
19	J102510.10-004644.9	0.5561	0.5562	≤ 6.45	6.14±1.68	≤ 3.29	≤ 1.98	–	–	
20	J093020.60+001828.0	0.5928	0.5928	≤ 6.5	12.19±2.45	4.23 ± 1.03	8.79±0.97	–	–	
			The non-USMgII absorber in our lines of sight							
21	J111400.00-002342.6	0.7981	0.7983	22.4	1.98 ± 0.25	–	–	–	–	

<sup>a</sup> Galaxy showing strong stellar absorption from Ca II and H I in its spectrum.

<sup>b</sup> The host galaxy is at small angular separation from the QSO and its image merges with that of the galaxy. Although only J1216+0350 is a GOTOQ.

<sup>c</sup> Galaxy information is from [Rahmani et al. \(2016\)](#).

<sup>d</sup> Galaxy information is from [Gauthier \(2013\)](#). We consider the galaxy with the lowest D for correlation analysis involving impact parameters.

<sup>e</sup> There are two potential host galaxies at smaller impact parameters for which we could not get reliable spectra [see Figure 2].

**Table 6.** Properties of the USMgII host galaxies not sitting on top of the background quasars inferred from the SED fitting.

Quasar	Galaxy	$\log(M_{\star}/M_{\odot})$	$M_{\text{B}}$	$[L_{\text{B}}/10^{43}]$ (ergs $\text{s}^{-1}$ )	SFR (SED) ( $M_{\odot} \text{yr}^{-1}$ )	SFR $_{[\text{O II}]}$ ( $M_{\odot} \text{yr}^{-1}$ )	$\log(M_{\text{h}}/M_{\odot})$	$R_{\text{h}}$ (kpc)
(1)	(2)	(3)	(4)	(5)	(6)	(7)	(8)	(9)
J000413.73-082625.4	J000413.99-082624.27	10.99 <sup>+0.06</sup> <sub>-0.06</sub>	-21.68 ± 0.09	15.36 ± 0.09	10.25 <sup>+0.96</sup> <sub>-0.87</sub>	1.37 ± 0.44	12.24	228
J015635.18+034308.1	J015635.21+034306.03	10.21 <sup>+0.33</sup> <sub>-0.33</sub>	-20.06 ± 0.25	3.45 ± 0.79	7.39 <sup>+49.32</sup> <sub>-6.34</sub>	2.31 ± 0.73	11.65	145
J024008.21-081223.4	J024008.39-081222.53	10.57 <sup>+0.07</sup> <sub>-0.07</sub>	-20.68 ± 0.13	6.13 ± 0.76	5.87 <sup>+0.74</sup> <sub>-0.87</sub>	1.55 ± 0.49	11.87	174
J033438.28-071149.0	J033438.08-071152.08	10.57 <sup>+0.12</sup> <sub>-0.12</sub>	-20.81 ± 0.15	6.87 ± 0.94	4.55 <sup>+1.16</sup> <sub>-1.12</sub>	6.50 ± 1.86	11.88	169
J085627.09+074031.7	J085627.31+074029.51	11.02 <sup>+0.14</sup> <sub>-0.14</sub>	-19.05 ± 0.16	1.37 ± 0.20	17.90 <sup>+10.29</sup> <sub>-7.60</sub>	0.26 ± 0.08	12.27	237
J092222.58+040858.7	J092222.52+040856.00	10.26 <sup>+0.09</sup> <sub>-0.09</sub>	-20.06 ± 0.12	3.46 ± 0.39	2.59 <sup>+0.23</sup> <sub>-0.34</sub>	2.06 ± 0.66	11.66	154
J121453.29+080457.7	J121453.46+080457.03	10.71 <sup>+0.13</sup> <sub>-0.13</sub>	-20.28 ± 0.12	4.22 ± 0.46	4.95 <sup>+0.78</sup> <sub>-0.82</sub>	2.23 ± 0.71	11.97	192
J155003.71+031325.0	J155003.47+031325.77	11.62 <sup>+0.19</sup> <sub>-0.20</sub>	-21.21 ± 0.10	9.99 ± 0.96	33.51 <sup>+22.0</sup> <sub>-14.3</sub>	1.44 ± 0.46	13.56	624
J212143.98+003954.2	J212144.18+003954.25	10.37 <sup>+0.15</sup> <sub>-0.15</sub>	-20.33 ± 0.14	4.42 ± 0.56	7.93 <sup>+1.70</sup> <sub>-1.89</sub>	1.66 ± 0.51	11.75	157
J220330.04-002211.4	J220329.76-002215.03	10.22 <sup>+0.11</sup> <sub>-0.12</sub>	-20.39 ± 0.10	4.68 ± 0.43	3.74 <sup>+0.61</sup> <sub>-0.70</sub>	4.68 ± 1.34	11.64	153
J232653.15+002142.9	J232653.20+002148.10	11.07 <sup>+0.24</sup> <sub>-0.26</sub>	-20.68 ± 0.21	6.13 ± 0.21	20.14 <sup>+10.14</sup> <sub>-7.59</sub>	1.03 ± 0.32	12.34	245
J233548.62-023734.3	J233548.79-023734.79	10.81 <sup>+0.15</sup> <sub>-0.13</sub>	-20.58 ± 0.10	5.58 ± 0.53	6.65 <sup>+2.59</sup> <sub>-1.49</sub>	0.62 ± 0.19	12.06	204

[et al. 2020](#)). Seventy five percent of these galaxies are within  $\pm 200$   $\text{kms}^{-1}$  of the Mg II absorption. Interestingly in our sample, the only system with clearly identified non-isolated host galaxies (beyond  $D=100$  kpc) is USMgII absorber towards J2207-0901 at  $z_{\text{abs}}=0.5623$  studied by [Gauthier \(2013\)](#). If we combine this with the non-isolated host galaxies studied by [Nestor et al. \(2011a\)](#), we find the mean

velocity offset to be  $\mu = 106.4 \text{ kms}^{-1}$  and  $\sigma = 201.3 \text{ kms}^{-1}$ . This trend of larger velocity dispersion for non-isolated galaxies, though based on only 3 USMgII absorbers, is consistent with what has been found for literature samples discussed above.

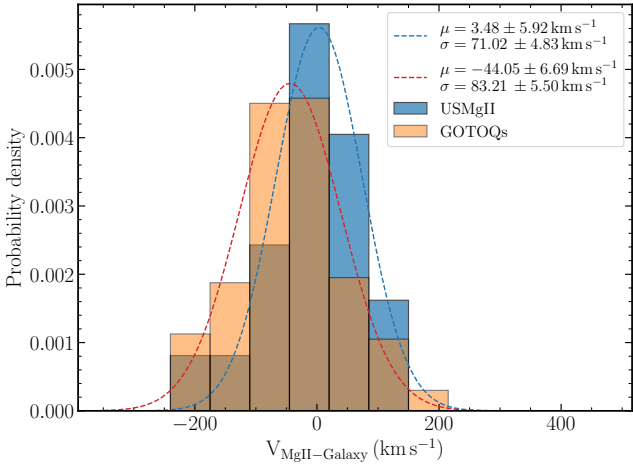


**Figure 7.** The distribution of the line of sight velocity separation between the Mg II absorption and the [O II] emission detected from the associated host galaxies. The blue and orange histograms represent the USMgII host galaxies from our sample and the GOTOQs from *Joshi et al. (2017)*, respectively. The dashed blue and orange line corresponds to the Gaussian fits to the histograms associated with the USMgII and the GOTOQs, respectively. The Gaussian parameters for these fits are also provided in the figure.

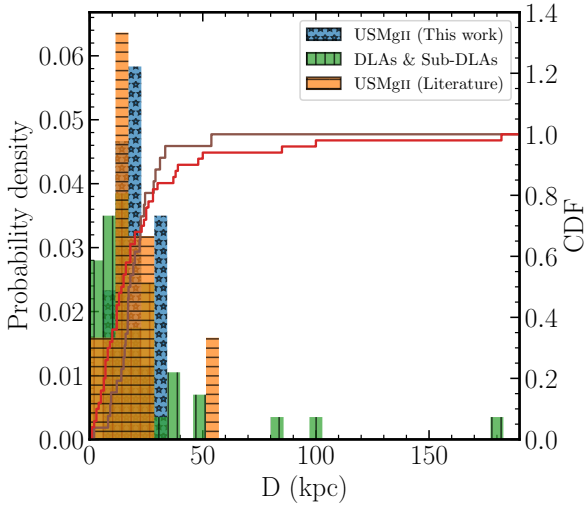


**Figure 8.** The impact parameter distribution of the USMgII host galaxies identified in our survey (blue), from the literature (orange) and the host galaxies of DLAs and sub-DLAs (green, *Rahmani et al. 2016*). The cumulative distribution of D for the USMgII absorbers (ours + literature sample) and that for the DLAs and sub-DLAs are shown in brown and red respectively.

**5.3 Impact parameter: distribution and correlations**

The measured impact parameter (D) of the USMgII host galaxies are listed in column 5 of Table 5 and its distribution is shown in Figure 8. In the case of multiple host galaxy identifications we consider the nearest one (i.e. smallest D values). Recall, in the case of USMgII system at  $z_{\text{abs}}=0.4801$  towards J2338-0056, the galaxy with the consistent redshift is at  $D = 79$  kpc, while there are two nearby galaxies for which we could not measure the redshifts. When we consider the nearest identified galaxy to the USMgII absorber (excluding the case of J2338-0056), the D values are in the range 7.3 to 38 kpc with a median D of 18 kpc. If we include two GOTOQs,

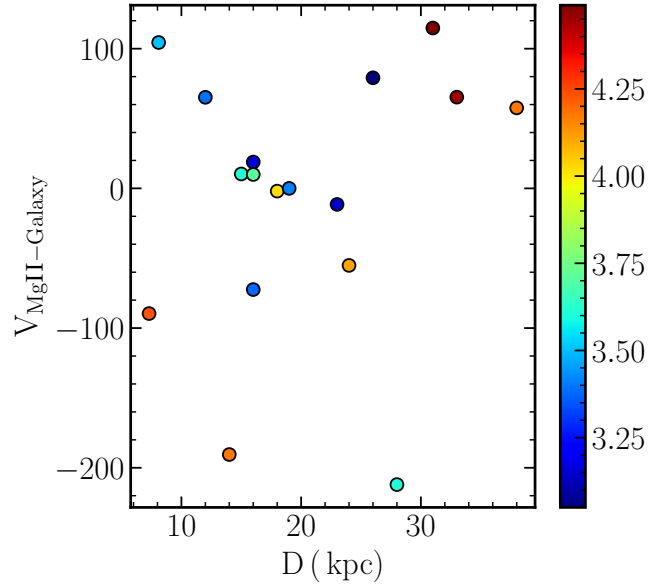


**Figure 9.** Velocity difference between the host galaxies and USMgII absorbers is plotted against the impact parameter. The points are colour-coded by  $W_{2796}$  as shown in the colour bar. No correlation is evident in this figure.

$z_{\text{abs}}=0.5561$  system towards J1025-0046 and  $z_{\text{abs}}=0.5928$  towards J0930+0018, then the median D is 16 kpc.

As mentioned before DLAs tend to have large  $W_{2796}$ , therefore it is important to compare the D-distributions of USMgII and DLAs in order to understand differences in their origin. In Figure 8 we also show the distributions of D for the USMgII host galaxies found in the literature (see Table F in the appendix), as well as the host galaxies of DLAs and the sub-DLAs (at  $0.01 \leq z_{\text{abs}} \leq 3.4$ ) given in *Rahmani et al. (2016)*. In the sample of USMgII systems from the literature, the impact parameter for the nearest galaxy ranges from 2 to 53.8 kpc with a median D of 17 kpc. The impact parameter of the DLAs and sub-DLAs ranges from 1 to 182 kpc with a median D of 14 kpc. We performed a KS test between the distributions of D for the two samples (sub-DLAs + DLA sample vs. the combined USMgII sample, i.e., ours + literature sample). We find the maximum difference between the cumulative distributions to be 0.30 and the probability of this difference to occur by chance being 0.08. This suggests that the two samples of absorbers belong to different parent populations at the  $\sim 2\sigma$  level. The difference mainly comes from few DLA host galaxies with large impact parameters.

Next we explore the correlation between  $W_{2796}$  and other parameters such as  $E(B-V)$ , different equivalent width ratios and velocity offset. We do not find any clear trend between  $E(B-V)$  and D in our sample. Spearman rank correlation analysis between the two gives a correlation coefficient of,  $r_s = -0.05$ , confirming the lack of a correlation. We also do not find any significant correlation (or anti-correlation) between D and  $W_{2853}^{\text{MgI}}/W_{2796}^{\text{MgII}}$ . We do see some trend of large  $\mathcal{R} = W_{2600}^{\text{FeII}}/W_{2796}^{\text{MgII}}$  having smaller D (when we exclude the  $z_{\text{abs}}=0.5624$  system towards J232653.15+002142 that has Mg II doublet ratio less than 1 and  $W_{2600}^{\text{FeII}} = 4.29\text{\AA}$ ). We find a Spearman correlation coefficient of  $r_s = -0.48$  between D and  $\mathcal{R}$ . It will be interesting to confirm this trend with a larger sample.

In Figure 9, we plot the velocity offset of the host galaxy with respect to the absorption redshift and the impact parameter for our USMgII sample. There is no clear correlation evident between these two quantities. The figure also suggests that there is no correlation

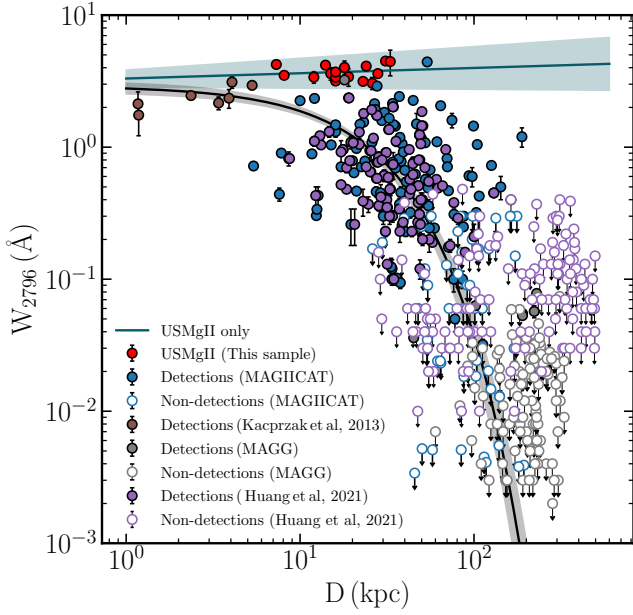


**Figure 10.** The scatter plot of  $W_{2796}$  vs  $D$ . Our USMgII systems are shown in red and literature data are shown in different symbols (as indicated in the panel). Black (cyan-green) solid curve with gray shaded region shows the best fit to the full sample (USMgII systems) and the associated error. It is evident that there is no anti-correlation between  $W_{2796}$  and  $D$  for the USMgII absorbers (also see Figures G1 and G2 in the appendix).

**Table 7.** Best fit to the relationship between  $W_{2796}$  vs  $D$

$\log(W_{2796})$	Reference
$(-0.015 \pm 0.002)D(\text{kpc}) + (0.27 \pm 0.11)$	Nielsen et al. (2013b)
$(-0.005 \pm 0.002)D(\text{kpc}) - (0.09 \pm 0.12)$	Rubin et al. (2018)
$(-1.17 \pm 0.10) \log(D(\text{h}^{-1} \text{kpc})) + (1.28 \pm 0.13)$	Chen et al. (2010a)
$(-0.72 \pm 0.25) \log(D(\text{kpc})) + (0.83 \pm 0.38)$	Huang et al. (2021)
$(-0.019 \pm 0.002)D(\text{kpc}) + (0.464 \pm 0.039)$	This work
$(-0.016 \pm 0.003)D(\text{kpc}) + (0.702 \pm 0.067)$	This work ( $0.4 \leq z \leq 0.6$ )

between  $W_{2796}$  and either  $D$  or the velocity offset. As  $W_{2796}$  is related to the line-of-sight velocity spread, lack of strong velocity offset is consistent with the velocity field in the absorbing gas being symmetric with respect to the systemic redshift of the galaxies.

#### 5.4 Impact parameter vs $W_{2796}$

It has now been well-established that  $W_{2796}$  anti-correlates with  $D$ , albeit with a large scatter (Bergeron & Boissé 1991; Steidel 1995; Chen et al. 2010a; Nielsen et al. 2013b). In Figure 10, we plot  $W_{2796}$  vs.  $D$  for our sample as well as data from the literature. It is a common practice to characterize this anti-correlation, either by a log-linear or a power law dependence. Best fit relationship obtained for different samples in the literature are summarized in Table 7. We obtained the best fit to the data plotted in Figure 10 using the standard procedure discussed in Appendix G. The best fit relationship for the full sample is also shown in Figure 10 and provided in Table 7. This table also provides results for absorbers at  $0.4 \leq z \leq 0.6$  (see Figure G1).

It is apparent that USMgII systems occupy a distinct region in the plot and do not follow the general anti-correlation between  $W_{2796}$  and  $D$  (also see Figure G2). For example, for the power law fit given by Chen et al. (2010a)  $W_{2796} \geq 3 \text{ \AA}$  is realised for  $D \leq 4.85$

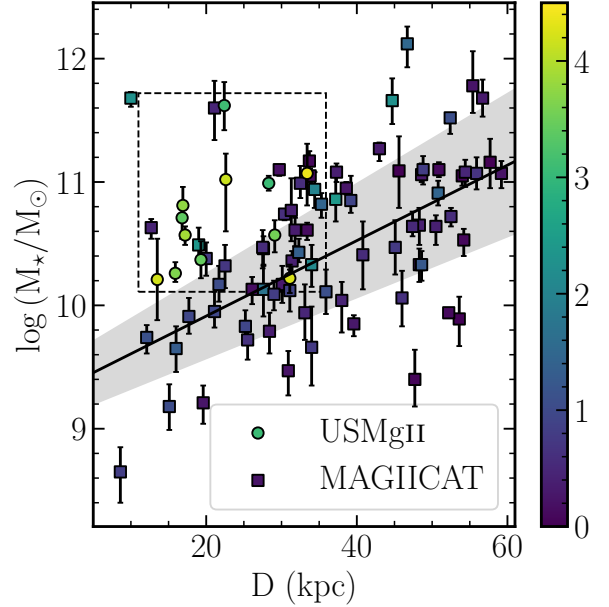


**Figure 11.** The stellar mass of the Mg II host galaxies against the impact parameter. Points are color-coded based on the Mg II rest equivalent width,  $W_{2796}$ , as shown in the sidebar. The squares and circles represent the host galaxies taken from the MAGIICAT sample and our USMgII sample, respectively. Region occupied by the USMgII systems is demarcated by the box in dashed line.

kpc. For the log-linear fit given by Nielsen et al. (2013b),  $W_{2796}$  saturates to a value of  $1.86 \text{ \AA}$  for  $D = 0$  kpc. Fit saturating to lower  $W_{2796}$  is also the case for the fit discussed in Figure 12 of Dutta et al. (2020). Even for our best fit for  $0.4 \leq z \leq 0.6$  absorbers (that also includes USMgII systems in the fit) USMgII systems are expected to have  $D \leq 14$  kpc. This is lower than the median values discussed above. Clearly the distribution of  $D$  for the USMgII is inconsistent with the predictions from the general population of Mg II absorbers.

The large scatter seen around the best fit is most likely to be driven by various galaxy properties such as  $z_{\text{abs}}$ , luminosity (Nielsen et al. 2013b; Chen et al. 2010b), stellar mass (Churchill et al. 2013), halo radius and the orientation (Bouché et al. 2012). Indeed, Huang et al. (2021) have explicitly shown that the scatter decreases when one takes the galaxy luminosity, stellar mass and halo radius into account for the star-forming isolated galaxies (see also, Chen et al. 2010a). Recent wide-field IFU surveys using MUSE like the MUDF (Fossati et al. 2019), MUSE-ALMA Halos (Hamanowicz et al. 2020), as well as grisms surveys using HST (Dutta et al. 2020; Lundgren et al. 2021) are adding further scatter to the  $W_{2796} - D$  plot, by identifying multiple galaxies associated with Mg II systems out to large impact parameters. Therefore, the environment and ambiguity in absorber-galaxy association are other factors that enhance the scatter. In what follows, we explore how the above mentioned properties of USMgII host galaxies compare with that of the host galaxies in the general population of Mg II absorbers.

In Figure. 11, we plot  $M_*$  vs  $D$  color coded using  $W_{2796}$ . When we consider the MAGIICAT galaxies, for a given  $W_{2796}$  massive galaxies tend to be at a larger impact parameter. We also find a correlation between  $M_*$  and  $D$  that can be approximated by  $\log(M/M_{\odot}) = (0.036 \pm 0.006)D(\text{kpc}) + (9.301 \pm 0.225)$ . The solid black line and the gray shaded region around it in the figure correspond to this fit and the associated  $1\sigma$  uncertainty, respectively. The dashed rectangular box in this figure encompasses the points

from the USMgII sample. It is evident that the USMgII galaxies are more massive than the MAGIICAT host galaxies for the same impact parameter (in line with the findings of Rubin et al. 2018; Dutta et al. 2020). Note only 2 out of 12 USMgII host galaxies are within  $1\sigma$  region of the fit. We also see similar trend when we use  $M_B$  instead of  $M_*$ , i.e., there is a correlation between  $M_B$  and  $D$ , and USMgII galaxies tend to be brighter compared to the relationship defined by MAGIICAT points (see Appendix H). The correlation between  $D$  and  $M_B$  and/or  $M_*$  are typically used in the literature (Chen et al. 2010a; Huang et al. 2021) to reduce the scatter in the  $D$  vs  $W_{2796}$  plots. For the median impact parameter and  $M_*$  of our host galaxies, equation 16 of Huang et al. (2021) predicts  $W_{2796} = 1.5\text{\AA}$ . Thus it appears that USMgII absorbers do not follow the general trend and the scatter in  $D$  vs  $W_{2796}$  plot can not explained by previously reported correction to the host galaxy stellar mass.

### 5.5 [O II] Luminosity and Star Formation Rate:

The measured [O II] line flux for all the host galaxies of our USMgII systems are given in column 6 of Table 5. These values are obtained after applying the corrections as explained above (see Section 3) but without applying any dust correction. Left panel in Figure 12, we plot the distribution of [O II] luminosity ( $L_{[\text{O II}]}$ ) scaled by the characteristic [O II] luminosity ( $L_{[\text{O II}]}^*$ ) of the field galaxies (Comparat et al. 2016) at the host galaxy redshift. The blue histogram with star, orange histogram with tilted vertical lines, the red histogram with the horizontal lines and the green histogram with tilted lines on the left corresponds to the distribution of the scaled  $L_{[\text{O II}]}$  of the USMgII host galaxies from our USMgII sample, GOTOQs (Joshi et al. 2017), MEGAFLOW-III survey (Schroetter et al. 2019), MAGG survey (Dutta et al. 2020) respectively. The [O II] luminosity of our galaxies ranges from 0.06 to 1.43  $L_{[\text{O II}]}^*$ , with a median value of 0.39  $L_{[\text{O II}]}^*$  with  $L_{[\text{O II}]}^*(z = 0.5) = 3.2 \times 10^{41} \text{ erg s}^{-1}$ . Note that, in the case of  $z_{\text{abs}} = 0.5896$  towards J0218-0832, the host galaxy does not show detectable [O II] emission with  $L_{[\text{O II}]} \leq 1.8 \times 10^{41} \text{ erg s}^{-1} (3\sigma)$ . In the case of galaxies identified by Gauthier (2013) for the  $z_{\text{abs}} = 0.5623$  system towards J2207-0901, the observed [O II] luminosity of the galaxy with the lowest  $D$  is  $0.56 L_{[\text{O II}]}^*$ .

Using the [O II] luminosity function (Comparat et al. 2016) we calculate the median expected  $L_{[\text{O II}]}$  and the number of galaxies having  $L_{[\text{O II}]} \geq L_{[\text{O II}]}^*$ . When we consider  $L_{\text{min}} = 0.06\%$  (or  $0.1\%$ )  $L_{[\text{O II}]}^*$  based on the lowest luminosity observed in our sample, we expect about 0.6% (or 1.5%) of galaxies in our sample will be super- $L_{[\text{O II}]}^*$ . Also expected median [O II] luminosity is less than  $0.2 L_{[\text{O II}]}^*$ . Therefore, out of 18 USMgII host galaxies in our sample, we expect about 0.2 of them to be super- $L_{[\text{O II}]}^*$  galaxies. In our sample there are two host galaxies with  $L_{[\text{O II}]}$  in excess of  $L_{[\text{O II}]}^*$  and the observed median value ( $0.39 L_{[\text{O II}]}^*$ ) is higher than that predicted ( $< 0.2 L_{[\text{O II}]}^*$ ) from the luminosity function. Therefore, we can conclude that  $L_{[\text{O II}]}$  of the USMgII host galaxies are significantly higher than what we expect from random sample of galaxies and USMgII selection preferentially picks galaxies with higher  $L_{[\text{O II}]}$ .

The SFR is assumed to be proportional to the [O II] luminosity of the galaxy and is given by Kennicutt (1998),  $\text{SFR}_{[\text{O II}]} = (1.4 \pm 0.4) \times 10^{-41} L_{[\text{O II}]} \text{ ergs s}^{-1}$ . Measured  $\text{SFR}_{[\text{O II}]}$  are also given in Table 6. As can be seen from this table, SFR based on SED fitting ranges from  $2.6 M_{\odot} \text{ yr}^{-1}$  to  $33.5 M_{\odot} \text{ yr}^{-1}$ , with a median value of  $7.7 M_{\odot} \text{ yr}^{-1}$ , whereas the  $\text{SFR}_{[\text{O II}]}$  ranges from  $0.26 M_{\odot} \text{ yr}^{-1}$  to  $6.50 M_{\odot} \text{ yr}^{-1}$ , with a median value of  $1.61 M_{\odot} \text{ yr}^{-1}$ . It is well documented that the SFR obtained based on [O II] emission line have systematic uncertainties that depend on variation in reddening, chemical abundance (stellar mass

through the mass metallicity relations) and ionization (Moustakas et al. 2006; Gilbank et al. 2010). A considerable contribution to the underestimation of  $\text{SFR}_{[\text{O II}]}$  originates from the dust corrections that we have not applied for our estimation. Also it has been found that in galaxies with  $12 + [\text{O}/\text{H}] > 8.7$  (or B-band luminosity in excess  $10^{11} L_{B\odot}$ ) one tends to underestimate the  $\text{SFR}_{[\text{O II}]}$  (Moustakas et al. 2006). Therefore, we have used SFR from the SED fitting in the analysis presented below.

### 5.6 [O II] luminosity vs $W_{2796}$

If the large  $W_{2796}$  of the USMgII absorbers is related to feedback processes in the host galaxy, then we expect a correlation between  $W_{2796}$  and  $L_{[\text{O II}]}$ . Such a correlation is also found between the  $L_{[\text{O II}]}$  and  $W_{2796}$  in the stacked SDSS spectrum (Noterdaeme et al. 2008; Ménard et al. 2011). It was suggested that if this correlation is driven by any physical mechanism then one can use  $W_{2796}$  as a proxy to pick high-luminosity star-forming galaxies. However, as pointed out by Joshi et al. (2018), the main driver for this correlation could be the impact parameter vs.  $W_{2796}$  correlation (also see López & Chen 2012). In that case, there is a high probability for emission from the galaxies hosting the high  $W_{2796}$  systems to fall inside the SDSS fiber compared to the host galaxies of the low  $W_{2796}$  systems.

In their SIMPLE sample, Bouché et al. (2007) have found a  $2\sigma$  correlation between the SFR derived from the  $H\alpha$  luminosity and  $W_{2796}$ . They explained this by assuming the absorbing gas being part of the wind from the host galaxies. As we now have larger number of  $L_{[\text{O II}]}$  measurements for host galaxies of Mg II absorbers, we revisit this correlation. In the right panel of Figure 12, we plot the scaled [O II] luminosity, i.e.,  $L_{[\text{O II}]} / L_{[\text{O II}]}^*$ , vs.  $W_{2796}$ . We do not find any trend between  $W_{2796}$  and  $L_{[\text{O II}]} / L_{[\text{O II}]}^*$  in our USMgII sample alone. In the same plot, we also show the points from the GOTOQ, MAGG and MEGAFLOW-III samples. It is evident from the figure that most of the galaxies with  $L_{[\text{O II}]} / L_{[\text{O II}]}^* \geq 1$  are associated with high  $W_{2796}$  systems (i.e. 58% and 79% of such galaxies are associated with  $W_{2796} \geq 3$  and  $2.5\text{\AA}$  absorbers respectively). Similarly, galaxies with  $L_{[\text{O II}]} / L_{[\text{O II}]}^* \leq 0.1$  are predominantly associated with low equivalent width (i.e.  $W_{2796} \leq 1\text{\AA}$ ) absorbers from Dutta et al. (2020).

Thus, when we perform the rank-correlation analysis for the combined sample, we do find a correlation (Spearman rank correlation of  $r_S = 0.34$  and a p-value of  $< 10^{-4}$ ) between the quantities plotted in Figure 12. When we restrict ourselves to stronger Mg II absorption systems, the strength of this correlation decreases significantly. For example, when we consider systems with  $W_{2796} \geq 0.5$ , the rank correlation coefficient,  $r_S$  decreases to 0.21 (p value =  $6 \times 10^{-4}$ ), and for systems with  $W_{2796} \geq 2$ ,  $r_S$  further decreases to 0.13 (p value = 0.1). When we exclude the GOTOQs, which are biased towards high  $L_{[\text{O II}]}$  galaxies,  $r_S$  drops from 0.34 to 0.23 (p-value = 0.03) for the full Mg II sample. Additionally, if we restrict ourselves to host galaxies having impact parameter less than 50 kpc (excluding GOTOQs), we find  $r_S = 0.20$  (p-value = 0.23), while considering a maximum impact parameter of 100 kpc,  $r_S = 0.19$  (p-value = 0.18).

For better visualization, we divide the sample into 4 sub-samples of Mg II absorbers based on the rest equivalent width of the Mg II absorption ( $W_{2796} \leq 1$ ,  $1 < W_{2796} \leq 2$ ,  $2 < W_{2796} \leq 3$ ,  $W_{2796} > 3$ ). For each of these sub-samples, we calculate the median values of  $W_{2796}$  and  $L_{[\text{O II}]} / L_{[\text{O II}]}^*$ . The four blue stars in the right panel of Figure 12 corresponds to the median values for each sub-sample. The analysis presented here suggests a correlation between  $W_{2796}$  and  $L_{[\text{O II}]}$  for the full sample. While USMgII selection statistically



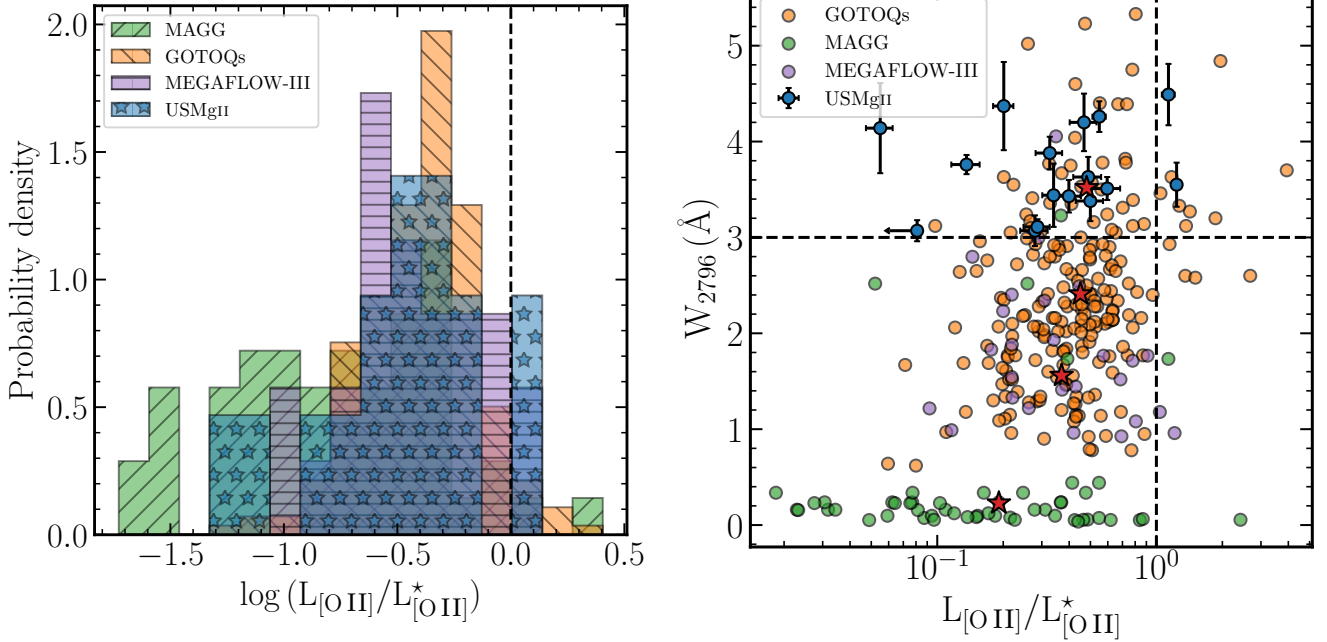


**Figure 12.** *Left panel:* Distribution of [O II] luminosity scaled by the characteristic [O II] luminosity of the field galaxies (Comparat et al. 2016) at the redshift of the galaxies. The blue histogram with stars, orange histogram tilted vertical lines, the magenta histogram with the horizontal lines and the green histogram with tilted lines on the left corresponds to the [O II] luminosity distribution of the USMgII host galaxies from our USMgII sample, of the GOTOQs (Joshi et al. 2017), galaxies from the MEGAFLow-III survey (Schroetter et al. 2019), MAGG survey (Dutta et al. 2020) respectively. *Right panel:*  $W_{2796}$  against the scaled [O II] luminosity. Color assignment is same as that of the left panel. The red stars correspond to the median values of the  $W_{2796}$  and  $L_{\text{[O II]}}/L_{\text{[O II]}}^*$  in 4 sub-sample based on  $W_{2796}$  (see text for details). The horizontal dashed black line corresponds to  $W_{2796} = 3$ , i.e., limiting value for the USMgII systems. The vertical dashed line in both the panels corresponds to the characteristic [O II] luminosity,  $L_{\text{[O II]}}^*$ .

picks high luminosity host galaxies, the scatter in  $L_{\text{[O II]}}$  is large at a given  $W_{2796}$ .

### 5.7 Nebular Emission Line Ratios: metallicity and ionization parameter

The  $[\text{O III}]/[\text{O II}]$  as well as the  $[\text{O III}]/\text{H}\beta$  line ratios are very sensitive to the hardness of the ionizing radiation field (i.e. temperature of the stars), and can distinguish between the ionization mechanisms of the nebular gas in a galaxy (Baldwin et al. 1981; Kewley et al. 2001). Over the redshift range  $z = 0 - 5$ , a rise in both the ratios,  $[\text{O III}]/[\text{O II}]$  and  $[\text{O III}]/\text{H}\beta$ , of star-forming galaxies has been observed (Nakajima & Ouchi 2014; Steidel et al. 2014; Kewley et al. 2015; Khostovan et al. 2016). This implies that compared to the local galaxies, galaxies at higher redshifts have higher ionization parameter, lower metallicity, harder stellar ionizing radiation field, and higher electron densities.

Left panel of Figure 13 shows the line luminosity ratio  $L_{\text{[O III]}}/L_{\text{[O II]}}$  vs. redshift. Host galaxies of our USMgII absorption systems and GOTOQs (at  $0.4 \leq z_{\text{abs}} \leq 0.6$ ) are plotted as blue and orange points, respectively. There are 13 USMgII systems for which these measurements are possible. In cases where the [O III] emission is not clearly detected, we give  $3\sigma$  upper limits. The red line corresponds to the evolution of the line ratio  $L_{\text{[O III]}}/L_{\text{[O II]}}$  for the star-forming galaxies (Khostovan et al. 2016). It is evident from this figure that measurements from GOTOQs follow the general trend of the field galaxies. However, the measured ratio in the host galaxies of USMgII systems are typically lower than the best fit to the star-forming galaxies. The KS-test (with  $D = 0.542$  with  $p$ -value = 0.013) also confirms the distribution of  $L_{\text{[O III]}}/L_{\text{[O II]}}$  in

these two populations are different. There are 7 GOTOQs that have  $W_{2796} > 3\text{\AA}$  and the measured  $L_{\text{[O III]}}/L_{\text{[O II]}}$  are distributed equally around the fit for star-forming galaxies. We see a negative trend between  $L_{\text{[O III]}}/L_{\text{[O II]}}$  and  $W_{2796}$  in the GOTOQ sample (i.e. largest ratios are seen among the host galaxies of absorbers with low  $W_{2796}$ ). However, this anti-correlation is not statistically significant (see Figure E1 in appendix E). Thus the difference between GOTOQs and USMgII can not be simply attributed to the presence of such a trend.

In the right panel of Figure 13, we show the redshift evolution of the ratio  $L_{\text{[O III]}}/\text{H}\beta$  of the USMgII host galaxies compared to that of the GOTOQs over the same redshift range. Simultaneous measurements of  $L_{\text{[O III]}}/\text{H}\beta$  are possible for only 9 galaxies in our sample. Like for  $L_{\text{[O III]}}/L_{\text{[O II]}}$ , the  $L_{\text{[O III]}}/\text{H}\beta$  measured in the case of USMgII tend to be lower compared to the measurements from the GOTOQs and general population of galaxies. The KS-test gives  $D = 0.487$  and a  $p$ -value of 0.050. This could indicate that the ionizing radiation in the star-forming field galaxies is harder than that in the USMgII host galaxies. To explore this further, in what follows, we use the line ratios to measure the metallicity and ionization parameter of the gas.

Gas phase metallicity is usually calculated from the metallicity-sensitive line luminosity ratios of strong emission lines present in the galaxy spectrum (see e.g., Nagao et al. 2006, for various such calibrations against different line ratios). Since we have the coverage of different nebular emission lines like [O II]  $\lambda\lambda$  3727, 3729,  $\text{H}\beta$   $\lambda$  4862, and [O III]  $\lambda\lambda$  4960, 5008, we make use of the  $R_{23}$  metallicity estimator, originally proposed by Pagel et al. (1979) and defined as,  $R_{23} = (L_{\text{[O II]}\lambda\lambda 3727, 3729} + L_{\text{[O III]}\lambda\lambda 4960, 5008})/L_{\text{H}\beta}$ . Based on various photoionization models, this ratio has been calibrated against oxygen abundances (see e.g., McGaugh 1991; Kewley & Dopita 2002). How-

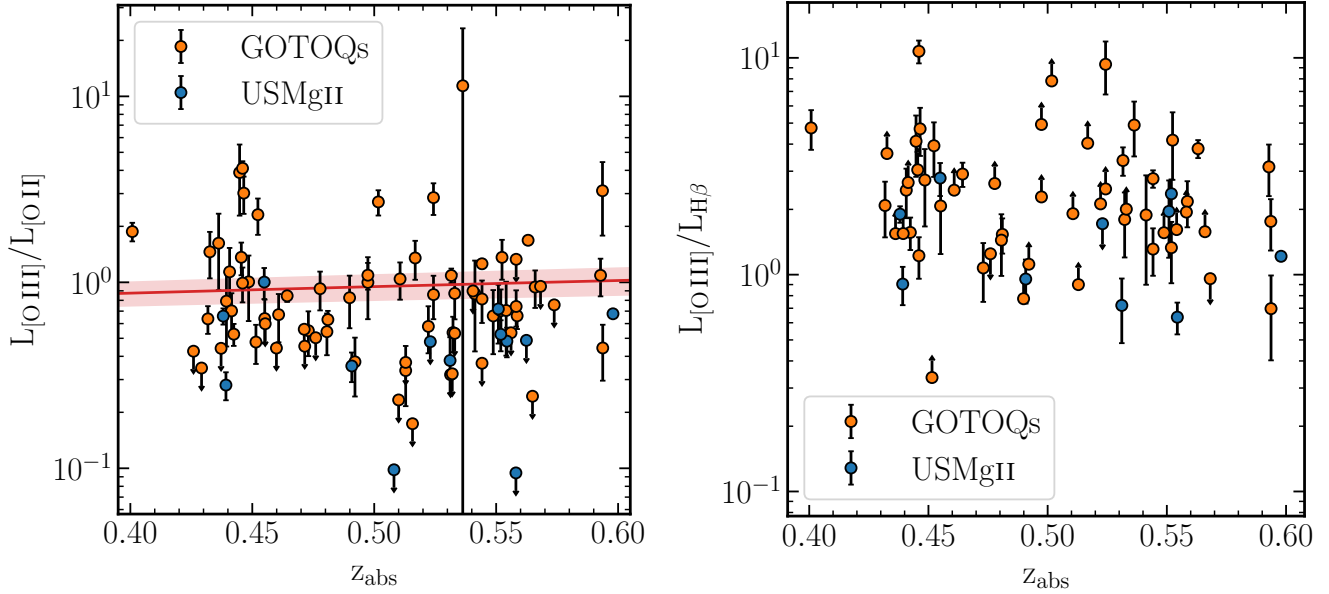


**Figure 13.** *Left panel:* Ratio of [O III] and [O II] line luminosities associated with Mg II host galaxies as a function the absorption redshift. Blue points correspond to our USMgII sample while the orange points are taken from GOTOQs (with  $0.4 \leq z_{\text{abs}} \leq 0.6$ ) (Joshi et al. 2017). The red line gives the observed redshift evolution of  $L_{[\text{O III}]} / L_{[\text{O II}]}$ , for the star-forming galaxies (Khostovan et al. 2016). *Right panel:* Ratio of [O III] and H $\beta$  line luminosities as a function of  $z_{\text{abs}}$ .

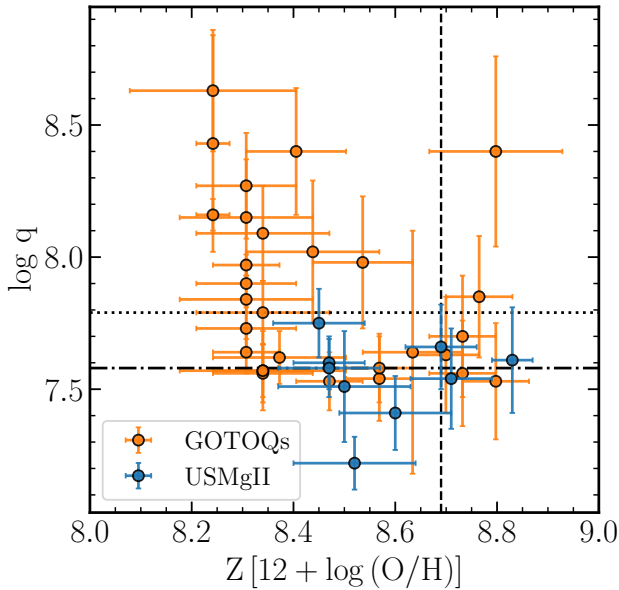


**Figure 14.** Ionization parameter ( $q$ ) vs. the gas phase metallicity ( $Z$ ) for the GOTOQs (orange) and the USMgII (blue) host galaxies in the redshift range  $0.4 \leq z \leq 0.6$ . The black dotted and dash-dotted horizontal lines corresponds median ionization parameter for the GOTOQs and the USMgII host galaxies respectively. The host galaxies of USMgII preferentially occupy low  $q$  region. The dashed vertical line corresponds to the solar oxygen abundance.

ever, the estimator  $R_{23}$  is known to have a strong dependence on the ionisation parameter ( $q$ ), i.e., the inferred metallicity will be different for different assumed values of  $q$ . Therefore, we measure the gas phase metallicity ( $Z$ ) and the ionization parameter ( $q$ ) simultaneously based on the emission lines ([O II], [O III] and H $\beta$ ) present in the galaxy spectra and the photoionization model provided by Levesque

et al. (2010) using the python fork (Mingozzi et al. 2020) of the IDL code `iz1` (Inferring metallicity and ionization parameters, Blanc et al. 2015). Apart from two cases, we do not detect the [O III]  $\lambda$  4960 emission at  $\geq 3\sigma$  significance. We therefore take the associated flux of this line to be one-third of the flux associated with [O III]  $\lambda$  5008 line as suggested by theoretical studies (Storey & Zeippen 2000).

Another difficulty in the use of  $R_{23}$  is that the ratio is doubly degenerate in terms of the oxygen abundance. This is because, at low abundance the intensity of the forbidden lines scales roughly with the chemical abundance, while at high abundance the nebular cooling is dominated by infrared fine-structure lines, and the electron temperature drops too low to collisionally excite the optical forbidden lines. Nebular emission lines like [N II]  $\lambda$  6564 are usually used to break this degeneracy (Kewley & Dopita 2002; Pettini & Pagel 2004). However, in our case, we do not have spectral coverage of the [N II]  $\lambda$  6564 line. As a result, to avoid any confusion, we will be considering only the upper branch metallicities. We detect all the three nebular lines only in the case of 10 host galaxies. The obtained gas phase metallicities,  $12 + \log(\text{O}/\text{H})$ , to be in the range from 8.45 to 8.83 (0.58-1.41 times the solar abundance for  $\log(\text{O}/\text{H})_{\odot} = 8.69$ ). Given the mass-metallicity relation (Ma et al. 2016), this corresponds to a stellar mass in the range  $9.23 \leq \log M_{\star} [M_{\odot}] \leq 10.42$ .

We performed the same exercise for the GOTOQs in the redshift range of our interest. In this redshift range, for only 29 GOTOQs, all the three emission lines are detected with at least  $3\sigma$  significance. In Figure 14, we show the scatter plot of the ionization parameter versus the gas phase metallicity for both these 29 GOTOQs as well as the USMgII host galaxies from our sample. From this plot, it is quite apparent that the USMgII galaxies tend to have a lower ionization parameter compared to the GOTOQs (KS-test gives  $D = 0.52$  and a  $p$ -value of 0.03). This indicates that, compared to the GOTOQs, the USMgII host galaxies are dominated by softer ionizing field.

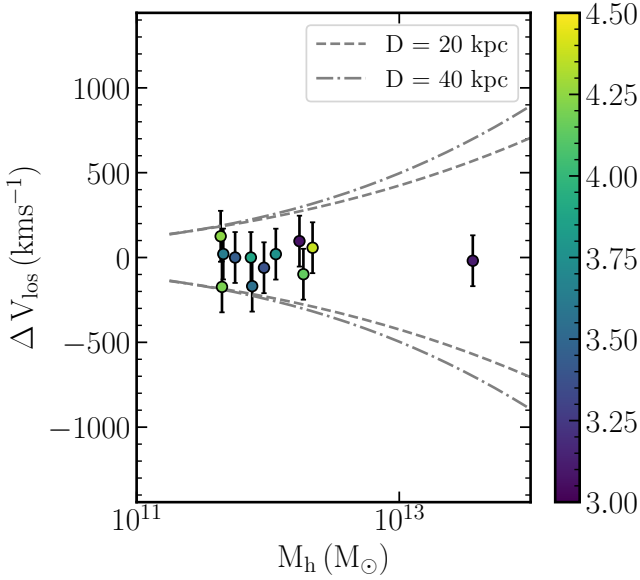


**Figure 15.** The velocity difference between the Mg II absorbing gas along the quasar sightline and the USMgII host galaxies is plotted against their dark matter halo mass color-coded following  $W_{2796}$  as indicated on the right side of the figure. The gray dashed and dot-dashed lines correspond to the escape velocity for the dark matter halo potential at the impact parameters of 20 kpc and 40 kpc respectively. For each measured velocity difference, we associate an error bar of  $\pm 150 \text{ km s}^{-1}$ .

## 6 DISCUSSION

### 6.1 Gas kinematics

From the virial radius of the USMgII host galaxies in our sample given in column 10 of Table 6, it is evident that the impact parameter is typically one-tenth of the virial radius. This (together with lack of additional galaxies within 100 kpc in most cases, see Table 2) provides a strong reason to believe that the kinematics of the absorbing gas is mostly governed by the physical processes operating in the halo of the identified host galaxy itself.

In Figure 15, we plot the rest frame velocity difference between the absorbing gas and the host galaxy along our line of sight ( $\Delta v_{\text{los}}$ ) against the halo mass color-coded as the  $W_{2796}$ . Here, we assume the dark matter halo follows the NFW profile (Navarro et al. 1997) and halo concentration of  $c_h = 10$ . The dashed and the dot-dashed gray lines corresponds to the escape velocity against the halo mass at a distance of 20 kpc and 40 kpc respectively from the center of the halo. This figure suggests the measured velocity offsets are consistent with the absorbing gas being bound to the galaxy.

However, in order to quantify what fraction of the absorbing gas is bound to the galaxy we also need to know the line of sight velocity spread. Recall that a large  $W_{2796}$  of USMgII absorption will correspond to large velocity spread,  $\Delta v_{\text{los}}$ , along our line of sight (see Ellison 2006; Zou et al. 2018). It is well known that  $W_{2796}$  is strongly correlated with  $\Delta v_{\text{los}}$ . This correlation will imply  $\Delta v_{\text{los}} > 300 \text{ km s}^{-1}$  for our sample. It is also suggested that velocity widths in excess of  $300 \text{ km s}^{-1}$  may originate from multiple components (see for example, Ledoux et al. 1998; Zou et al. 2018). As mentioned before, in three systems in our sample we see multiple component structure even at SDSS resolution. Also in three cases we see more than one galaxy at the same redshift as the USMgII absorber. The errorbars in Figure 15 indicate a spread of  $\pm 150 \text{ km s}^{-1}$  around the measured velocity offset. If velocity spreads are of this order then in

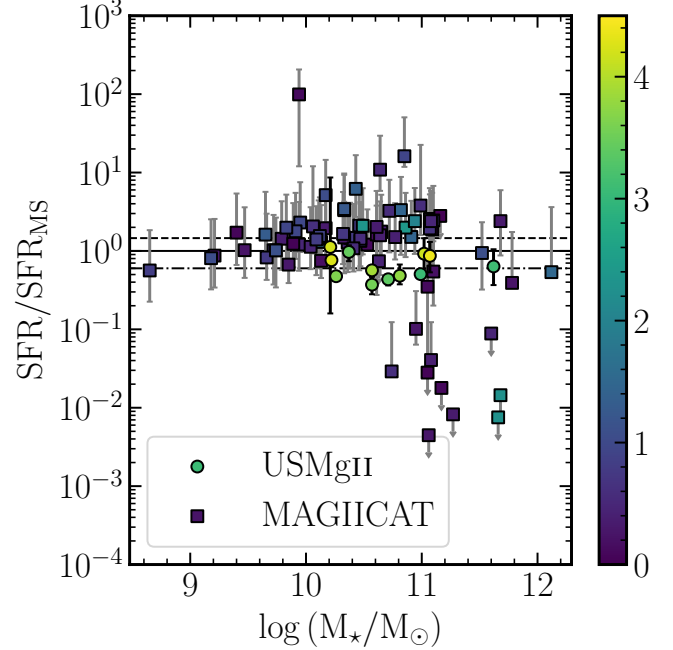


**Figure 16.** Scatter plot of SFR scaled by the SFR of a main sequence galaxy of the same stellar mass at  $z_{\text{abs}}$  ( $\text{SFR}_{\text{MS}}$ ) vs stellar mass for USMgII (circle) and MAGIICAT host galaxies (squares). Color-coding is based on the rest equivalent width,  $W_{2796}$ . The black solid line corresponds to SFR of the main sequence. The dashed black line corresponds to the median SFR of the MAGIICAT galaxies while the the dot-dashed line corresponds to that of the USMgII host galaxies.

most cases the absorbing gas will be bound to the galaxy. However, high resolution spectroscopic observations are needed to directly measure the fraction of absorbing gas bound to the galaxies.

### 6.2 Are USMgII host galaxies starbursts?

To investigate whether the USMgII host galaxies identified in our sample are regular star-forming galaxies, or star-burst or post star-burst galaxies, we put these galaxies in the SFR scaled by the main sequence SFR at the redshift of the galaxy (Speagle et al. 2014) versus stellar mass plot as shown in Figure 16. In the same plot, we have also shown the isolated Mg II absorbers within the impact parameter of 60 kpc from the MAGIICAT sample. We identify that the USMgII host galaxies have systematically less SFR (i.e. median  $\text{SFR} = 0.6 \text{ SFR}_{\text{MS}}$ ) compared to the star-forming main sequence (Speagle et al. 2014) as well as the MAGIICAT host galaxies (median  $\text{SFR} = 1.5 \text{ SFR}_{\text{MS}}$ ). Thus USMgII systems considered here are not star bursting galaxies and typically form stars at a rate slightly lower than the star forming main sequence.

Next, we test whether the SFR in the USMgII host galaxies is sufficient to launch galactic winds for the inferred gravitation potential. Given the stellar mass of  $M_*$ , the theoretical threshold SFR for launching winds is given by Murray et al. (2011),

$$\text{SFR}_{\text{threshold}} = 1.7 \left( \frac{M_*}{10^{10} M_\odot} \right)^{0.56} M_\odot \text{ yr}^{-1}.$$

For the 12 USMgII host galaxies for which the  $M_*$  and SFRs are inferred through the SED fitting, we find that the SFRs are higher than the corresponding threshold values. However, Rubin et al. (2014) does found several galaxies with SFR above this

threshold that do not show any wind signatures. The definite way of identifying the presence of galactic winds in a galaxy is to confirm whether there is a blue-shifted component present in the stellar absorption profiles. However, detecting galactic winds through such analysis is not possible with our galaxy spectra that does not cover Mg II wavelength range. Detecting wind signatures with future observations is important to quantify the role played by winds from ongoing as well as past starburst activities in producing USMgII absorption.

### 6.3 Fraction of galaxies producing USMgII absorption

From Figure 10, we see that USMgII host galaxies can have impact parameters up to 40 kpc. However, only a fraction of galaxies within  $D \sim 40$  kpc will produce an USMgII absorption. To find this fraction ( $f_{\text{USMgII}}$ ), we consider the isolated galaxies in galaxy-centric Mg II absorption surveys conducted by Dutta et al. (2020), Huang et al. (2021) and also the MAGIICAT. We find only one out of 34 galaxies (i.e.  $f_{\text{USMgII}} \sim 0.03$ ) at  $D \leq 20$  kpc and none of the 106 galaxies at  $20 \leq D(\text{kpc}) \leq 40$  produce USMgII absorption. For the full range,  $D \leq 40$ , we get an average  $f_{\text{USMgII}} \sim 0.007$ . Usually,  $f_{\text{USMgII}}$  values are interpreted in terms of covering factor of the gas. In this picture, the projected area around galaxy centres covered by the USMgII absorber is  $\sim 1\%$  of the total area. The large  $W_{2796}$  seen in the USMgII absorbers suggest large velocity spread among multiple clouds along our line of sight. Another possible interpretation of low  $f_{\text{USMgII}}$  is to say USMgII originate from a different population of galaxies. The impact parameter distribution of USMgII host galaxies not following the general population (see section 5.4) may suggest that USMgII selection picks a different population (high  $M_{\star}$  with relatively low SFR/SFR<sub>MS</sub> and low ionization parameter with large reservoir of CGM gas) of host galaxies.

### 6.4 Galaxy environments of USMgII absorbers

From the recent studies (Fossati et al. 2019; Dutta et al. 2020; Hamałowicz et al. 2020) of Mg II absorption systems with integral field units (IFU) like MUSE, there is growing evidence that a significant fraction of Mg II absorbing gas might not be associated with isolated galaxies. As mentioned before, there is one USMgII system present in the sample of Dutta et al. (2020) and three in the sample of Schroetter et al. (2019). Interestingly, for all these 4 systems the host galaxies are found to be isolated (i.e., no other galaxy is found within 100 kpc from the quasar sightline and a maximum velocity separation of  $500 \text{ km s}^{-1}$ ). As discussed in Section 3.1, there are 7 USMgII absorbers with only one potential host galaxy (with  $m_r < 23.6$  mag) within an impact parameter of 100 kpc. Therefore, at least 33% of USMgII absorbers in our sample are hosted by isolated galaxies. This fraction is 57% if we consider the limiting magnitude of  $m_r = 22.5$  mag. We identify three cases (i.e.  $\sim 14\%$ ) that are likely to be associated with more than one galaxy. These systems are towards J0156+0343, J2207-0901 and, J2338-0056. For the first case (J0156+0343), we detect extended [O II] emission consistent with the host galaxy(ies) being part of merging systems (see Figure 4). The second case (J2207-0901) has already been studied by Gauthier (2013) and the USMgII absorption is likely to be originating from intra-group gas. For the third system (J2338-0056), we identify a USMgII host galaxy at an impact parameter of 79 kpc, however there are two more galaxies (with consistent photometric redshift) present for which we could not get the spectrum and these are likely to be part of a galaxy group.

## 7 CONCLUSIONS

In this paper, we have explored the nature of the galaxies hosting USMgII absorption at redshift,  $z \sim 0.5$ . Main summary of this work is provided below.

1. Using the SDSS Mg II/Fe II absorber catalog (Zhu & Ménard 2013), we have created a sample of 109 USMgII absorbers accessible to SALT in the redshift range  $0.4 \leq z_{\text{abs}} \leq 0.6$ . From this sample, we confirm only 27 absorbers to be USMgII systems. Out of these 27 systems, 21 of them were observed with SALT and for 18 of them, the USMgII host galaxies are identified. Among the rest of the 5 unobserved systems, two of them are GOTOQs, i.e., emission is detected in the background quasar spectra. Therefore, among the 27 USMgII systems, we have identified the host galaxies for 20 of them.

2. Given the power-law fit (Chen et al. 2010a) between the impact parameter ( $D$ ) and the rest equivalent width ( $W_{2796}$ ), one expects the USMgII absorbers to reside within  $D \sim 5$  kpc. However, for our sample, the impact parameters ranges from 7.3 to 79 kpc with a median of 18 kpc. Using the log-linear fit to the combined sample (Nielsen et al. 2013a), we argue that the USMgII absorbers constitute statistically distinct population in the  $W_{2796} - D$  plane.

3. Among the the 23 USMgII systems (20 detections and 3 non-detections), we have detected [O II] emission in 18 cases. We conclude that, including the two unobserved GOTOQs, at least about 70% of the host galaxies are star-forming (i.e.  $\text{SFR} \geq 1 M_{\odot} \text{ yr}^{-1}$ ). The measured [O II] luminosities are in the range of  $0.06 L_{[\text{OII}]}^*$  to  $1.43 L_{[\text{OII}]}^*$  with a median value of  $0.39 L_{[\text{OII}]}^*$ .

4. When we combined our sample with those from the literature, we find a positive correlation between  $W_{2796}$  and  $L_{[\text{OII}]}$  ( $r_S = 0.34$  and  $p$ -value of  $< 10^{-4}$ ) for USMgII host galaxies as well as from the literature (see Figure 12). However, this correlation is seen to be driven by weak Mg II absorbers (i.e.  $W_{2796} < 1 \text{ \AA}$ ) which tend to be associated with low luminosity galaxies with higher  $D$ .

5. Compared to the field galaxies and the GOTOQs, we find the measured emission lines ratios [O III] / [O II] and [O III] /  $H\beta$  to be smaller for the USMgII host galaxies. Using photoionization models we find this trend to be driven by the ionizing radiation in these USMgII host galaxies being softer compared to the field galaxies.

6. We measure galaxy parameters like, stellar mass ( $10.21 \leq \log [M_{\star}/M_{\odot}] \leq 11.62$ ), B-band magnitude ( $-21.68 \leq M_B \leq -19.05$ ), star formation rate ( $2.59 \leq \text{SFR}[M_{\odot} \text{ yr}^{-1}] \leq 33.51$ ) and halo mass ( $11.64 \leq \log [M_h/M_{\odot}] \leq 13.56$ ) using SED fitting. The inferred virial radius of halos ( $145 \leq R_h[\text{kpc}] \leq 624$ ) are at least 5 times larger than the impact parameter measured. The measured  $M_{\star}$  for USMgII are higher than those found for general Mg II absorbers at a given impact parameter. However the measured SFR are slightly lower than what has been predicted by star forming main sequence.

7. The general population of Mg II absorbers show a correlation between  $D$  and  $M_{\star}$ . We find the USMgII systems to not follow this trend. For the same impact parameter, the USMgII host galaxies are more massive and luminous compared to the host galaxies of relatively weak Mg II absorbers.

8. We find the mean velocity difference between the Mg II absorption redshift and galaxy redshift from [O II] emission to  $\mu = 3.48 \pm 5.82 \text{ km s}^{-1}$  with a  $\sigma = 71.02 \pm 4.83 \text{ km s}^{-1}$ . This velocity difference is well within the expected escape velocities for the inferred range of  $M_h$ . However, we argue that  $W_{2796}$  measured along the line of sight should correspond to a velocity width in excess of  $300 \text{ km s}^{-1}$ . Therefore, what fraction of the observed gas in USMgII systems is bound can be answered only using high resolution spectra. Additionally, large velocity widths could indicate multiple

components (i.e. merging systems) contributing to the absorption. This can also be probed using high resolution spectroscopy.

9. In the literature sample of USMgII systems we find all the 4 known host galaxies are isolated (no companion galaxy within 100 kpc and  $\pm 500 \text{ km s}^{-1}$ ). In our sample we find that at least 33% of host galaxies of USMgII are isolated up to a projected distance of 100 kpc and the r band limiting magnitude of 23.6. Measuring the galaxy orientations using high spatial resolution imaging of the isolated galaxies together with a high-SNR spectrum probing the down the barrel absorption will be very useful to quantify the role of strong outflows in the case of USMgII systems.

## ACKNOWLEDGMENTS

All the new observations reported in this paper were obtained with the Southern African Large Telescope (SALT). RD gratefully acknowledges support from the European Research Council (ERC) under the European Union's Horizon 2020 research and innovation programme (grant agreement No 757535). This project makes use of the following softwares : NumPy (Harris et al. 2020), SciPy (Virtanen et al. 2020), Matplotlib (Hunter 2007), and AstroPy (Astropy Collaboration et al. 2013, 2018). LKG thanks Aromal P for helpful discussions on data reductions and data analysis. We thank the anonymous referee for the comments and suggestions that significantly improved the presentations of this paper.

This paper makes use of SDSS observational data. Funding for the Sloan Digital Sky Survey IV has been provided by the Alfred P. Sloan Foundation, the U.S. Department of Energy Office of Science, and the Participating Institutions. SDSS-IV acknowledges support and resources from the Center for High Performance Computing at the University of Utah. The SDSS website is [www.sdss.org](http://www.sdss.org). SDSS-IV is managed by the Astrophysical Research Consortium for the Participating Institutions of the SDSS Collaboration including the Brazilian Participation Group, the Carnegie Institution for Science, Carnegie Mellon University, Center for Astrophysics | Harvard & Smithsonian, the Chilean Participation Group, the French Participation Group, Instituto de Astrofísica de Canarias, The Johns Hopkins University, Kavli Institute for the Physics and Mathematics of the Universe (IPMU) / University of Tokyo, the Korean Participation Group, Lawrence Berkeley National Laboratory, Leibniz Institut für Astrophysik Potsdam (AIP), Max-Planck-Institut für Astronomie (MPIA Heidelberg), Max-Planck-Institut für Astrophysik (MPA Garching), Max-Planck-Institut für Extraterrestrische Physik (MPE), National Astronomical Observatories of China, New Mexico State University, New York University, University of Notre Dame, Observatório Nacional / MCTI, The Ohio State University, Pennsylvania State University, Shanghai Astronomical Observatory, United Kingdom Participation Group, Universidad Nacional Autónoma de México, University of Arizona, University of Colorado Boulder, University of Oxford, University of Portsmouth, University of Utah, University of Virginia, University of Washington, University of Wisconsin, Vanderbilt University, and Yale University.

## DATA AVAILABILITY

Data used in this work are obtained using SALT. Raw data will become available for public use 1.5 years after the observing date at <https://ssda.sao.ac.za/>.

## REFERENCES

- Anglés-Alcázar D., Faucher-Giguère C.-A., Kereš D., Hopkins P. F., Quataert E., Murray N., 2017, *Monthly Notices of the Royal Astronomical Society*, 470, 4698
- Astropy Collaboration et al., 2013, *A&A*, 558, A33
- Astropy Collaboration et al., 2018, *AJ*, 156, 123
- Baldwin J. A., Phillips M. M., Terlevich R., 1981, *PASP*, 93, 5
- Barbary K., 2016, *The Journal of Open Source Software*, 1, 58
- Bergeron J., Boissé P., 1991, *A&A*, 243, 344
- Bertin E., Arnouts S., 1996, *A&AS*, 117, 393
- Blanc G. A., Kewley L., Vogt F. P. A., Dopita M. A., 2015, *ApJ*, 798, 99
- Bordoloi R., et al., 2011, *The Astrophysical Journal*, 743, 10
- Bordoloi R., Lilly S. J., Kacprzak G. G., Churchill C. W., 2014, *The Astrophysical Journal*, 784, 108
- Bouché N., Murphy M. T., Péroux C., Csabai I., Wild V., 2006, *MNRAS*, 371, 495
- Bouché N., Murphy M. T., Péroux C., Davies R., Eisenhauer F., Förster Schreiber N. M., Tacconi L., 2007, *ApJ*, 669, L5
- Bouché N., Hohensee W., Vargas R., Kacprzak G. G., Martin C. L., Cooke J., Churchill C. W., 2012, *MNRAS*, 426, 801
- Bruzual G., Charlot S., 2003, *Monthly Notices of the Royal Astronomical Society*, 344, 1000
- Buchner J., 2021, *The Journal of Open Source Software*, 6, 3001
- Buckley D. A. H., Charles P. A., Nordsieck K. H., O'Donoghue D., 2005, *Proceedings of the International Astronomical Union*, 1, 1–12
- Budzynski J. M., Hewett P. C., 2011, *MNRAS*, 416, 1871
- Burgh E. B., Nordsieck K. H., Kobulnicky H. A., Williams T. B., O'Donoghue D., Smith M. P., Percival J. W., 2003, in Iye M., Moorwood A. F. M., eds, *Society of Photo-Optical Instrumentation Engineers (SPIE) Conference Series Vol. 4841, Instrument Design and Performance for Optical/Infrared Ground-based Telescopes*. pp 1463–1471, [doi:10.1117/12.460312](https://doi.org/10.1117/12.460312)
- Carnall A. C., McLure R. J., Dunlop J. S., Davé R., 2018, *Monthly Notices of the Royal Astronomical Society*, 480, 4379
- Carnall A. C., Leja J., Johnson B. D., McLure R. J., Dunlop J. S., Conroy C., 2019, *ApJ*, 873, 44
- Chen H.-W., Helsby J. E., Gauthier J.-R., Shectman S. A., Thompson I. B., Tinker J. L., 2010a, *The Astrophysical Journal*, 714, 1521
- Chen H.-W., Wild V., Tinker J. L., Gauthier J.-R., Helsby J. E., Shectman S. A., Thompson I. B., 2010b, *ApJ*, 724, L176
- Chevallard J., Charlot S., 2016, *Monthly Notices of the Royal Astronomical Society*, 462, 1415
- Churchill C. W., Nielsen N. M., Kacprzak G. G., Trujillo-Gomez S., 2013, *ApJ*, 763, L42
- Comparat J., et al., 2016, *MNRAS*, 461, 1076
- Crawford S. M., et al., 2010, in *Observatory Operations: Strategies, Processes, and Systems III*. p. 773725, [doi:10.1117/12.857000](https://doi.org/10.1117/12.857000)
- Dey A., et al., 2019, *AJ*, 157, 168
- Dutta R., et al., 2020, *MNRAS*, 499, 5022
- Ellison S. L., 2006, *MNRAS*, 368, 335
- Faber S. M., et al., 2007, *ApJ*, 665, 265
- Falcón-Barroso J., Sánchez-Blázquez P., Vazdekis A., Ricciardelli E., Cardiel N., Cenarro A. J., Gorgas J., Peletier R. F., 2011, *A&A*, 532, A95
- Fossati M., et al., 2019, *MNRAS*, 490, 1451
- Fukugita M., Shimasaku K., Ichikawa T., 1995, *PASP*, 107, 945
- Fynbo J. P. U., et al., 2010, *MNRAS*, 408, 2128
- Gauthier J.-R., 2013, *Monthly Notices of the Royal Astronomical Society*, 432, 1444
- Gilbank D. G., Baldry I. K., Balogh M. L., Glazebrook K., Bower R. G., 2010, *MNRAS*, 405, 2594
- Girelli G., Pozzetti L., Bolzonella M., Giocoli C., Marulli F., Baldi M., 2020, *A&A*, 634, A135
- Gordon K. D., Clayton G. C., Misselt K. A., Landolt A. U., Wolff M. J., 2003, *The Astrophysical Journal*, 594, 279
- Guillemin P., Bergeron J., 1997, *A&A*, 328, 499
- Hamanowicz A., et al., 2020, *MNRAS*, 492, 2347
- Harris C. R., et al., 2020, *Nature*, 585, 357–362
- Huang Y.-H., Chen H.-W., Shectman S. A., Johnson S. D., Zahedy F. S.,

- Helsby J. E., Gauthier J.-R., Thompson I. B., 2021, *MNRAS*, **502**, 4743
- Hunter J. D., 2007, *Computing in Science Engineering*, **9**, 90
- Joshi R., Srianand R., Petitjean P., Noterdaeme P., 2017, *Monthly Notices of the Royal Astronomical Society*, **471**, 1910
- Joshi R., Srianand R., Petitjean P., Noterdaeme P., 2018, *MNRAS*, **476**, 210
- Kacprzak G. G., et al., 2014, *The Astrophysical Journal*, **792**, L12
- Kennicutt Robert C. J., 1998, *ApJ*, **498**, 541
- Kewley L. J., Dopita M. A., 2002, *ApJS*, **142**, 35
- Kewley L. J., Dopita M. A., Sutherland R. S., Heisler C. A., Trevena J., 2001, *ApJ*, **556**, 121
- Kewley L. J., Zahid H. J., Geller M. J., Dopita M. A., Hwang H. S., Fabricant D., 2015, *ApJ*, **812**, L20
- Khostovan A. A., Sobral D., Mobasher B., Smail I., Darvish B., Nayyeri H., Hemmati S., Stott J. P., 2016, *MNRAS*, **463**, 2363
- Kobulnicky H. A., Nordsieck K. H., Burgh E. B., Smith M. P., Percival J. W., Williams T. B., O'Donoghue D., 2003, in Iye M., Moorwood A. F. M., eds, Society of Photo-Optical Instrumentation Engineers (SPIE) Conference Series Vol. 4841, Instrument Design and Performance for Optical/Infrared Ground-based Telescopes. pp 1634–1644, doi:10.1117/12.460315
- Kocevski D. D., Lemaux B. C., Lubin L. M., Shapley A. E., Gal R. R., Squires G. K., 2011, *ApJ*, **737**, L38
- Kroupa P., Boily C. M., 2002, *MNRAS*, **336**, 1188
- Ledoux C., Petitjean P., Bergeron J., Wampler E. J., Srianand R., 1998, *A&A*, **337**, 51
- Ledoux C., Petitjean P., Fynbo J. P. U., Møller P., Srianand R., 2006, *A&A*, **457**, 71
- Ledoux C., Noterdaeme P., Petitjean P., Srianand R., 2015, *A&A*, **580**, A8
- Levesque E. M., Kewley L. J., Larson K. L., 2010, *AJ*, **139**, 712
- López G., Chen H.-W., 2012, *MNRAS*, **419**, 3553
- Lundgren B. F., et al., 2021, *ApJ*, **913**, 50
- Ma X., Hopkins P. F., Faucher-Giguère C.-A., Zolman N., Muratov A. L., Kereš D., Quataert E., 2016, *MNRAS*, **456**, 2140
- Marigo P., Bressan A., Nanni A., Girardi L., Pumo M. L., 2013, *Monthly Notices of the Royal Astronomical Society*, **434**, 488
- Martin C. L., Shapley A. E., Coil A. L., Kornei K. A., Bundy K., Weiner B. J., Noeske K. G., Schiminovich D., 2012, *The Astrophysical Journal*, **760**, 127
- McGaugh S. S., 1991, *ApJ*, **380**, 140
- Ménard B., Nestor D., Turnshek D., Quider A., Richards G., Chelouche D., Rao S., 2008, *MNRAS*, **385**, 1053
- Mingozzi M., et al., 2020, *A&A*, **636**, A42
- Moustakas J., Kennicutt Robert C. J., Tremonti C. A., 2006, *ApJ*, **642**, 775
- Murga M., Zhu G., Ménard B., Lan T.-W., 2015, *MNRAS*, **452**, 511
- Murray N., Ménard B., Thompson T. A., 2011, *ApJ*, **735**, 66
- Ménard B., Wild V., Nestor D., Quider A., Zibetti S., Rao S., Turnshek D., 2011, *Monthly Notices of the Royal Astronomical Society*, **417**, 801
- Nagao T., Maiolino R., Marconi A., 2006, *A&A*, **459**, 85
- Nakajima K., Ouchi M., 2014, *MNRAS*, **442**, 900
- Navarro J. F., Frenk C. S., White S. D. M., 1997, *ApJ*, **490**, 493
- Nestor D. B., Turnshek D. A., Rao S. M., Quider A. M., 2007, *The Astrophysical Journal*, **658**, 185–202
- Nestor D. B., Johnson B. D., Wild V., Ménard B., Turnshek D. A., Rao S., Pettini M., 2011a, *MNRAS*, **412**, 1559
- Nestor D. B., Johnson B. D., Wild V., Ménard B., Turnshek D. A., Rao S., Pettini M., 2011b, *Monthly Notices of the Royal Astronomical Society*, **412**, 1559
- Nielsen N. M., Churchill C. W., Kacprzak G. G., 2013a, *The Astrophysical Journal*, **776**, 115
- Nielsen N. M., Churchill C. W., Kacprzak G. G., 2013b, *The Astrophysical Journal*, **776**, 115
- Noterdaeme P., Petitjean P., Ledoux C., Srianand R., Ivanchik A., 2008, *A&A*, **491**, 397
- Noterdaeme P., Srianand R., Mohan V., 2010a, *MNRAS*, **403**, 906
- Noterdaeme P., Petitjean P., Ledoux C., López S., Srianand R., Vergani S. D., 2010b, *A&A*, **523**, A80
- Pagel B. E. J., Edmunds M. G., Blackwell D. E., Chun M. S., Smith G., 1979, *MNRAS*, **189**, 95
- Péroux C., Howk J. C., 2020, *ARA&A*, **58**, 363
- Péroux C., Nelson D., van de Voort F., Pillepich A., Marinacci F., Vogelsberger M., Hernquist L., 2020, *MNRAS*, **499**, 2462
- Petitjean P., Bergeron J., 1990, *A&A*, **231**, 309
- Petitjean P., Bergeron J., Puget J. L., 1992, *A&A*, **265**, 375
- Pettini M., Pagel B. E. J., 2004, *MNRAS*, **348**, L59
- Péroux C., Bouché N., Kulkarni V. P., York D. G., 2013, *Monthly Notices of the Royal Astronomical Society*, **436**, 2650
- Rahmani H., et al., 2016, *MNRAS*, **463**, 980
- Rao S. M., Turnshek D. A., Sardane G. M., Monier E. M., 2017, *MNRAS*, **471**, 3428
- Richter P., 2012, *ApJ*, **750**, 165
- Rubin K. H. R., Prochaska J. X., Koo D. C., Phillips A. C., Weiner B. J., 2010, *The Astrophysical Journal*, **712**, 574
- Rubin K. H. R., Prochaska J. X., Koo D. C., Phillips A. C., 2012, *The Astrophysical Journal*, **747**, L26
- Rubin K. H. R., Prochaska J. X., Koo D. C., Phillips A. C., Martin C. L., Winstrom L. O., 2014, *The Astrophysical Journal*, **794**, 156
- Rubin K. H. R., Diamond-Stanic A. M., Coil A. L., Crighton N. H. M., Moustakas J., 2018, *ApJ*, **853**, 95
- Savage B. D., et al., 2000, *ApJS*, **129**, 563
- Schroetter I., Bouché N., Péroux C., Murphy M. T., Contini T., Finley H., 2015, *ApJ*, **804**, 83
- Schroetter I., et al., 2019, *MNRAS*, **490**, 4368
- Selsing J., Fynbo J. P. U., Christensen L., Krogager J. K., 2016, *A&A*, **585**, A87
- Speagle J. S., Steinhardt C. L., Capak P. L., Silverman J. D., 2014, *ApJS*, **214**, 15
- Srianand R., Khare P., 1994, *The Astrophysical Journal*, **428**, 82
- Srianand R., Gupta N., Petitjean P., Noterdaeme P., Saikia D. J., 2008, *MNRAS*, **391**, L69
- Srianand R., Hussain T., Noterdaeme P., Petitjean P., Krühler T., Japelj J., Páris I., Kashikawa N., 2016, *Monthly Notices of the Royal Astronomical Society*, **460**, 634
- Steidel C. C., 1995, in Meylan G., ed., QSO Absorption Lines. p. 139 (arXiv:astro-ph/9509098)
- Steidel C. C., Kollmeier J. A., Shapley A. E., Churchill C. W., Dickinson M., Pettini M., 2002, *ApJ*, **570**, 526
- Steidel C. C., et al., 2014, *ApJ*, **795**, 165
- Storey P. J., Zeippen C. J., 2000, *MNRAS*, **312**, 813
- Straka L. A., et al., 2015, *Monthly Notices of the Royal Astronomical Society*, **447**, 3856
- Tody D., 1986, in Crawford D. L., ed., Society of Photo-Optical Instrumentation Engineers (SPIE) Conference Series Vol. 627, Instrumentation in astronomy VI. p. 733, doi:10.1117/12.968154
- Tremonti C. A., Moustakas J., Diamond-Stanic A. a. M., 2007, *The Astrophysical Journal*, **663**, L77
- Virtanen P., et al., 2020, *Nature Methods*, **17**, 261
- Weiner B. J., et al., 2009, *ApJ*, **692**, 187
- Wild V., Hewett P. C., 2005, *MNRAS*, **361**, L30
- Xin B., Ivezić Ž., Lupton R. H., Peterson J. R., Yoachim P., Jones R. L., Claver C. F., Angeli G., 2018, *AJ*, **156**, 222
- Yan R., Blanton M. R., 2012, *ApJ*, **747**, 61
- Yan R., Newman J. A., Faber S. M., Konidaris N., Koo D., Davis M., 2006, *ApJ*, **648**, 281
- York D. G., et al., 2000, *AJ*, **120**, 1579
- York D. G., et al., 2006, *MNRAS*, **367**, 945
- Zabl J., et al., 2019, *Monthly Notices of the Royal Astronomical Society*, **485**, 1961
- Zabl J., et al., 2021, *MNRAS*, **507**, 4294
- Zhu G., Ménard B., 2013, *ApJ*, **770**, 130
- Zibetti S., Menard B., Nestor D. B., Quider A. M., Rao S. M., Turnshek D. A., 2007, *The Astrophysical Journal*, **658**, 161
- Zou S., Petitjean P., Noterdaeme P., Ledoux C., Krogager J. K., Fathivavsari H., Srianand R., López S., 2018, *A&A*, **616**, A158

## APPENDIX A: GAUSSIAN FITS TO ABSORPTION LINES

We computed the redshift and rest equivalent widths of absorption lines using Gaussian fits. In Figure A1 we summarise the fits to Mg II, Mg I, Fe II and Mn II. The corresponding plots for cases with clear Ca II detections are shown in Figure A2.

## APPENDIX B: BAL QUASARS AS FALSE USMGII DETECTION IN THE ABSORBER CATALOG

With our selection criteria for USMgII absorption systems, i.e. accessible to SALT and having absorption redshift in the interval  $0.4 \leq z_{\text{abs}} \leq 0.6$ , the JHU-SDSS Metal Absorber Catalog of Zhu & Ménard (2013) yields a total of 109 USMgII systems. As discussed in Section 2, a careful visual inspection of individual spectrum resulted in only a total of 27 USMgII systems being secure. Table B1 summarises the details of all the 109 USMgII systems. In the last column of this table, we describe our reasoning for the inclusion or the exclusion of all of these 109 systems in our USMgII sample.

## APPENDIX C: SURVEY COMPLETENESS

In Table 4, we list the galaxies in DECaLS galaxy catalog (Dey et al. 2019) having consistent photo-z with our USMgII absorbers and within an impact parameter of 100 kpc. Last column of this table provides the status of spectroscopic redshift measurements. We use the information provided in this table to quantify the survey completeness of our sample (see section 3.1).

## APPENDIX D: $W_{3935}^{\text{CaII}}$ VS $E(B-V)$

In Figure D1 we plot rest equivalent width of Ca II  $\lambda 3936$  against  $E(B-V)$  for our sample, C I absorbers from Zou et al. (2018) and DLAs from Wild & Hewett (2005). The curve shown in this figure is for our Galactic sightlines found by Murga et al. (2015). Wild & Hewett (2005) reported a possible correlation between the two quantities. Note that the sample spans a large  $E(B-V)$  for a given  $W_{3935}^{\text{CaII}}$ . However, such a correlation was not clearly evident in the case of Zou et al. (2018). Our data points roughly follow the trend shown by the sample of Wild & Hewett (2005), however the error in our equivalent width measurements are large. Also our sample lacks systems with large  $E(B-V)$  and Ca II absorption detections.

## APPENDIX E: $L_{[\text{O III}]} / L_{[\text{O II}]}$ VS $W_{2796}$

In Figure E1 we plot the ratio of  $[\text{O III}]/[\text{O II}]$  as a function of  $W_{2796}$  for GOTOQs and our USMgII absorbers. Green stars show the average value of this ratio for 4 different  $W_{2796}$  bins. We do see a tendency for the ratio to be smaller for systems with larger  $W_{2796}$ . Only for the GOTOQs, the Spearman rank correlation coefficient is -0.094 (p-value = 0.436) while for the combined sample (GOTOQs + Our USMgII sample) the Spearman rank correlation coefficient is -0.251 (p-value = 0.021).

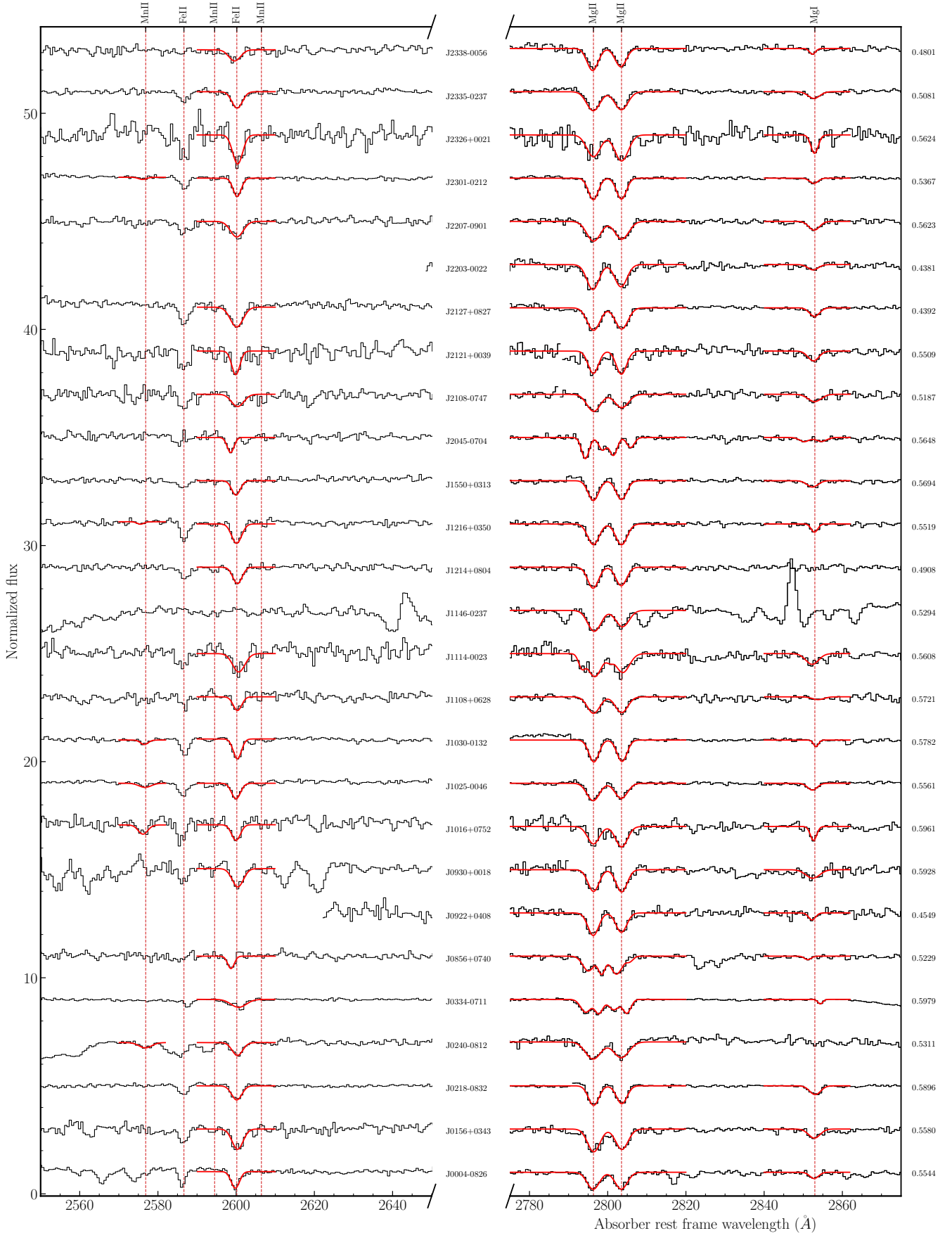


**Figure A1.** Gaussian fits to absorption profiles of Mn II, Fe II, Mg II, and Mg I for all USMgII systems in our sample in the rest frame of the absorbing gas. Normalized quasar spectrum is shown in black. Solid red lines overlaid on the normalized spectra are obtained Gaussian fits. The red dashed vertical lines drawn according to the USMgII absorption redshift corresponds to the different transitions marked on the top panel.



**Table B1.** Details of all the 109 USMgII absorber from [Zhu & Ménard \(2013\)](#)

No.	Quasar	Plate	MJD	Fiber	$z_{\text{qso}}$	$z_{\text{abs}}$	Comment
1	J000413.73-082625.4	7148	56591	326	2.2470	0.5544	Secured USMgII system. Clear detection of Mg II and Fe II doublets.
2	J000510.28-042216.9	7035	56568	606	2.1950	0.5014	False detection of USMgII due to blending.
3	J000701.42-011459.1	4217	55478	178	2.3220	0.5742	Mg II identification is not secured.
4	J000828.36-004326.7	4217	55478	224	2.0530	0.4876	False detection of USMgII due to blending.
5	J001239.55+091650.1	4536	55857	654	2.3880	0.5300	False detection of USMgII .
6	J001409.26-070806.0	7150	56597	510	2.1950	0.4547	False detection of USMgII due to blending.
7	J003459.49+034456.9	4303	55508	414	2.2350	0.5917	BAL quasar.
8	J003941.88+054253.1	4419	55867	660	2.1050	0.5955	BAL quasar.
9	J004502.79+003604.1	3589	55186	806	2.0940	0.5221	BAL quasar.
10	J005233.67+014040.8	4306	55584	74	2.3010	0.5660	False detection of USMgII due to blending.
11	J010515.45+004742.3	4225	55455	955	2.4060	0.5659	False detection of USMgII due to blending.
12	J010749.31+033913.5	4309	55528	104	0.5070	0.5000	BAL quasar.
13	J012606.00-085651.9	2878	54465	434	1.8314	0.5197	BAL quasar.
14	J015035.94+083512.4	4532	55559	930	1.9950	0.4903	BAL quasar.
15	J015345.35-100839.6	665	52168	209	1.9148	0.5655	BAL quasar.
16	J015635.18+034308.1	4270	55511	144	1.3710	0.5580	Secured USMgII system. Clear detection of Mg II and Fe II doublets.
17	J015931.02+005449.6	4234	55478	588	2.4500	0.5740	False detection of USMgII .
18	J020102.94-055819.2	4398	55946	525	1.9440	0.4630	BAL quasar.
19	J020630.60-061124.4	7238	56660	227	2.0190	0.5351	BAL quasar.
20	J020959.47-055125.7	4394	55924	566	2.5170	0.5849	False detection of USMgII .
21	J021035.82-010524.2	1074	52937	5	1.9242	0.5838	BAL quasar.
22	J021717.53-005148.9	4236	55479	140	2.2360	0.5903	BAL quasar.
23	J021820.10-083259.4	4395	55828	780	1.2190	0.5896	Secured USMgII system. Clear detection of Mg II and Fe II doublets.
24	J022234.71-040417.6	6369	56217	739	2.0430	0.5029	False detection of USMgII due to blending.
25	J023740.12-001231.0	4240	55455	476	1.9800	0.4503	BAL quasar.
26	J024008.21-081223.4	7057	56593	480	2.2310	0.5311	Secured USMgII system. Clear detection of Mg II and Fe II doublets.
27	J024426.85-005440.1	3650	55244	8	2.3130	0.4907	False detection of USMgII .
28	J024459.75+005411.1	7337	56686	756	2.3790	0.5958	False detection of USMgII .
29	J024747.59-004810.1	6782	56576	54	1.9300	0.5780	BAL quasar.
30	J025216.20-055801.9	7054	56575	324	2.3250	0.5082	False detection of USMgII due to blending.
31	J030443.10-082537.5	458	51929	98	1.9057	0.5512	BAL quasar.
32	J033438.28-071149.0	461	51910	74	0.6358	0.5979	Secured USMgII system. Clear detection of Mg II doublets.
33	J080853.34+084509.2	2570	54081	444	1.9814	0.5013	False identification of Mg II doublets.
34	J081242.14+082832.5	2570	54081	616	2.3181	0.5103	BAL quasar.
35	J082126.38+092529.1	2571	54055	518	1.8351	0.5358	BAL quasar.
36	J083033.10+075438.9	4866	55895	754	1.9600	0.5579	BAL quasar.
37	J084031.86+053419.2	4903	55927	226	1.8930	0.4366	False detection of USMgII .
38	J085627.09+074031.7	1299	52972	173	1.8932	0.5224	Secured identification of USMgII . Clear detection of Mg II and Fe II doublets.
39	J090653.58+095930.3	1739	53050	286	1.6885	0.4504	BAL quasar.
40	J091532.66+073734.3	4869	55896	944	2.3510	0.5176	False detection of USMgII .
41	J092100.99+045311.7	991	52707	217	1.8163	0.4924	BAL quasar.
42	J092222.53+040858.6	568	52254	372	0.7146	0.4549	Secured USMgII system. Clear detection of Mg II doublets.
43	J093020.60+001828.0	3823	55534	996	2.4300	0.5928	Secured USMgII system. Clear detection of Mg II and Fe II doublets.
44	J093512.75-013724.6	3767	55214	776	2.1490	0.4770	False detection of USMgII . No trace of Fe II doublets.
45	J100726.26+051300.7	573	52325	445	1.9052	0.4488	False identification of USMgII .
46	J101610.82+075209.1	5334	55928	90	2.1870	0.5961	Secured USMgII system. Clear detection of Mg II and Fe II doublets.
47	J102510.09-004644.9	3832	55289	409	2.2120	0.5561	Secured USMgII system. Clear detection of Mg II and Fe II doublets.
48	J103015.07-025032.8	3785	55241	724	2.1480	0.5783	Secured USMgII system. Clear detection of Mg II and Fe II doublets.
49	J103059.75-013237.7	3785	55273	338	2.1680	0.5714	BAL quasar
50	J103326.53+015841.7	4739	55644	18	2.1260	0.4720	Mg II identification is not secured.
51	J104652.17+063404.0	4853	55928	318	2.3650	0.5572	False detection of USMgII .
52	J110338.72+084101.1	5359	55953	928	2.3900	0.5859	BAL quasar.
53	J110817.93+062832.9	1003	52641	19	1.2049	0.5721	Secured USMgII system. Clear detection of Mg II and Fe II doublets.
54	J111249.66+005310.1	278	51900	619	1.6822	0.4274	BAL quasar.
55	J111359.99-002342.7	279	51984	262	0.9535	0.5617	Secured USMgII system. Clear detection of Mg II and Fe II doublets.
56	J111816.33+083436.1	2413	54169	16	0.5830	0.5821	USMgII absorption from the host galaxy of the quasar.
57	J112021.40+084423.0	5369	56272	766	2.1140	0.5505	BAL quasar.
58	J113826.30-015428.9	3775	55207	699	1.9230	0.5770	BAL quasar.
59	J114546.21+032251.9	514	51994	458	2.0091	0.5441	False identification of USMgII .
60	J114614.24-023716.1	3790	55208	420	2.1500	0.5295	Secured detection of USMgII absorption.

**Table B1.** Continued.

61	J115820.00+065415.3	1622	53385	64	1.7105	0.4651	BAL quasar.
62	J120359.81+095419.0	5391	56000	552	2.0240	0.4711	BAL quasar.
63	J121453.29+080457.7	1624	53386	505	1.4325	0.4908	Secured USMgII system. Clear detection of Mg II and Fe II doublets.
64	J121628.03+035031.8	4751	55646	614	0.9960	0.5519	Secured USMgII system. Clear detection of Mg II and Fe II doublets.
65	J122043.21-013215.3	333	52313	540	0.4482	0.4453	USMgII absorption from the host galaxy of the quasar.
66	J122354.57+095935.3	5401	55949	518	2.3530	0.5692	BAL quasar.
67	J123256.70-000604.3	3848	55647	388	2.3750	0.5211	False detection of USMgII .
68	J124602.10+075425.6	5407	55926	39	2.1390	0.5432	BAL quasar.
69	J124628.80+061039.2	847	52426	366	1.9588	0.5925	BAL quasar.
70	J124644.46-025122.3	336	51999	172	1.7713	0.4961	BAL quasar.
71	J133748.81-020102.7	4047	55352	710	0.5780	0.5742	BAL quasar.
72	J140301.31+032531.9	4783	55652	446	2.2560	0.5212	BAL quasar.
73	J140601.18-012443.1	4038	55363	796	1.8350	0.5186	BAL quasar.
74	J141206.73+071325.6	1824	53491	625	2.0192	0.5996	False identification of USMgII .
75	J142717.70+084255.2	5462	55978	222	2.1970	0.5313	False detection of USMgII due to blending.
76	J143830.68-014807.4	4026	55325	696	2.2200	0.5914	BAL quasar.
77	J144959.96+003225.3	309	51994	357	1.7065	0.4648	BAL quasar.
78	J144959.96+003225.3	310	51990	305	1.9253	0.5804	BAL quasar.
79	J145704.53+072033.3	1815	53884	299	2.0192	0.5966	False identification of USMgII .
80	J145913.71+000215.9	4019	55363	36	1.9300	0.5807	BAL quasar.
81	J150919.01-013353.4	922	52426	586	2.0656	0.5128	BAL quasar.
82	J150919.01-013353.4	922	52426	586	2.0656	0.5244	BAL quasar.
83	J150938.28+050524.4	4776	55652	782	2.3270	0.5632	False detection of USMgII .
84	J152218.01+051007.0	4803	55734	558	2.4540	0.5863	False detection of USMgII .
85	J153200.65+090540.0	5209	56002	812	2.1560	0.5633	BAL quasar.
86	J155003.71+031325.0	594	52045	611	1.7879	0.5694	Secured USMgII system. Clear detection of Mg II and Fe II doublets.
87	J162902.98+091322.5	2532	54589	494	1.9913	0.4470	False identification of USMgII .
88	J204333.20-001104.2	981	52435	44	0.5469	0.5293	BAL quasar.
89	J204501.33-070452.6	1917	53557	205	0.6702	0.5635	Secured USMgII system. Clear detection of Mg II and Fe II doublets.
90	J210851.54-074726.5	638	52081	126	1.4890	0.5187	Secured USMgII system. Clear detection of Mg II and Fe II doublets.
91	J212119.15+012039.6	5142	55825	776	2.1980	0.4906	False detection of USMgII due to blending.
92	J212143.98+003954.2	5142	55825	220	1.3480	0.5509	Secured USMgII system. Clear detection of Mg II and Fe II doublets.
93	J212727.19+082724.6	4089	55470	402	0.7450	0.4392	Secured USMgII system. Clear detection of Mg II and Fe II doublets.
94	J213157.89+031459.0	4080	55471	29	2.2800	0.5299	False detection of USMgII .
95	J213555.40-063553.6	641	52199	567	1.1724	0.4443	False identification of Mg II doublets.
96	J220131.89-001543.4	4198	55480	118	1.9300	0.4462	BAL quasar.
97	J220330.04-002211.4	372	52173	26	1.7640	0.4381	Secured USMgII system. Clear identification of Fe II and Mg II doublets.
98	J220619.09-031423.1	4377	55828	296	2.2080	0.5970	BAL quasar.
99	J220702.53-090127.8	718	52206	209	1.2965	0.5623	Secured USMgII system. Clear detection of Mg II and Fe II doublets.
100	J222848.61+000633.7	4202	55445	940	2.3280	0.5352	False detection of USMgII .
101	J222848.61+000633.7	4214	55451	10	2.2370	0.5078	BAL quasar.
102	J223308.78-085445.4	721	52228	71	1.8525	0.5238	BAL quasar.
103	J230101.29-021200.0	4362	55828	814	0.6190	0.5367	Secured USMgII system. Clear detection of Mg II and Fe II doublets.
104	J230124.06+091704.6	5056	55921	110	2.1250	0.5555	BAL quasar.
105	J232627.39+034627.2	4283	55864	538	2.0050	0.4735	BAL quasar.
106	J232653.14+002142.9	1095	52521	549	2.1959	0.5624	Secured identification of USMgII .
107	J233548.62-023734.3	4357	55829	434	1.2250	0.5081	Secured USMgII system. Clear detection of Mg II and Fe II doublets.
108	J233818.25-005610.5	385	51877	295	0.8946	0.4801	Secured USMgII system. Clear detection of Mg II doublets.
109	J235859.47-002426.2	387	51791	181	1.7592	0.4930	BAL quasar.

**Table C1.** Details of galaxies with consistent photo-z to the USMgn absorbers in our sample with  $D < 100$  kpc

No.	Quasar Name	$z_{\text{abs}}$	Galaxy coordinates	D(kpc)	$m_r$	Photo-z	Comments
1	J0004-0826	0.5544	J000413.99-082624.27	26	19.9	$0.558 \pm 0.044$	Spectroscopically confirmed
			J000413.18-082632.34	69	22.9	$0.648 \pm 0.161$	Consistent photo-z
2	J0156+0343	0.5581	J015635.21+034306.03	14	20.9	$0.573 \pm 0.037$	Spectroscopically confirmed
			J015635.19+034311.86	23	23.3	$0.635 \pm 0.403$	Consistent photo-z
			J015634.97+034305.15	28	21.6	$0.488 \pm 0.104$	Consistent photo-z
			J015635.30+034303.22	34	23	$0.497 \pm 0.143$	Spectroscopically confirmed
			J015635.54+034311.76	41	22	$0.524 \pm 0.112$	Consistent photo-z
			J015635.55+034304.93	41	21	$0.455 \pm 0.106$	Consistent photo-z
3	J0218-0832	0.5896	J021820.26-083258.39	16	21.1	$0.632 \pm 0.026$	Spectroscopically confirmed
4	J0240-0812	0.5311	J024008.39-081222.53	18	20.7	$0.524 \pm 0.076$	Spectroscopically confirmed
			J024007.42-081224.78	74	22.7	$0.556 \pm 0.1$	Consistent photo-z
			J024008.97-081217.78	79	23.4	$0.77 \pm 0.306$	Consistent photo-z
			J024009.08-081225.12	82	23.4	$0.596 \pm 0.107$	Consistent photo-z
5	J0334-0711	0.5977	J033438.08-071152.08	28	20.9	$0.553 \pm 0.18$	Spectroscopically confirmed
			J033438.54-071153.17	37	22.6	$0.595 \pm 0.074$	Consistent photo-z
6	J0856+0740	0.5232	J085627.22+074031.36	12	23	$0.627 \pm 0.141$	Consistent photo-z but no nebular emission detected
			J085627.31+074029.51	24	21.7	$0.577 \pm 0.112$	Spectroscopically confirmed
			J085626.52+074025.70	65	23	$0.503 \pm 0.127$	Consistent photo-z
			J085626.08 +074035.84	98	23.5	$0.558 \pm 0.257$	Consistent photo-z
7	J0922+0408	0.4549	J092222.52+040856.00	15	20.8	$0.333 \pm 0.109$	Not consistent but spectroscopically confirmed
8	J1114-0023	0.5610	J111400.04-002341.21	10	22	$0.893 \pm 0.18$	Not consistent
			J111400.19-002341.33	20	22.5	$0.505 \pm 0.101$	Consistent photo-z
			J111359.65-002336.94	49	23.4	$0.725 \pm 0.205$	Consistent photo-z
9	J1214+0804	0.4908	J121453.46+080457.03	16	20.5	$0.408 \pm 0.079$	Spectroscopically confirmed
			J121453.16+080446.44	68	23.5	$0.869 \pm 0.57$	Consistent photo-z
10	J1216+0350	0.5519	...	...	...	...	GOTOQ with no other candidates
11	J1550+0313	0.5694	J155003.70+031325.70	4	21.9	$0.436 \pm 0.361$	Consistent photo-z but no nebular emission detected
			J155003.47+031325.77	23	20.5	$0.485 \pm 0.085$	Spectroscopically confirmed
			J155002.95+031333.28	90	21.5	$0.314 \pm 0.269$	Consistent photo-z
12	J2045-0704	0.5649	J204501.46-070452.13	13	21.8	$0.56 \pm 0.086$	Consistent photo-z but no nebular emission detected
				52	22.6	$0.58 \pm 0.271$	Consistent photo-z
13	J2108-0704	0.5187	J210851.43-074727.67	12	21.6	$0.398 \pm 0.144$	Spectroscopically confirmed
14	J2121+0039	0.5509	J212144.18+003954.25	19	20.9	$0.566 \pm 0.102$	Spectroscopically confirmed
15	J2127+0827	0.4392	J212727.09+082724.21	8	20.5	$0.306 \pm 0.145$	Spectroscopically confirmed
16	J2203-0022	0.4381	J220329.98-002209.56	11	22.2	$0.455 \pm 0.147$	Consistent photo-z but no nebular emission detected
			J220329.76-002215.03	31	20	$0.358 \pm 0.081$	Spectroscopically confirmed
			J220329.70-002217.06	42	23.5	$0.965 \pm 0.611$	Consistent photo-z
17	J2207-0901	0.5623	J220702.92-090128.50	37	22	$0.371 \pm 0.071$	Spectroscopically confirmed
			J220702.86-090132.85	45	22.9	$0.568 \pm 0.187$	Consistent photo-z (Spectroscopically confirmed)
			J220703.09-090125.14	56	20.9	$0.551 \pm 0.029$	Consistent photo-z
			J220702.02-090132.81	58	20.5	$0.505 \pm 0.094$	Consistent photo-z
			J220703.22-090136.62	88	23.3	$0.582 \pm 0.235$	Consistent photo-z
18	J2301-0212	0.5367	J230100.83-021202.97	47	22.2	$0.627 \pm 0.238$	Consistent photo-z
19	J2326+0021	0.5624	J232653.20+002148.10	33	19.6	$0.485 \pm 0.037$	Spectroscopically confirmed
			J232652.87+002135.83	53	22.3	$0.479 \pm 0.101$	Consistent photo-z
			J232653.10+002156.14	85	22.5	$0.591 \pm 0.083$	Consistent photo-z
20	J2335-0237	0.5081	J233548.79-023734.79	16	20.6	$0.54 \pm 0.075$	Spectroscopically confirmed
			J233548.45-023738.64	30	22.9	$0.693 \pm 0.339$	Consistent photo-z
			J233549.09-023742.99	68	21.6	$0.482 \pm 0.236$	Consistent photo-z
			J233549.48-023730.00	84	23.5	$0.969 \pm 0.592$	Consistent photo-z
21	J2338-0056	0.4801	J233818.44-005610.48	16	22.2	$0.516 \pm 0.077$	No nebular emission
			J233817.985-005617.62	49	22.9	$0.62 \pm 0.19$	Consistent photo-z
			J233817.58-005609.86	60	22	$0.497 \pm 0.037$	No nebular emission
			J233819.09-005605.87	79	22.3	$0.449 \pm 0.082$	Spectroscopically confirmed
			J233817.38-005604.47	86	21.6	$0.523 \pm 0.103$	Consistent photo-z

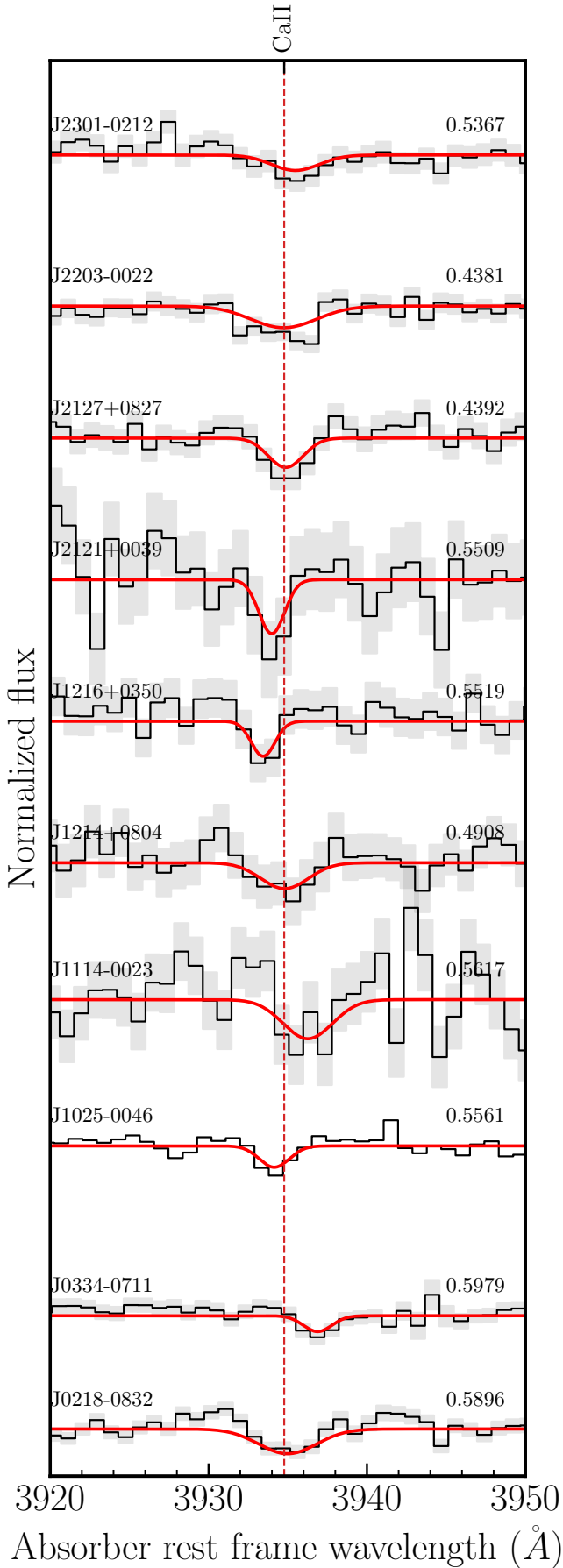


**Figure A2.** Gaussian fit to the Ca II absorption associated with the USMgII absorptions in the absorber rest frame. The vertical red dashed line corresponds to the expected location of Ca II absorption based on redshift of the USMgII absorption.

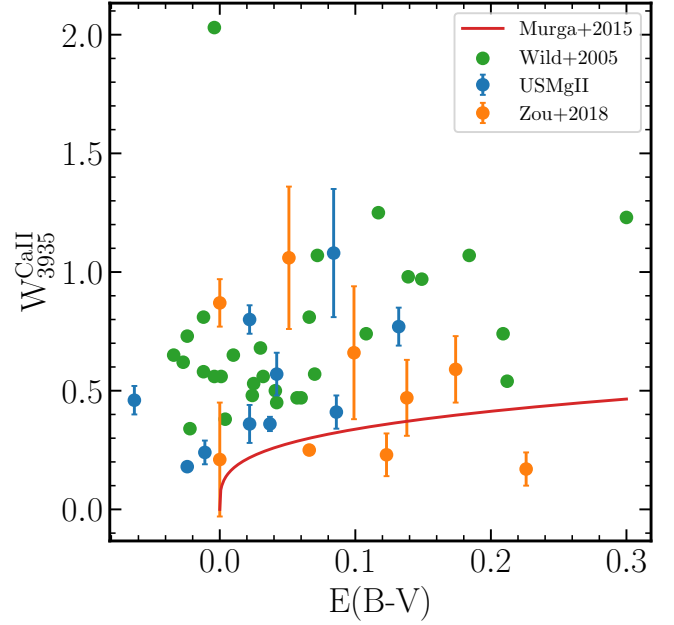


**Figure D1.** Ca II  $\lambda$  3935 rest equivalent width plotted against the color excess of the background quasars for our USMgII sample (blue), high redshift C I absorbers (orange) (Zou et al. 2018), and the Ca II absorbers from SDSS DR3 in the redshift range  $0.84 \leq z_{\text{abs}} \leq 1.3$  (Wild & Hewett 2005). The red solid line corresponds to the relation obtained for our Milky way galaxy.

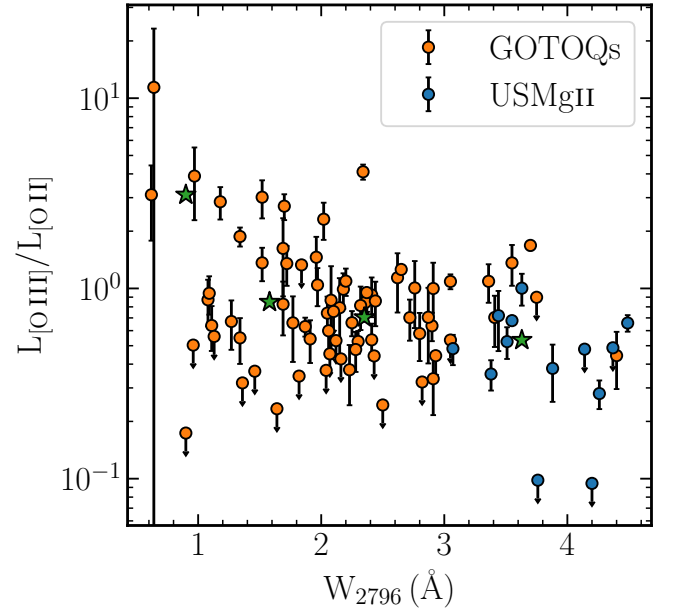


**Figure E1.**  $L_{[\text{O III}]} / L_{[\text{O II}]}$  ratio vs the rest equivalent width of Mg II for both GOTOQs (orange) and our USMgII (blue) sample. Green stars give median values of the ratio for different  $W_{2796}$  bins.

## APPENDIX F: USMgII SYSTEMS FROM THE LITERATURE

In this section, we concentrate on various Mg II absorption surveys that have been conducted over the years and in particular if they contain any USMgII absorption and the physical properties of the associated host galaxy. For this exercise we consider the following surveys: (i) MAGG (Dutta et al. 2020), (ii) MEGAFLOW (Schroetter et al. 2019), (iii) MAGIICAT (Nielsen et al. 2013a), (iv) SIMPLE (Bouché et al. 2007; Schroetter et al. 2015), (v) Nestor et al. (2011b), (vi) Gauthier (2013) and, (vii) Huang et al. (2021).

As mentioned before in the text, MAGG (Dutta et al. 2020) is a IFU based galaxy-centric Mg II absorption systems survey containing a total of 228 galaxies around 28 quasar fields in the redshift range  $0.8 \leq z \leq 1.5$  using MUSE. This survey is about 90% complete down to the SFR  $\sim 0.1 M_{\odot} \text{yr}^{-1}$  and a projected distance of about 250-350 kpc from the background quasars.

The MEGAFLOW survey (Zabl et al. 2019), on the other hand, aimed to study the gas flows and the galactic winds in the galaxies, is a IFU based absorber-centric study using the same instrument, MUSE. This survey primarily contains 22 quasar fields with at least three strong ( $W_{2796} \geq 0.5 \text{Å}$ ) Mg II absorption systems along individual line of sight and a few more relatively weak ( $0.3 \text{Å} \leq W_{2796} \leq 0.5 \text{Å}$ ) Mg II absorption systems. As a result, the MEGAFLOW survey contains 79 Mg II absorption systems ( $W_{2796} \geq 0.3 \text{Å}$ ) towards 22 different quasar sightlines in the redshift range  $0.51 \leq z \leq 1.45$ .

The MAGIICAT survey is a compilation of the Mg II absorption systems in the redshift range  $0.07 \leq z \leq 1.12$  based on the studies previously done and it is comprised of both absorber-centric and galaxy-centric inspections.

The SIMPLE survey is again an absorber-centric survey with  $W_{2796} \geq 2 \text{Å}$  around the redshift  $\sim 1$ . The sample consists of 21 such Mg II absorption systems, out of which, for 14 cases the host galaxies are identified within an impact parameter of 54 kpc. The galaxies are detected using the  $H\alpha$  nebular emission line with the  $3\sigma$  detection threshold is given by  $F_{H\alpha} \geq 1.2 \times 10^{-17} \text{ ergs s}^{-1} \text{ cm}^{-2}$  ( $\sim 0.5 M_{\odot} \text{yr}^{-1}$ ).

Nestor et al. (2011b) studied a pair of USMgII systems around the redshift  $z \sim 0.7$  and identified a pair of USMgII host galaxies within the impact parameters of 61 kpc for both the cases.

Gauthier (2013) also studied a particular USMgII absorption which is basically a part of our USMgII sample and identified a galaxy group containing 4 galaxies being responsible for the USMgII absorption observed against the background quasar.

Huang et al. (2021) studied the gas around a total of 380 galaxies using 156 background quasars in the redshift range  $0.10 \leq z \leq 0.48$  upto an impact parameter of 500 kpc.

## APPENDIX G: $W_{2796}$ VS. D CORRELATIONS

To improve the characterisation of the impact parameter versus the  $W_{2796}$  relationship for strong Mg II absorbers at smaller impact parameters with our observations, we fit a log-linear model to our data along with other data available in the literature assuming a log-linear dependence between  $W_{2796}$  and D of the form

$$\log W_{2796} (\text{Å}) = \alpha \times D (\text{kpc}) + \beta \quad (\text{G1})$$

Following Chen et al. (2010a), Rubin et al. (2018) and Dutta

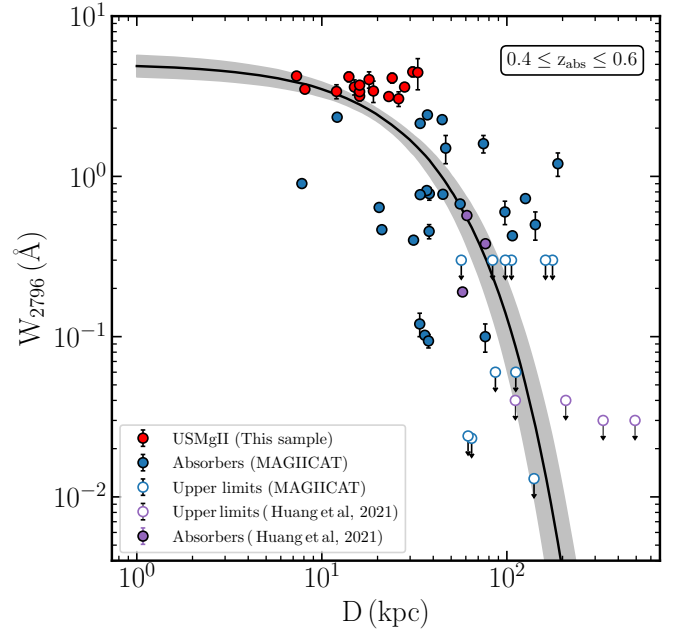


**Figure G1.** The figure shows the plot of  $W_{2796}$  against the impact parameter D for absorbers at  $0.4 \leq z \leq 0.6$  in different samples. The red, blue, and purple corresponds to the USMgII, MAGIICAT and, Huang et al. (2021) samples respectively.

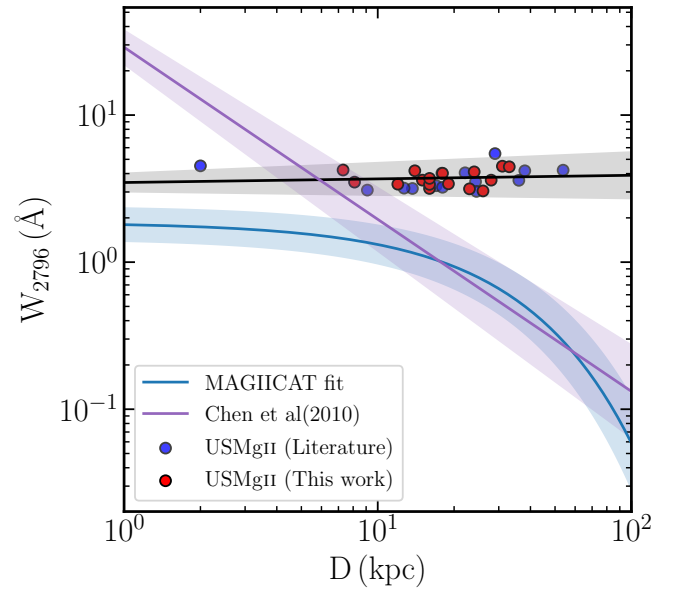


**Figure G2.**  $W_{2796}$  versus the impact parameter for the USMgII host galaxies from our sample (red) as well as from the literature (blue). The black line corresponds to a power law fit with the gray shaded region showing the  $1\sigma$  error to the fit.

et al. (2020), we define the likelihood function as follows

$$\mathcal{L}(W) = \left( \prod_{i=1}^n \frac{1}{\sqrt{2\pi\sigma_i^2}} \exp \left\{ -\frac{1}{2} \left[ \frac{W_i - W(D_i)}{\sigma_i} \right]^2 \right\} \right) \times \left( \int_{-\infty}^{W_i} \prod_{i=1}^m \frac{dW'}{\sqrt{2\pi\sigma_i^2}} \exp \left\{ -\frac{1}{2} \left[ \frac{W' - W(D_i)}{\sigma_i} \right]^2 \right\} \right) \quad (\text{G2})$$

**Table F1.** Details of USMgII from the literature

Sample Reference	Quasar	$z_{\text{abs}}$	$W_{2796}$ ( $\text{\AA}$ )	$z_{\text{em}}$	D (kpc)	$L_{[\text{OII}]}$ ( $10^{40} \text{ ergs s}^{-1}$ )	SFR ( $M_{\odot} \text{ yr}^{-1}$ )	Environment
Gauthier (2013)	J220702.64-090117.8	0.5624	4.18 $\pm$ 0.30	0.5623	55	3.6 $\pm$ 0.4	0.5 $\pm$ 0.2	Group
				0.5621	38	18 $\pm$ 1	2.5 $\pm$ 0.8	
				0.5623	209	18 $\pm$ 2	2.5 $\pm$ 1.1	
				0.5604	246	$\leq$ 9	$\leq$ 1.3	
Nestor et al. (2011b)	J074707.62+305414.9	0.7646	3.60 $\pm$ 0.11	0.7660	36	83.12 $\pm$ 0.81	11.64 $\pm$ 3.32	Pair
				0.7643	61	35.82 $\pm$ 0.82	5.01 $\pm$ 1.44	
Nestor et al. (2011b)	J141751.84+011556.1	0.6681	5.47 $\pm$ 0.18	0.6671	29	112.3 $\pm$ 0.58	15.73 $\pm$ 4.49	Pair
				0.6678	58	36.00 $\pm$ 0.39	5.04 $\pm$ 1.44	
Bouché et al. (2007) & Schroetter et al. (2015)	J014717.76+125808.8	1.0391	4.025	1.0389	17.9	–	10	Isolated
	2QZJ022620.4-285751	1.0208	4.515	1.0223	$\leq$ 2	–	8	Isolated
	J044821.8+095051.7	0.8392	3.169	0.8391	13.7	–	16	Isolated
	J094309.66+103400.6	0.9967	3.525	0.9956	24.3	–	17	Isolated
	J142253.31-000149.0	0.9097	3.185	0.9096	12.7	–	5	Isolated
	J233551.10+151453.2	0.8557	3.308	0.8557	17	–	2.3	Isolated
Dutta et al. (2020)	J162116.92-004250.8	1.13351	3.229 $\pm$ 0.002	1.13364	18	27 $\pm$ 0.25	3.78 $\pm$ 0.01	Isolated
Schroetter et al. (2019)	J010332.30+133233.5	1.0481	3.09 $\pm$ 0.17	1.0483	9.1	–	2.9 $^{+2.1}_{-1.4}$	Isolated
	J103936.67+071427.3	0.8193	3.03 $\pm$ 0.27	0.8192	24.5	–	3.2 $^{+2.4}_{-1.5}$	Isolated
	J110735.25+175731.4	1.0630	4.05 $\pm$ 0.35	1.0637	22.1	–	2.5 $^{+1.8}_{-1.2}$	Isolated
Nielsen et al. (2013a)	J000448.11-415728.8	0.8366	4.422 $\pm$ 0.002	0.8400	53.8	–	–	Isolated

where the total error for each measurement,  $\sigma_i$  is given by,

$$\sigma_i^2 = \sqrt{\sigma_c^2 + \sigma_{mi}^2}$$

where  $\sigma_c$  is the intrinsic scatter and  $\sigma_{mi}$  is the measurement error in  $W_{2796}$  for each measurement. To obtain the fitting parameters,  $\alpha$ ,  $\beta$ , and the  $\sigma_c$ , we derive posterior probability distributions using the UltraNest<sup>1</sup> package (Buchner 2021). This gives the best fitting parameters for all the Mg II absorbers from the literature including our USMgII absorbers as  $\alpha = -0.019 \pm 0.002$ ,  $\beta = 0.464 \pm 0.039$  and  $\sigma_c = 0.910 \pm 0.044$ . In the left panel of Figure 10, the best fit is shown in solid black line whereas the  $1\sigma$  error on that curve is shown in gray. In the right panel of Figure G1, we do the similar analysis, but this time restricting to only the Mg II absorbers in the redshift range  $0.4 \leq z_{\text{abs}} \leq 0.6$ . This time the fitting parameters are  $\alpha = -0.016 \pm 0.003$ ,  $\beta = 0.702 \pm 0.067$  and  $\sigma_c = 1.18 \pm 0.13$ . Note that for both the cases, the USMgII host galaxies populate a region that is significantly different from what is expected from the fits. To understand how the  $W_{2796}$  varies with impact parameter, we compiled a sample of USMgII absorbers from the literature and using our sample, and fitted the distribution with a simple model of the form Eqn. G1. The resultant fitting parameters are given by,  $\alpha = 0.023 \pm 0.047$  and  $\beta = 0.543 \pm 0.061$ . The best fit and the associated  $1\sigma$  error is shown in Figure G2.

#### APPENDIX H: ABSOLUTE B-BAND MAGNITUDE OF USMgII HOST GALAXIES

In Figure H1, we have plotted the absolute B-band magnitude  $M_B$  of both the USMgII host galaxies and the MAGIICAT host galaxies scaled by characteristic B-band magnitude ( $M_B^*$ ) at the galaxy redshift (Faber et al. 2007). Once again, we find a correlation between the impact parameters of MAGIICAT host galaxies and the relative B band magnitude, that can be characterized by a linear fit of the form,

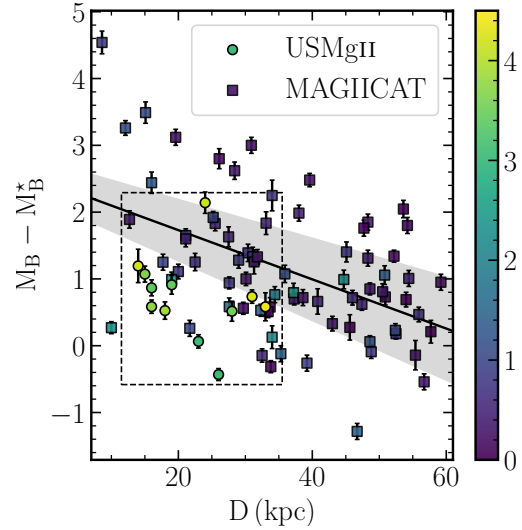


**Figure H1.** Absolute B-band magnitude of the Mg II host galaxies plotted against the impact parameter. The solid lines and shaded regions in both the plots are the best fit for the MAGIICAT sample and the  $1\sigma$  error range in the fit respectively. The USMgII host galaxies span the region in the plot marked with a dashed rectangle. Clearly, for a given impact parameter, the USMgII galaxies are brighter and more massive on average compared to the MAGIICAT galaxies.

$M_B - M_B^* = (-0.037 \pm 0.008)D + (2.445 \pm 0.302)$ . The solid black line and the grey shaded region around it in the figure corresponds to this fit and the associated  $1\sigma$  uncertainty to it. Except for one case, the USMgII host galaxies tend to be brighter at a given impact parameter (and beyond the  $1\sigma$  region) compared to the MAGIICAT host galaxies.

<sup>1</sup> <https://johannesbuchner.github.io/UltraNest/>

This paper has been typeset from a  $\text{\TeX}/\text{\LaTeX}$  file prepared by the author.